Current Ground Motions Along the Long-Point Fault Derived from Continuous GPS Observations (2012–2014)

A Thesis Presented to

the Faculty of the Department of Earth and Atmospheric Science

University of Houston

In Partial Fulfillment

of the Requirements for the Degree

Master of Science

By

John Serna, Jr.

May 2015

Current Ground Motions Along the Long-Point Fault Derived

from Continuous GPS Observations (2012–2014)

____

John Serna, Jr.

APPROVED:

____

Dr. Guoquan Wang, Chairman

____

Dr. Joel Saylor

____

Dr. Ramesh Shrestha

____

Dean, College of Natural Sciences and Mathematics

Acknowledgements

In all sincerity, I would like to express my gratitude to Dr. Guoquan Wang who took me in as a graduate student. Dr. Wang's support, instruction, and guidance, was essential in the development and completion of this project. In addition, I would like to thank Dr. Saylor and Dr. Shrestha who oversaw this project as committee members, but were also integral in focusing the project scope.

I would also like to thank the members of the Geodesy Group whose initiative, support, and camaraderie, made me feel part of the team. My deepest thanks are reserved for my family. To my mother and father, I love you and thank you for supporting me when things didn't go my way; I hope I've made you proud. Brother, thank you for being my role-model and giving me the push to better myself in all aspects of life.

Finally, I'd like to thank my dearest friends: Curtis Nichol, Robert "Nick" Lanning, and Jennifer "Kool-aid" Welch for their support.

Current Ground Motions Along the Long-Point Fault Derived from Continuous GPS Observations (2012–2014)

A Thesis Presented to

the Faculty of the Department of Earth and Atmospheric Science

University of Houston

In Partial Fulfillment

of the Requirements for the Degree

Master of Science

By

John Serna, Jr.

May 2015

ABSTRACT

The Texas Gulf Coast region possesses numerous complex fault structures. This case study focused on the Long-Point Fault, an active fault located in west Houston; with 16 kilometers of length, it is the longest fault within the region. This fault causes recurring damage to roadways, buried pipes, and buildings along the fault trace, resulting in a financial burden for taxpayers.

This study employed a high-resolution LiDAR map depicting precise locations of principal fault systems within the greater Houston metropolitan area. Georeferencing was combined with a high-accuracy kinematic GPS technique in order to establish the precise fault trace of the Long-Point Fault. Field investigations verified that the fault scarp mapped by the 2001 airborne LiDAR mapping of Houston coincides with the surface trace of the Long-Point Fault. To establish surface fault motion, eleven permanent GPS stations were installed for continuous GPS monitoring in 2012. To enhance spatial resolution, twenty-six benchmarks were installed along the Long-Point fault trace and were reoccupied in monthly surveys. Daily GPS observations from 2012–2014 were processed using both relative (double differencing) and absolute (precise point) positioning methods. Two years of GPS observations indicate that the Long-Point Fault area is experiencing subsidence. All GPS stations along the Long-Point Fault observed subsidence rated ranging from 1–7 mm/year as well as strong vertical seasonal variation, 4 cm peak to peak. Minor horizontal movements at 1–4 mm/yr, referenced to the stable Houston reference frame (SHRF), were observed at several GPS stations;

however, no coherent fault motion was observed along the length of the fault surface trace.

Groundwater data from water wells near the Long-Point Fault area were obtained and examined for possible correlation with subsidence. At the end of 2014, the groundwater levels in the Chicot and Evangeline aquifers in the Long-Point Fault area are 50–53 m and 69–106 m below the ground surface, respectively. Daily depth to groundwater level for the Chicot and Evangeline aquifer system show correlation between aquifer recharge, and withdrawal, and vertical seasonal variation exhibited by all installed GPS stations along the Long-Point Fault. The Chicot and Evangeline ground water levels have been increasing in this area since 2000, but are still below the regional preconsolidation of ~30 m below the ground surface, contributing to the subsidence observed. While correlation between seasonal vertical movement and groundwater level change exists, a longer period of continuous GPS observations will be able to provide more information about the activity of the fault.

Table of Contents

List of Figures

List of Tables

List of Appendix Figures

1 Introduction

Active faulting is a natural process that becomes a geologic hazard when people try to live where these processes occur. With booming populations in cities all over the world, commercial and residential developers must mitigate risk for sustainable development on or near these geologic hazards. While some active faults are capable of generating major earthquakes, e.g. the San Andreas Fault in California, causing catastrophic damage to property and urban infrastructure, others display aseismic creep which exhibits slow, gradual displacement without the buildup of significant strain, producing minor seismic shaking (USGS Earthquake Glossary, 2013). The Hayward Fault in California locally generates distinct damage to building foundations, roads, curbs, and sidewalks, all ascribed to aseismic creep. Risk mitigation with respect to aseismic creep, measured in millimeters or centimeters per year, proves difficult.

The hazards associated with active faulting necessitate a thorough understanding of their behaviors, e.g. stick-slip or creep and/or linear or nonlinear movement. Networks (or arrays) of Global Positioning System (GPS) stations established throughout the United States (and on a grand scale globally) provide data not just on fault displacement, but from continuous, incremental, and nearly undetectable shifts on the order of millimeters. The United States Geological Survey (USGS), the Plate Boundary Observatory (PBO), and, specific to this case study, HoustonNET provide accessible data for understanding faults (and fault systems).

Complementary to GPS technology, other technologies (e.g. interferometric synthetic aperture radar (InSAR) and airborne laser swath mapping (ALSM)) augment fault studies. InSAR was used by Buckley et al. (2003) to determine the traces of faults in the Houston area by improving spatial resolution when used in conjunction with GPS monitoring (Bawden, 2012). ALSM data of Harris County was used in a study by Shah and Lanning-Rush (2005) to map out fault systems in the Gulf Coast region.

To more effectively understand the complexities and nuances of the behavior within active faults, this study will focus on the Long-Point Fault located in the Houston metropolitan area. By georeferencing a high-resolution map (produced by the USGS from ALSM and a digital elevation model (DEM)) that depicts precise locations of principal fault systems within the greater Houston metropolitan area; via Google Earth, a detailed map of the fault trace was generated using a high-accuracy kinematic GPS technique. In order to better establish surface fault movement, eleven permanent GPS stations along the Long-Point fault were installed; continuous GPS monitoring is conducted daily. Five stations are positioned on the hanging wall of the fault, while the remaining six stations are positioned on the footwall of the fault.

The Long-Point Fault was chosen for this study for three reasons. First and foremost, damages to residential and commercial buildings, utilities, and roads associated with the fault suggest that it has been recently active (Figures 1.01-1.04). Second, the length of the Long-Point Fault (sixteen kilometers) allows for sufficient options for where the permanent GPS stations can be positioned. Last, the Long-Point

Fault lies in a densely populated area that is affected by recurring damage resulting in a financial burden to taxpayers and businesses.

Figure 1.01: Residential Building Damage

This residential building on Oak Tree Drive (Latitude: 29°47’39.12” N, Longitude: 95°31’31.96 W) sits on the Long-Point Fault. The street-side entrance to the building is situated on the footwall, while the rear entrance is situated on the hanging wall. Foundation deformation from the northwestern corner (street-side entrance) of the building to the southeast (rear entrance) is represented by the yellow line. The distance in-between the red lines display the offset created the Long-Point Fault.

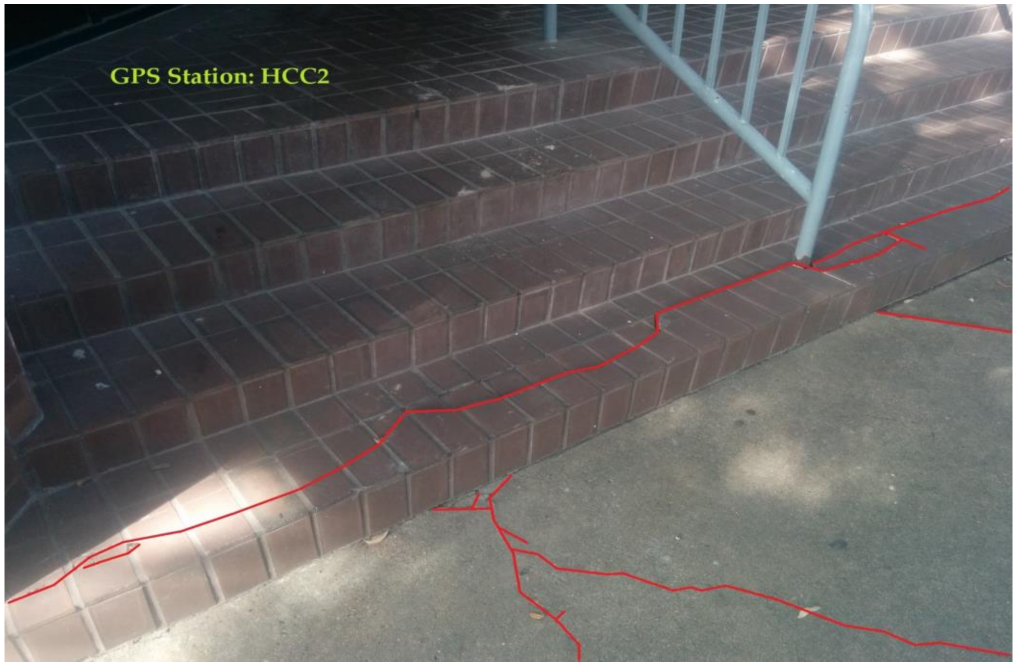

Figure 1.02: Commercial Building Damage

Houston Community College at Texas Beltway 8 Frontage Road (Latitude: 29°47’16.67” N, Longitude: 95°33’43.46” W) displays cracking in the staircase that extends to the landing. The red lines emphasize cracking patterns faintly seen due to the resolution of the photo.

Figure 1.03: Utility Damage

Utility poles on Survey Measurement #15: Brittmoore Road (Latitude: 29°46′59.99″ N, Longitude: 95°34′11.62″ W) and Survey Measurement #17: Lumpkin Road (Latitude: 29°47′22.07″ N, Longitude: 95°33′31.95″ W) disrupted (tilted) by the Long-Point Fault.

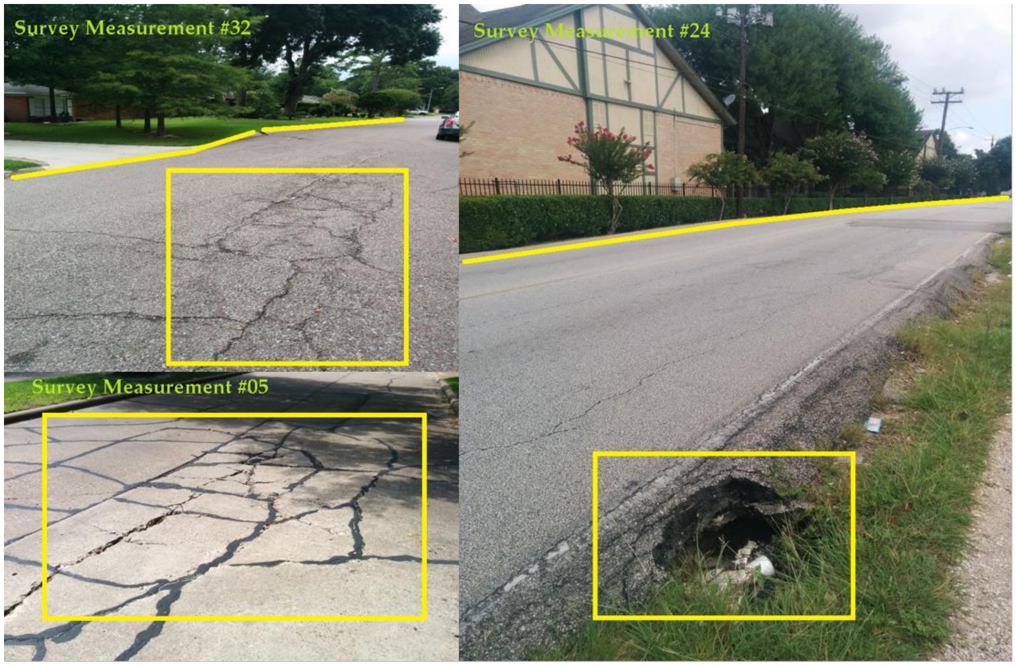

Figure 1.04: Road Damage

Examples of roads within Long-Point Fault area exhibiting cracking (yellow rectangles) and deformation (yellow lines): (A) Survey Measurement #32: West Forest Drive (Latitude: 29°46′20.71″ N, Longitude: 95°35′8.90″ W) (B) Survey Measurement #05: Panola Way (Latitude: 29°47′37.92″ N, Longitude: 95°31′35.33″ W) (C) Survey Measurement #24: Witte Road (Latitude: 29°47′30.82″ N, Longitude: 95°32′24.40″ W).

2 Geology and Tectonics

2.1 Regional Geology

Houston, Texas, is located in the Gulf Coastal Plain, nearly fifty miles from the Gulf of Mexico. The Gulf Coastal Plain, in its entirety, stretches from Mexico in the south to Florida in the east (Kasmarek and Strom, 2002) and accommodates several thousand meters of Cenozoic sedimentary deposits (Baker Jr., 1978). The intricacy of the Texas Gulf Coast Plain's geology is attributed to two factors: the spatial and temporal variability of the sediments which form the Texas coast, and the motion of Jurassic salt deposits beneath said variable sediments. Approximately one hundred and twenty-two to one hundred and forty-four kilometers in width, the Texas Gulf Coast is composed of these coastal plain deposits. Apart from Middle to Late Jurassic marine salts deposited coeval with rift sediments (Salvador, 1991), the sedimentary strata that comprise the Gulf of Mexico coastal plain are interbedded sequences of conglomerate, sandstone, siltstone, and shale (Kasmarek et al., 2009). The earliest sediments (clay, silt, sand, and gravel) in the Gulf of Mexico were deposited as the most recent supercontinent, Pangaea, rifted during the Late Triassic (Chowdhury and Turco, 2006). In spite of the rich and complex tectonic history of the surrounding region, it has been tectonically stable since the positioning of the Yucatan block at the end of the Jurassic (Salvador, 1991a).

During the Middle Jurassic, the development of the Gulf of Mexico basin allowed for the deposition of clastic, non-marine sediments as well as the Louann Salt: the most tectonically influential stratum of the Gulf of Mexico (Salvador, 1991). While the Gulf of Mexico basin had restrictive seawater flow during the Middle Jurassic, the resulting rotation of the Yucatan (Late Jurassic) allowed for intermittent seawater influx, producing massive salt deposition (Bird et al., 2005).

Tectonic activity in the area ceased in the Late Jurassic following with the end of Yucatan rotation and seafloor spreading (Salvador, 1991b). However, a convergence of sediment from the surrounding highlands of the Appalachian and Ouachita Mountains to the north, the Llano and Marathon uplifts to the northwest, and the Chiapas Massif and Maya Mountains to the south initiated rapid subsidence within the region (McFarlan and Menes, 1991; Salvador, 1991). Concurrently, structures associated with the mobilization of salt (e.g. growth faults, diapirs, pillows, and sheets) began to form (Nelson, 1991).

Despite the fact that plate-driven tectonics in the Gulf had ceased during the Late Jurassic, the major (plate) tectonic event known as the Laramide orogeny continued to be immensely influential on the structure of the Gulf (Coleman et al., 1991). Terrigenous clastic sediment transported via diverse fluvial systems, resultant from the mountain-building event, was deposited in the Gulf. Various sediment deposition areas generated regions of rapid subsidence with extensive deformation, otherwise known as sags or embayments. In response to this sediment loading, large-scale isostatic subsidence of the crust developed, thus inducing an ongoing coastward tilting of successively older depositional sequences. The immense volume of sediment deposited about the unstable, prograding continental margin further exacerbated the motion of salt structures in the underlying strata, hence varying the thickness of depositional patterns (Galloway et el., 1991).

Approximately 35 to 55 million years ago (Ma) the Laramide orogeny concluded, though sediment deposition continues presently (Coleman et al., 1991). Sequential accumulation of these sediments have prograded to the continental margin, three hundred kilometers basinward of the reef-delimited carbonate shelf edge (Galloway et al., 1991). Within the Gulf Coastal Plain are alternating deltaic and interdeltaic regions (Lohse, 1955), wherein the latter consists predominantly of barrier islands, beach ridges, coastal mudflats, and marshes. Exposed Pleistocene formations (e.g. Lissie, Willis, and Beaumont) and the overlying alluvial deposits are comprised mainly of unconsolidated sand, silts, and clays (Reid, 1973).

2.2 Salt Tectonics

Deformation and subsidence in the Gulf presently is attributed to salt deformation (Salvador, 1991b). Salt-flow structures as well as listric fault growth contribute to regional surface deformation and basin structuring (Early Cretaceous to present). Salt-flow within the Gulf Coast region is due to differential pressure gradients of sediments that overlie the salt as well as density differences allowing upward movement through younger, denser sediment (Jorgensen, 1975); furthermore, this movement can generate structures such as salt diapirs, pillows, and sheets. Listric faulting within the Gulf of Mexico is a result of coupled, differential, basinward movement of sediments situated above a decollement surface, either salt or abnormally pressured shale; additionally, gravity is the principle driving force associated to this type of faulting (Jackson and Talbot, 1986; Nelson, 1991).

Because of the large scale of salt structures in the Gulf of Mexico, the earliest depositional thickness of salt is thought to have been considerable: fifteen hundred to twenty-one hundred meters (Jackson and Seni, 1984). Significant salt-flow was required in the formation of these structures; therefore, this implies that the salt was relatively free of impurities (e.g. limestone, anhydrite, and poly-halite) since they inhibit flow. The rapid water evaporation within the basin (Late Jurassic), attributed to the arid regional climate and contributed to a depositional environment necessary to generate an extensive amount of salt (Nelson, 1991). Jurassic in age, the Louann salt is believed to underlie the entire Gulf Coastal basin and was deposited when the Gulf of Mexico was not yet completely open to the young Atlantic (Kasmarek and Strom, 2002).

The subsequent deposition of sediment situated above the Louann salt was influenced by movement from the underlying salt. This condition produces a low-angle decollement surface that decreases in angle with respect to depth from the surface of deposition until reaching a parallel bedding plane, resulting in the development of a specific type of fault, referred to as a listric fault. Occurring syndepositionally, a listric growth fault is a more accurate designation. Listric growth faults in the Gulf Coast region can either be associated with salt or shale decollements, down to the depositional stratum of the Louann salt; however, these faults can also be attributed to salt sheets, abnormal pressure differentiation, or clay mineral transitions (Nelson, 1991). Continued movement of listric growth faults are attributed to differential compaction, differential pressure, differential water loss, or a combination of the three (Bruce, 1973).

2.3 Research Area Surface Geology

The Lissie and Beaumont Formation are two geologic formations identified within the research area (Richmond, 1990). Differences in lithology and depositional setting distinguish the Lissie from Beaumont Formation. While fluvial mechanisms are inherent to the deposition of both the Lissie and Beaumont Formation, the formations laterally are discontinuous and vary slightly in composition (Meyer, 1939).

The Lissie Formation lithology comprises approximately 60% sandstone, 20% sand-clay, 10% gravel, and 10% clay (Meyer, 1939). Sandstones are described as being quartzose (SiO_2), cross-bedded, and cemented with clay. Gravels are distinguished as occurring in lenses of mainly chert and quartz; however, in some regions the gravels consists of igneous and metamorphic rock fragments. Clays, bearing similarity to Beaumont clays, appear as mottled red, orange, green, blue, and/or grey. Based on the various lithological descriptions of the Lissie Formation, the sedimentary environment suggests an alluvial environment (Meyer, 1939; Waters et al., 1955; Van Siclen, 1961).

Although the Beaumont Formation is comparable to the Lissie Formation, its significantly higher clay content and absence of gravels are distinctive. The Beaumont Formation's lithological composition includes calcareous, mottled clays, sand, and silt. Approximately 80% of the formation consists of clays in various coloring (e.g. pink, red, blue, tan, and grey). The amalgamation of river deltas, Brazos, Trinity, Neches, and Sabine compose the Beaumont Formation (Meyer, 1939; Waters et al., 1955; Van Siclen, 1961).

3 Subsidence and Faulting in the Greater Houston Area

3.1 Subsidence

Subsidence of the land surface is a major problem encountered by coastal cities worldwide (Galloway et al., 1999; Engelkemeir et al., 2010). This geological phenomenon can occur naturally or be activated (or intensified) by human activities. Sediment compaction, loading or cooling of the crust, faulting, and sinkholes exemplify naturally occurring subsidence; however, extraction of fluids from aquifers or reservoirs (e.g. water or hydrocarbons, including gases), expulsion of organic soils, and mining represent human activities that can induce or increase subsidence. Within Harris County, subsidence has the potential to complicate and/or exacerbate various hazards. Flooding susceptibility is attributed primarily to the lowering of the land surface; moreover, differential lowering of the land surface across the region potentially can disrupt drainage pathways and force precipitation runoff to be stalled (Galloway and Burbey, 2011). Subsequently, these hazards can induce damages to residential and commercial structures with the possibility of a total loss of property.

Naturally occurring subsidence is commonplace in the Gulf of Mexico basin; however, current subsidence occurs because of the unified effect of numerous natural and anthropogenic processes that are operating at multiple spatial and temporal scales (Dokka, 2004). Because of the proximity to the coast, urban infrastructure within Houston's metropolitan area has been negatively affected by subsidence since the early 1900's (Buckley et al., 2003). In order to curtail the increasing subsidence problems affecting the coastal region, the Harris–Galveston Subsidence District (HGSD) was founded in 1975. The HGSD actively monitors subsidence associated with ground water extraction in order to address historic and future subsidence predictions. Over the course of nearly four decades, the HGSD has been able to demonstrate that subsidence closely parallels groundwater use in the Houston area (Stork and Sneed, 2002; Berman, 2005; HGSD, 2013). Ultimately, the goal of the HGSD is to decrease the dependence of groundwater use across Harris and Galveston counties.

The Gulf Coast aquifer system that underlies the Harris County area consists of complex interbedded clays, silts, sands, and gravels. This system comprises five major components consisting of the following generally recognized water-producing formations (excluding the Burkeville Confining Unit). In order of increasing depth, these hydrostratigraphic units are: (1) the Chicot Aquifer, (2) the Evangeline Aquifer, (3) the Burkeville Confining Unit, (4) the Jasper Aquifer, and (5) the Catahoula (Ashworth and Hopkins, 1995; Baker, Jr., 1979).

The two shallow aquifers, the Chicot and Evangeline, constitute intermittent layers of sand and clay that are hydraulically connected; therefore, changes in the hydraulic properties of one aquifer will undoubtedly affect the properties of the other (Baker, Jr., 1979). Notwithstanding similarities in lithological composition and volume, the Chicot possesses laterally discontinuous clay-rich interbeds which are absent in the Evangeline aquifer (Leake and Prudic, 1991). The Burkeville is a regionally extensive, clay-dominated unit that restricts the vertical transmission of water; therefore, it is treated as a regional aquiclude (Knox et al., 2006) as it prevents deeper, more brackish water from reaching the potable waters of the Chicot and Evangeline (Kasmarek and Strom, 2002). Underneath the Burkeville, the Jasper and Catahoula components are rarely used in the Houston area. Despite being the deepest viable aquifer within the study area, the Jasper is separated from the two shallower aquifers by the Burkeville unit. The Catahoula only produces water from restricted sand layers near its outcrop because of the increasing depth and salinity towards the Gulf (Baker, Jr., 1979).

3.2 Faulting

Analogous with the hazardous nature of subsidence, damages in the Gulf Coast region surrounding Houston have also been associated with faulting. The first documentation of faulting in the region was part of an investigation of localized surface deformation at the Goose Creek Oil Field (Pratt and Johnson, 1926) along the east bank of Galveston Bay, thirty-two kilometers southeast of Houston. Subsequently, nearly one hundred and fifty faults have been identified and recorded within the area (Verbeek et al., 1979), though this number is believed to represent only a small portion of the true quantity (Shah and Lanning-Rush, 2005). Most fault movements in the Houston area do not release measureable amounts of seismic energy (Algermissen, 1969); consequently, the general awareness and institutional concern about the hazards of fault movement (e.g. that exists in California because of the San Andreas Fault) do not exist in the Texas Gulf Coast (Everett and Reid, 1981).

Despite the lack of seismicity, these faults constitute a considerable geologic hazard. Significant damage occurs to structures situated on the surface traces of these faults. Fault movement results in the cracking and deformation of building foundations and superstructures; moreover, service lines (water and/or sewer) are particularly susceptible to disruption by fault movement. In conjunction with the lack of seismicity and given the difficulty in mapping faults in the gulf coast plain, most faults are identified as active only after they have disrupted a manmade structure (Everett and Reid, 1981). Given the explosive growth of population of the Houston area, many more faults will inevitably be found as development expands into undeveloped lands on the outskirts of the area (Engelkemeir, 2010).

Faulting of non-lithified sediments accounts for the lack of seismicity. Specifically, fault propagation through non-lithified sediments does not allow for strain to be stored and released in an amount needed to produce noticeable seismic motion. Instead of significant seismic motion being induced, motion along the surface expression of the faults slowly slips (creep). Within the Houston area, mechanisms that actuate fault motion are not entirely understood; moreover, while temporal correlations between water withdrawal and fault slip have been observed, essentially compartmentalizing subsidence, other regions in the Houston area have displayed large water withdrawal-related subsidence depressions which are up to several square kilometers with no associated faulting. Further complicating the understanding of fault mechanisms is active salt tectonics, such as diapirism, underneath the study area. In some instances, the local fault patterns are attributed to the interactions of salt dome faults and regional faults (Cloos, 1968).

3.3 Monitoring Methods

The National Geodetic Survey (NGS) together with the Harris–Galveston Subsidence District (HGSD) have continuously collaborated to document and improve surface elevation observations along the Gulf Coast region of Texas. Techniques such as releveling (differential leveling between networks of benchmarks) and the utilization of deep borehole extensometers have provided excellent spatial data for surface elevation estimates and land-subsidence measurements. Although borehole extensometers are inexpensive compared to releveling, installation and maintenance expenses limit their geographical coverage (Berman, 2005).

The HGSD and NGS more recently have incorporated a network of GPS stations into their study of regional subsidence (Neighbors and Mitchell, 2010). GPS data allow researchers to establish positions and displacements within a specific reference frame, relating measurements to local, regional, or global scales (Abidin et al., 2008). The aforementioned network of GPS stations admit of a campaign-style GPS monitoring via Port-A-Measure (PAM) units and deep-monument continuously operating reference stations (CORS), offering increased accuracy at lower cost relative to borehole extensometers (Zilkoski et al., 2001). PAM units are trailer-mounted GPS devices that are required to stay in one location for a sufficient time to provide a statistically valid difference in height relative to three stable CORS (Zilkoski et al., 2001). In contrast, CORS are permanently fixed in one location (Berman, 2005). Additionally, the National Science Foundation (NSF) awarded the University of Houston a grant to install forty continuously monitoring GPS stations throughout the Houston area. This network, HoustonNET, will improve the spatial resolution of current GPS data.

Additional methods of monitoring subsidence include satellite aperture radar (SAR) and interferometric synthetic aperture radar (InSAR) surveys, or scenes. SAR scenes can be used to monitor large areas of land rather than a specific point; however, by differencing or interfering sequential SAR scenes, InSAR monitoring is useful in portraying and quantifying all points within a region when correlated to GPS reference stations. GPS stations alone are only capable of effectively portraying deformation at a single point; interpolation techniques must be involved to interpret larger areas. InSAR bridges gaps between GPS data successfully.

Tools and technologies used in subsidence monitoring similarly can be implemented to monitor fault movement in the Houston area. Engelkemeir (2010) investigated fault motion and surface deformation by employing PAM units, CORS, and extensometers; however, the existing network confines the monitoring of faults to those near the sparse distribution of GPS stations. Reid (1973) allocated instruments, tilt beams, and horizontal extensometers designed to monitor fault motion on several fault systems in the Houston area. Precise measurements were recorded despite the limited distribution of instruments within the area.

The USGS in collaboration with the HGSD and the Federal Emergency Management Agency (FEMA) conducted a light detection and ranging (LiDAR) scan of the Houston region in 2001 (Shah and Lanning-Rush, 2005). The intent of the LiDAR scan was to facilitate a digital elevation model (DEM) for the purpose of understanding watersheds in the area in order to prevent catastrophic flooding; additionally, the scan refined locations of principal faults mapped in the greater Houston metropolitan area (Shah and Lanning-Rush, 2005).

4 GPS and LiDAR

4.1 Introduction to GPS

The development of satellite systems for position determination, exclusively for military and intelligence applications, began in the 1960's. Satellite system objectives included providing global coverage, continuous operation in all weather conditions, the ability to serve high-dynamic platforms, and provide high accuracy. Creation of the Defense Navigation Satellite System (DNSS) program led to the consolidation of independent development efforts of each branch of military service to form a single, joint-use system. In 1973, the Navigation Satellite Timing and Ranging (NAVSTAR) GPS program was created by the U.S. Department of Defense (DOD). The NAVSTAR GPS system, commonly referred to as GPS, consists of three major segments: the space segment, the operation control segment, and the user equipment segment.

All aspects of the GPS system communicate by means of microwave radio signals; an understanding of these signals is essential for describing the relationships interior to the system as a whole. Currently operational GPS satellites broadcast two signals (designated carrier signals), each generated at a unique frequency. The application of two source frequencies allows researchers to calculate and remove common errors due to differences in signal behavior, resulting from corresponding differences in signal geometry. The first carrier signal (L1) has a frequency of 1575.42 MHz and a corresponding wavelength of 19 cm. The second carrier signal (L2) has a frequency of 1227.60 MHz and a wavelength of 24 cm (El-Rabbany, 2006). Both L1 and

L2 radio signals are generated as sinusoidal waves. In this case study, all GPS stations are capable of receiving both L1 and L2 carrier signals (Leick, 2004; Ward, 1994).

L1 and L2 signals are modulated through the addition of satellite-specific ranging and navigation codes during broadcast. The L1 signal is modulated by two codes: the Coarse/Acquisition (C/A) code and the Precision (P) code; however, the L2 signal is modulated by the P code only (El-Rabbany, 2006). Additionally, encryption of the precision (P) code for military application is designated Y code. These ranging codes are a series of binary values that contain information about the transmitting satellite (e.g. predicted position and inherent time). Errors in values immediately introduce errors into GPS positions and must be mitigated. Globally derived estimates of satellite ephemerides and clocks will facilitate the understanding of fault motion and/or subsidence within the Houston area.

The GPS constellation consists of thirty-two satellites arranged in six orbital planes centered on Earth; moreover, there is a minimum of five satellites to each orbit (Department of Homeland Security, 2013). Approximately 20,200 km above the surface, GPS satellites orbit the Earth twice a day. The 2nd Space Operations Squadron (2SOPS) at Schriever Air Force Base (Boulder, CO) is responsible for the daily command and control of the GPS constellation. Control involves the monitoring, maintenance, and navigational updates of the constellations (NCO, 2013). The cornerstone of the control segment is sixteen monitoring stations around the world. These stations continuously observe atmospheric conditions while simultaneously collecting range, phase, and navigational data (NCO, 2013). This information is uploaded to the Master Control Station (MCS) at Schriever Air Force Base.

This method of employing a network of globally distributed monitoring stations is emulated by the International GNSS Service (IGS). The IGS appropriates more than 350 continuously operating, dual-frequency GPS receivers (IGS Central Bureau, 2013) to its network. In calculating the highest quality data and products for researchers worldwide (IGS Central Bureau, 2013), there is a compromise between accuracy of the IGS products and turnaround rate. Table 4.01 presents the IGS Product Table. Concisely, accuracy of the IGS product offered is dependent on latency. Considering this study's interest in resolving the highest of accuracies, the final IGS product was chosen.

IGS Product Table			
		Accuracy	Latency
GPS Satellite Ephemerides/ Satellite & Station Clocks			
Broadcast	orbits	~100 cm	real time
	Sat. clocks	~5 ns RMS ~2.5 ns SDev	
Ultra-Rapid (predicted half)	orbits	~5 cm	real time
	Sat. clocks	~3 ns RMS ~1.5 ns SDev	
Ultra-Rapid (observed half)	orbits	~3 cm	3 - 9 hours
	Sat. clocks	~150 ps RMS ~50 ps SDev	
Rapid orbits	orbits	~2.5 cm	17 - 41 hours
	Sat. clocks	~75 ps RMS ~25 ps SDe	
Final orbits	orbits	~2.5 cm	12 - 18 days
	Sat. clocks	~75 ps RMS ~20 ps SDev	

Table 4.01: IGS Products

IGS products and their respective accuracies and latencies.

4.2 Introduction to LiDAR

LiDAR is an acronym for Light Detection and Ranging and is based on the principle of time-of-flight (TOF). Light (e.g. ultraviolet, visible, or near infrared) is emitted (via laser) in pulses that are reflected back from objects in the survey area, where sensitive detectors measure the reflected, or backscattered, pulses of light. The travel time between instrument (laser) and objects is used in combination with the location and orientation of the instrument to determine the position of every object that reflects the light (Meigs, 2013).

GPS combined with LiDAR make it possible to obtain accurate topographic maps (Schmid, Hadley, and Wijekoon, 2011). Airborne Laser Swath Mapping (ALSM) is particularly well suited to mapping linear topographic features. High measurement density, high data accuracy, fast data acquisition, canopy penetration, and a minimum amount of ground-truth data call upon the combination of LiDAR scanning with aeronautics. An ALSM system is composed of the aircraft platform (fixed-wing aircraft or helicopter), sensor, inertial measurement unit (IMU), inertial navigation system (INS), and global positioning system (GPS) control (Hodgson, 2005). In flight, INU and GPS units track and record the position and orientation of the laser. The two-way laser travel time, IMU, and GPS are integrated to determine the x, y, and z positions of each reflection (Wehr and Lohr, 1999). Reflections are returned from the ground, vegetation, and buildings; however, dependent on mapping criteria, vegetation and building returns may be removed through data processing.

Once the ALSM operation is complete, a point cloud (raw data) is produced from the laser sensor observation. The point cloud is a visual representation of the dataset captured by the sensor and consisting primarily of x, y, and z coordinates. As a result of data processing, a digital terrain model (DTM) is procured from the point cloud. The DTM, also referred to as digital elevation model (DEM), is a mathematical representation (or model) of the bare-earth surface; moreover, the model reveals the boundary between the solid ground and the atmosphere.

Collectively, LiDAR and ALSM generate accurate representations of the Earth that are used to study subtle changes in surface topography. This has proven very useful in the mapping of surface faults in the Houston area. Initially, the urban environment and the lithology of faults, often obfuscating subtle scarps, impeded the mapping of the surface expressions of faults in the region; however, in 2005, a DEM of Harris county, created by the HCFCD, facilitated in the identification of the locations of principal faults in the Houston area (Shah and Lanning-Rush, 2005). The delineation of faults was due to the subtle changes in topography observable on a kilometer scale.

5 Mapping the Surface Trace of the Long-Point Fault

Geological field mapping of the Long-Point Fault within the Houston area, in addition to surrounding fault systems (regionally), has proven to be troublesome. Specific to the vicinity of the Long-Point Fault, urban area reworking of surfaces (e.g. residential and/or city roads, driveways, and parking lots) remove indicators, such as surface deformations, crevices, and offsets, associated to faulting; furthermore, the incessant construction of residential and commercial buildings intrinsic to urban areas facilitate in the elimination of said faulting indicators. Simultaneously, considerable rainfall over time contributes to surface erosion reducing and/or erasing subtle surface features (fault scarps) indicative of faulting.

5.1 RTK GPS Field Survey

ALSM data of Harris County (2001) together with a digital elevation model (DEM) of Harris County were used in a study by Shah and Lanning-Rush (2005) that refined locations of principal fault systems in the Houston area, Figure 5.01; however, processing techniques (hill-shading) were used to detect surface faults not field investigations (Shah and Lanning-Rush, 2005). Despite this, the map rendered from the Shah and Lanning-Rush 2005 study provides the relative location of the Long-Point Fault within the Houston area, in itself essential to this study.

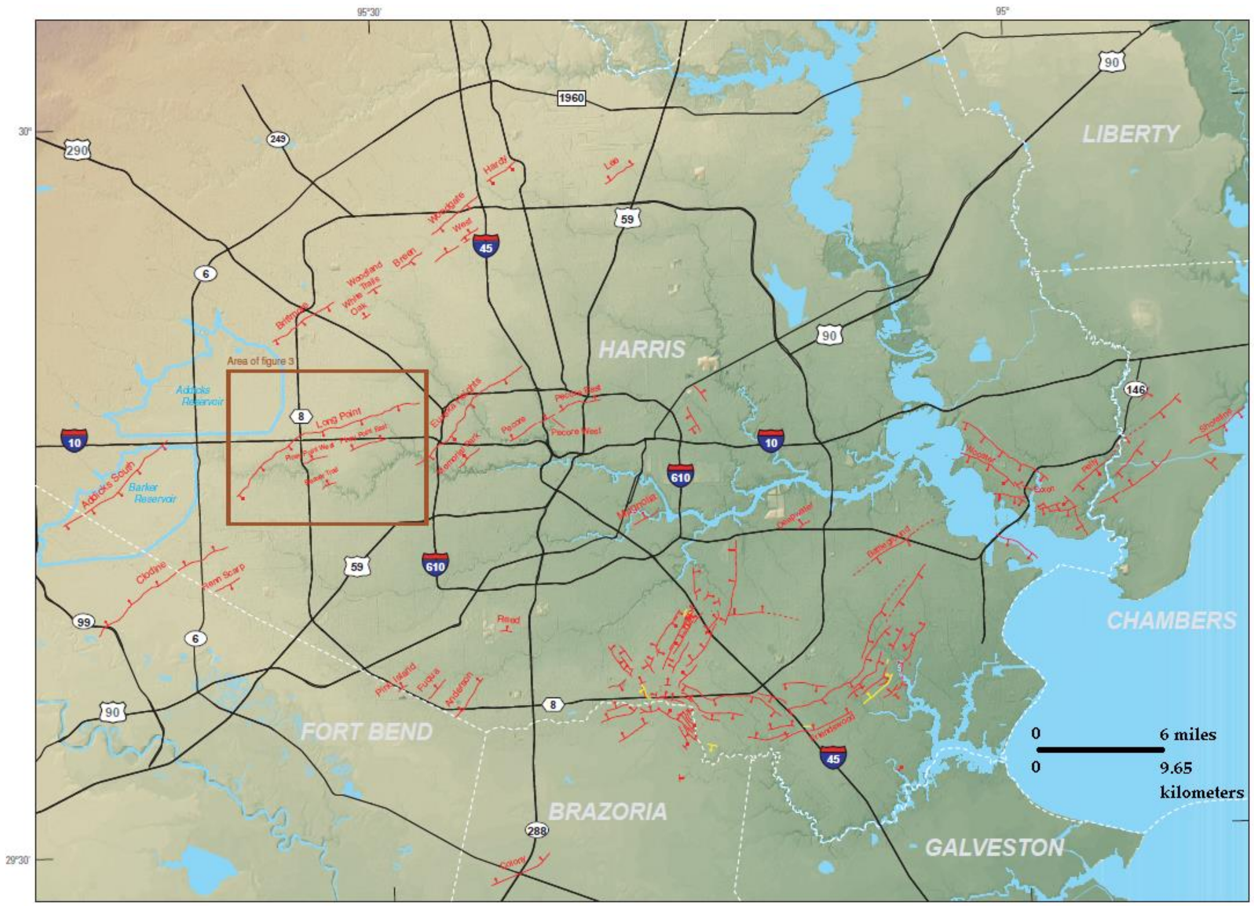

Figure 5.01: Rendered Map Delineating Principal Faults Within Gulf Coast Region

Shah and Lanning-Rush (2005) delineated principal faults within the Gulf Coast region using ASLM and DEM data.

Using the image overlay tool in Google Earth, I used latitude and longitude coordinates within Figure 5.01 to define the Long-Point Fault study area. Physical confirmation of fault damage (e.g. surface deformation, crevices, and offsets) is necessary to delineate the fault trace, as shown in Figures A.01 through A.12 in the Appendix. Fifty-two, two-minute GPS survey measurements were taken at the locations of damages attributed to the Long-Point Fault using high-accuracy kinematic GPS surveying via the Trimble R10 GNSS System. Advantageous to this study, the Trimble R10 provides real-time processed positions, either GPS or local coordinate systems, within minutes. The processed survey measurements were then exported as latitude and longitude coordinates and imported into Google Earth. Figure 5.02 uses Google Earth to display the fifty-two survey measurements conducted in this study.

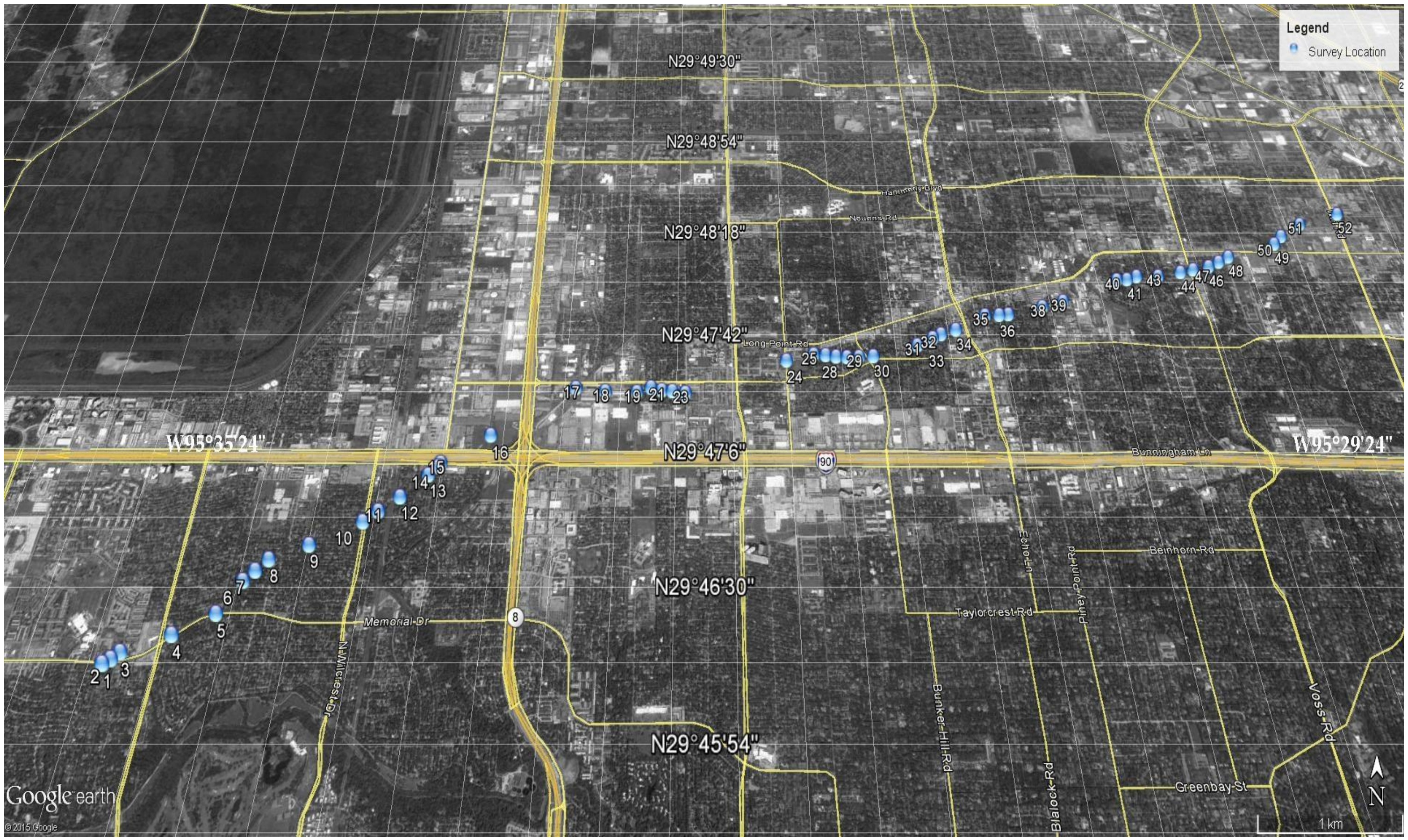

Figure 5.02: Compiled GPS Survey Locations Identifying Damage Attributed to Long-Point Fault
Fifty-two GPS survey locations (blue dots) surveyed within study area.

5.2 LiDAR Mapping

Collectively, the GPS survey locations (Figure 5.02) delineate the trace of the Long-Point Fault. Figure 5.03 features GPS survey locations superimposed on LiDAR data displayed using Generic Mapping Tools (GMT), an open-source software for processing and displaying xy and xyz datasets. Measured damage points are coincident with the fault scarp observed from the LiDAR map. By connecting all GPS survey measurements, the overall fault trace is observed to be trending southwest to northeast. The field investigations verify that the fault scarp truly represents the active fault surface trace.

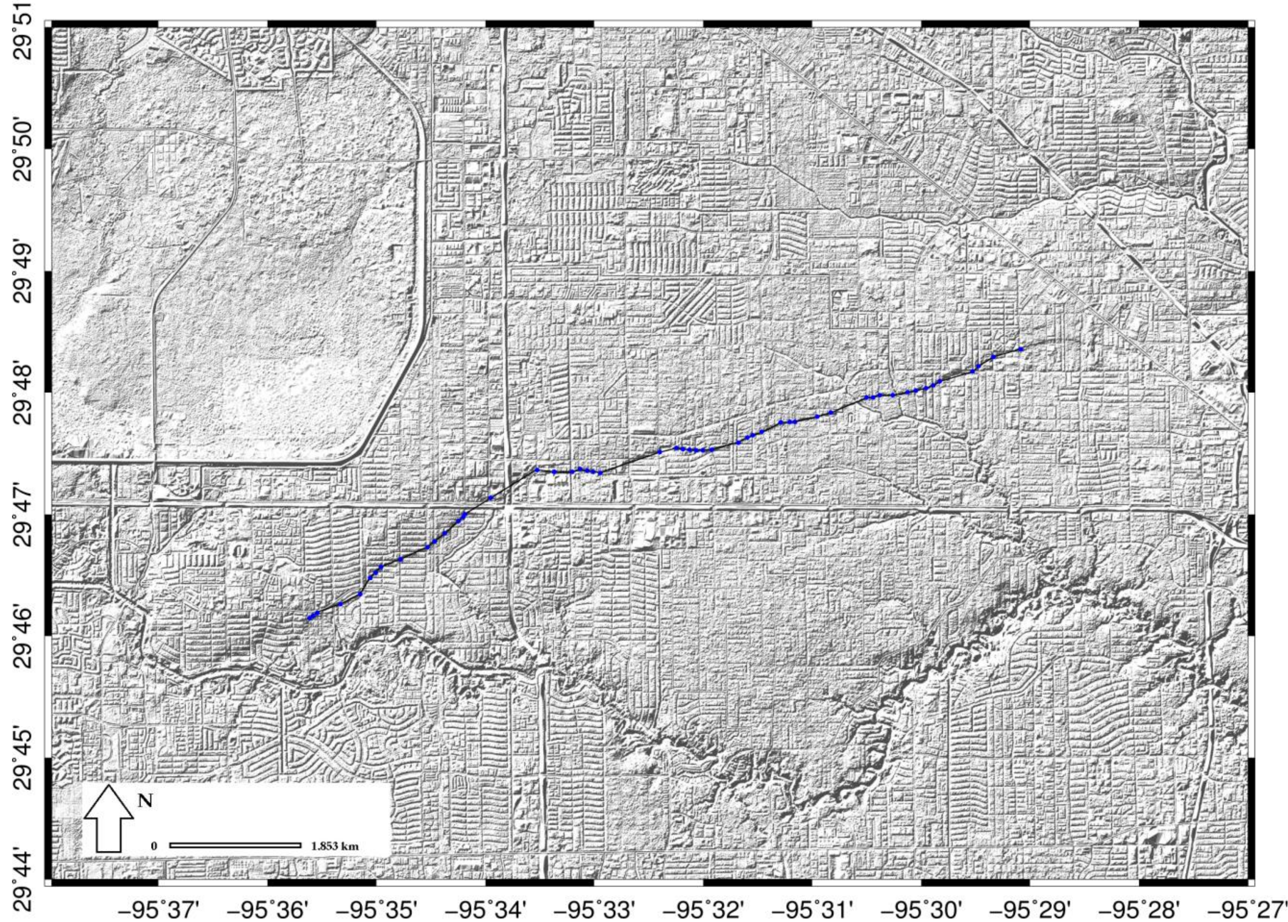

Figure 5.03: GPS Survey Measurements Interfaced with LiDAR Data

The blue points represent GPS survey locations showing relative position to fault scarp (trending southwest to northeast).

6 Current Ground Displacements along the Long-Point Fault

6.1 Introduction to the GPS and Benchmark Array

I used continuously monitoring GPS stations dispersed among varied locations on both sides of the fault in order to accurately constrain the fault kinematics. The Long-Point Fault poses unique challenges in the application of GPS. Together with the basic requirements of GPS functionality (e.g. electricity, open view of the sky, and long-term stability with respect to permanent mounting), distinctive urban area considerations must be taken into account. These considerations include permitting and/or contractual agreements, radio frequency interference within the environment, and security. In order to fulfill these considerations, it was determined that building mounted GPS stations would be ideal for this case study. Building-mounted GPS stations have specific advantages with regards to an urban environment: (1) access to electricity, (2) open views of the sky, (3) minimize the threats of vandalism and theft, (4) provide internet communication, and (5) present significant long-term stability.

Data-quality concerns as a result of building-mounted GPS stations need to be addressed as well as concerns regarding how to directly monitor ground movement, ensure station longevity, and mitigate errors caused by reflections of GPS signal (or multiple paths). Conducive to the enhancement of the quality of data acquired and addressing the aforementioned concerns, the National Geodetic Survey (NGS) guidelines regarding Continuously Operating Reference Station (CORS) GPS site installation were followed in this study (NGS website, 2015). The NGS guidelines were created in an effort to provide a set of best practices regarding installation of CORS GPS sites, ensure that the data acquired is of the highest quality, and to facilitate the proper installation of GPS stations displaying only ground motion beneath the building foundation.

NGS guidelines specifically address GPS station monumentation (e.g. considerations for location, stability, and obstructions) with the objective to avoid designs that are known to cause (or likely cause) data quality issues. These guidelines are based on designs implemented within CORS and IGS site installations over the past decade. Firstly, stability is required in antenna establishment to allow for the accurate measurement of the position and velocity correlated to a given site; this represents the crustal position and velocity of the site, not the antenna. Secondly, the monument should be designed to perpetuate its position in three dimensions, curtail the measurement of near-surface effects, and alleviate the effects of thermal expansion. Alleviation of thermal expansion is fulfilled by the avoidance of wood or metal frame buildings in preference of masonry, solid brick, or reinforced concrete buildings. Finally, to avert signal noise from the motion of buildings, heights should not be more than two stories. It should be noted that seasonal swelling and compaction of soil native to the Long-Point Fault area is usual. To mitigate this effect, large, older buildings with no visible cracks on the exterior (or interior) were chosen under the presumption that primary settling has already taken place.

Design and installation of the mount (or bracket) should be given significant consideration. While adjustable U-bolt and/or channel-lock systems are available, they are prone to gradual detachment or unlocking of the system and are therefore unsuitable for persistent stability. It is notable that material properties of the bracket, specifically the coefficient of expansion, can contribute to thermal expansion. Metals with high coefficient of expansion (e.g. aluminum) were avoided in preferment to mild steel (stainless steel), which supports stability and longevity of the bracket, Figure A.13.

Bracket location on the exterior of the building is important for bracket longevity and for extenuating movement not attributed to the crustal position and velocity of the station. Lateral attachment of the bracket should be completed using anchors, bolts, and epoxy with respect to a load bearing wall or a corner of the building. Diminishing the risk of disruption to the bracket, the location should not obstruct the building's roof in case of repairs and/or preventative maintenance; however, in order to prevent multipath errors, the location of the bracket should extend at least to half a meter above the roofline, Figure A.14.

The GNSS antenna, an integral part of the GPS station, is discussed within the NGS guidelines in considerable detail. The guidelines necessitate that a device be positioned between the bracket and antenna for appropriate leveling; however, provided the antenna needs to be exchanged, the device will allow for the recovery of the exact position in 3D space. In this study, the device (or adapter) in Figure A.15 was chosen considering its performance within the PAM network and following recommendations from HGSD. Based on specifications detailed by HGSD, the adapter is machined from a solid-bar round stainless steel and provides a leveling accuracy of 2.5 millimeter through bubble leveling. Antennas were aligned with magnetic north to maximize accuracy. Antenna cables were secured to the bracket to avoid damage to the antenna.

Another concern for consideration with respect to GPS station location is the radio frequency (RF) environment within the immediate surroundings. High-voltage power lines among other RF emitters can interfere or completely obstruct GPS satellite signals; therefore, NGS guidelines encourage avoidance to such sources.

Building selection resulted from NGS guideline criteria and/or considerations as well as contingency on overall proximity to the Long-Point Fault; however, privately owned buildings were not considered because of long-term costs associated with data communication (internet). Ultimately, educational institutions in the Long-Point Fault area were targeted; furthermore, Spring Branch Independent School District's (SBISD) abundance of campuses on either side of the fault met most if not all criteria. After permitting and/or contractual agreements were processed, SBISD campuses that were willing to participate were Meadow Wood Elementary, Wilchester Elementary, Woodview Elementary, Spring Branch Elementary, Cornerstone Academy, Ridgecrest Elementary, Treasure Forest Elementary, and Housman Elementary. Together with the SBISD campuses, Houston Community College and UTEX Industries, Incorporated agreed to participate as well.

In addition to permanent GPS stations, benchmarks established among the footwall and hanging wall of the Long-Point Fault will assist in providing enhanced spatial resolution between GPS measurements. Benchmark survey measurements lasting fifteen minutes to two hours allows for the use of NGS OPUS Rapid Static, discussed in Section 6.2. Monthly surveys of benchmarks combined with continuously monitoring GPS station data will assist in identifying possible correlations within the study area.

In this study, eleven permanent GPS stations were installed throughout the Long-Point Fault area. Five of the eleven stations (HCC1, WDVW, CSTA, TSFT, and HSMN) are on the hanging wall side of the Long-Point Fault, while the other six stations (MDWD, WCHT, UTEX, HCC2, SPBH, and RDCT) are on the footwall side. Installation of the stations on average took two days. Although some sites ultimately had nuances in regards to installation, most followed a generalized workflow as described below.

Installation of Bracket

Accessibility to the roof for colleagues assisting on the installation was required. This was for the placing of materials, such as the bracket, and tools that were required to be above the installer during the installation; however, the installer utilized a ground ladder to be in his required position. The colleagues' primary job during the installation was handling the bracket, while the installer used a hammer drill for facilitating bracket installation. In order to mock-up the bracket to the exterior wall, colleagues held the bracket in the required place while the installer marked a pilot hole with a sharpie, as shown in Figure A.16. After marking the pilot hole, the bracket was removed as it would be a safety hazard and obstruction to the installer. The installer would then drill a 3/8th inch hole into the wall (Figure A.17) and hammer a masonry anchor into the drilled hole. A bolt end is revealed through the tightening of the anchor to the wall via a wrench or socket. At this time colleagues would reposition the bracket, aligning one of the eight pre-drilled holes into the bracket to the bolt end of the anchor. A corresponding nut would then be placed on the bolt and tightened loosely allowing leeway for leveling purposes. After leveling the bracket to the ground, the nut is tightened securely onto the bolt. At this point it is necessary for colleagues to continue in assisting bracing the bracket in place. The installer continues securing the bracket with the seven remaining anchors, as shown in Figure A.18.

Installation of the penetration hole

With the bracket in place, the installer marks a location close to the bracket for a pilot hole. A pilot hole (or small-diameter hole) significantly helps in the drilling of a much larger hole. After drilling the pilot hole from the exterior of the building to the interior, the drilling bit is changed to a one-inch drilling bit and placed upon the pilot hole. A one-inch diameter hole is then drilled into the interior of the building, as shown in Figure A.19. Upon confirmation that the penetration hole has reached the interior of the building, a wooden dowel is used to measure drilling depth from the exterior to interior. With this measurement, 5/8-inch to 7/8-inch steel pipe is cut and inserted into the penetration hole with light hammering; this is specifically done for the ease of cable feedthrough.

Installation of antenna

The adapter (Figure A.15) is attached to the top of the bracket and oriented to magnetic north. Light hammering of the adapter is recommended in order to be “flush” or horizontal with the bracket; afterwards, this is confirmed with a level. After leveling, the adapter is secured to the bracket with a set screw. An Allen key is used to tighten the set screw. At this time, the GNSS antenna is placed onto the bracket via the adapter. Before the installation of coaxial cable to the antenna, the cable is unwound in order to release torsion. During this step, the coaxial connection opposite the ninety-degree connection is cut-off; this connection will be rebuilt later. Total length from the antenna coaxial connection to the penetration hole is measured and used to cut flexible conduit to length. The coaxial cable is then inserted into the previously cut conduit. At this point, the ninety-degree connection is connected to the antenna and temporary restraints (zip ties, duct tape, or both) are attached around the conduit and secured to bracket.

Installation of Exterior Junction Box

Before the installation, the lid of the junction box is removed with a Philips-head screwdriver. Two one-inch diameter holes are drilled, located on top and on the back of the junction box. The installer holds the junction box over the penetration hole and aligns the one-inch diameter hole to the penetration hole. For mounting purposes, tabs on each side of the junction box have pre-drilled holes for screw attachment to the exterior wall. The installer marks these holes for drilling and for the placement of flexible anchors. These marks are drilled with a 3/16-inch bit followed by the insertion of anchors that are lightly hammered, where the alignment of the junction box to anchors enables screws to be inserted and tightened. Next, the installer takes the end of the conduit containing the coaxial cable that has a female hose fitting attached. Similarly, a male hose fitting is inserted and secured to the top of the junction box. At this point, both female and male hose fittings are attached to each other, creating a water-tight seal. The coaxial cable can now be inserted into the steel pipe within the penetration hole, leading into the interior. The cover to the junction box is now replaced and all screws are secured, as shown in Figure A.20. Exterior installation is finalized by laying down a silicon bead over everything installed in order to seal and protect, thus enhancing longevity.

Installation of the Receiver

An electrical cable junction box is used as a compartment for the receiver. Three one-inch holes are drilled into the junction box: two on top and one on bottom. The electrical cable junction box is mounted using four flexible anchors, one at each corner, similarly to the method used in installing the bracket. Once mounted, the receiver is secured inside the junction box. This is done using quarter-inch screws secured into the junction box. The coaxial cable is then inserted into one of the top holes of the junction box. A re-head (a new end connector is mounted) of the coaxial cable end is performed for connection to the receiver. Assuming that an internet connection is available, a RJ45 cable is connected through the last of the predrilled holes on top of the junction box to the receiver. The power adapter can now be placed within the junction box and connected to the receiver. The electrical plug is fed through the bottom predrilled hole of the junction box to an electrical outlet, as shown Figure A.21. At this point, installation of the GPS station is complete. Figures A.22–A.24 display the eleven permanent GPS stations installed within the study area, while Figure 6.01 displays all permanent GPS stations onto a rendered LiDAR map of the study area.

Installation of Benchmarks

Given that the total length of the Long-Point Fault is sixteen kilometers, it was decided to segment the fault trace to one kilometer intervals. Thirteen areas (or sites) were identified for possible benchmark installation. Each site would have two associated benchmarks: one relative to the footwall side and the other to the hanging wall side.

Upon careful inspection and consideration (e.g. benchmark position to fault trace, open view of the sky, and safety) twenty-six benchmarks were installed. The installation process entails drilling a 3/16-inch hole approximately two inches into concrete and/or asphalt road, injecting fast-setting epoxy formulated for concrete and all weather conditions, and inserting a 1-1/4-inch galvanized screw into the drilled hole. The epoxy was allowed to set overnight; furthermore, initial surveying of the benchmarks could not be performed till epoxy had completely set, therefore geotagged pictures allowed for the relative position of benchmarks to be referenced later for survey measurement. Upon leaving the benchmark sites, green fluorescent paint was used to identify the benchmarks. Figures A.25–A.30 show various benchmark installations along the foot wall and hanging wall side of the Long-Point Fault. Benchmarks are designated JSXX (Figure 6.02), where XX signifies continuous numbering from 01 to 26; odd numbers represent benchmarks on the footwall side, while even numbers represent benchmarks on the hanging wall side. Figure 6.03 discloses benchmark locations with respect to permanent GPS station interfaced with LiDAR data.

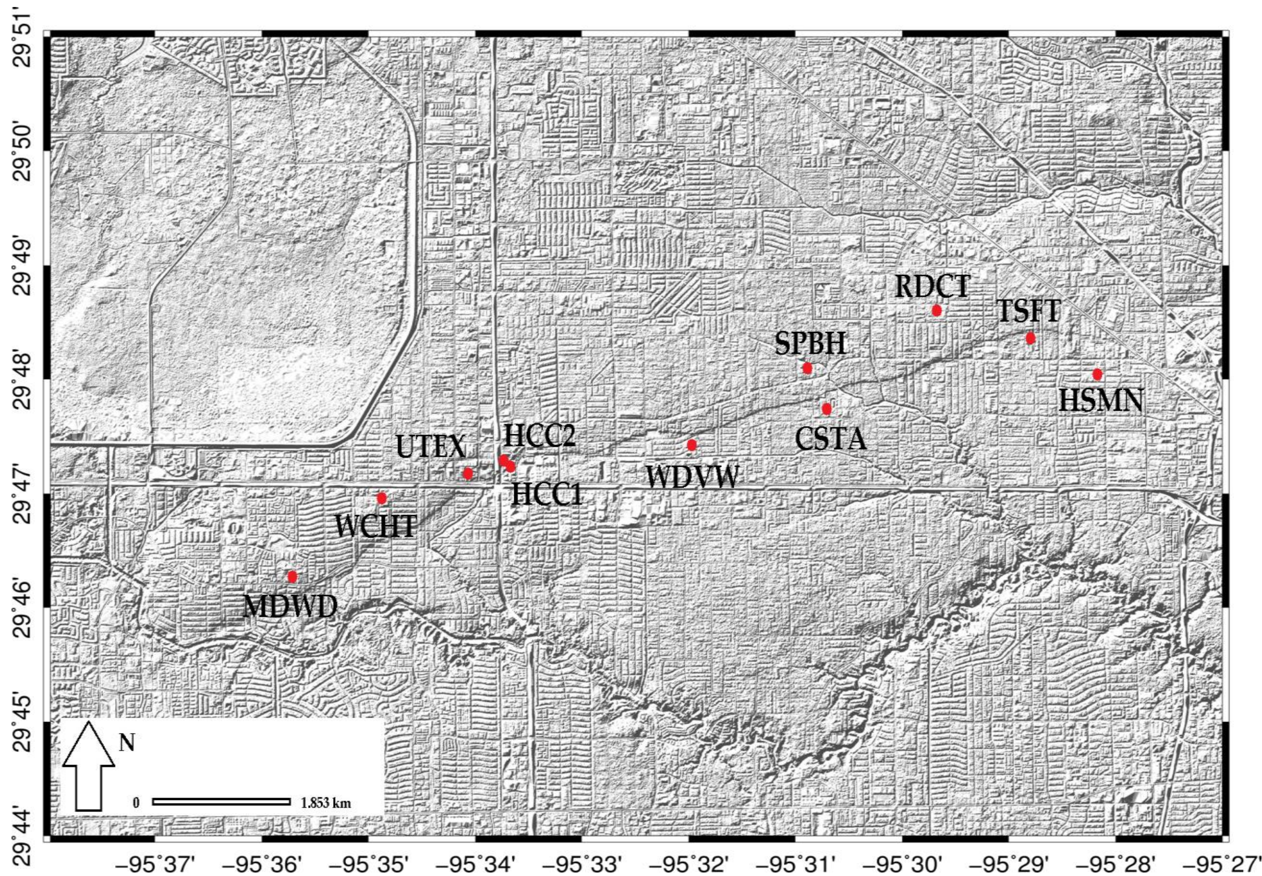

Figure 6.01: Overall Installed GPS Stations Along Long-Point Fault

Eleven GPS stations (red dots) were installed along the fault trace of the Long-Point Fault; six GPS stations (MDWD, WCHT, UTEX, HCC2, SPBH, and RDCT) were installed on the footwall side, while five GPS stations (HCC1, WDVW, CSTA, TSFT, and HSMN) were installed on the hanging wall side.

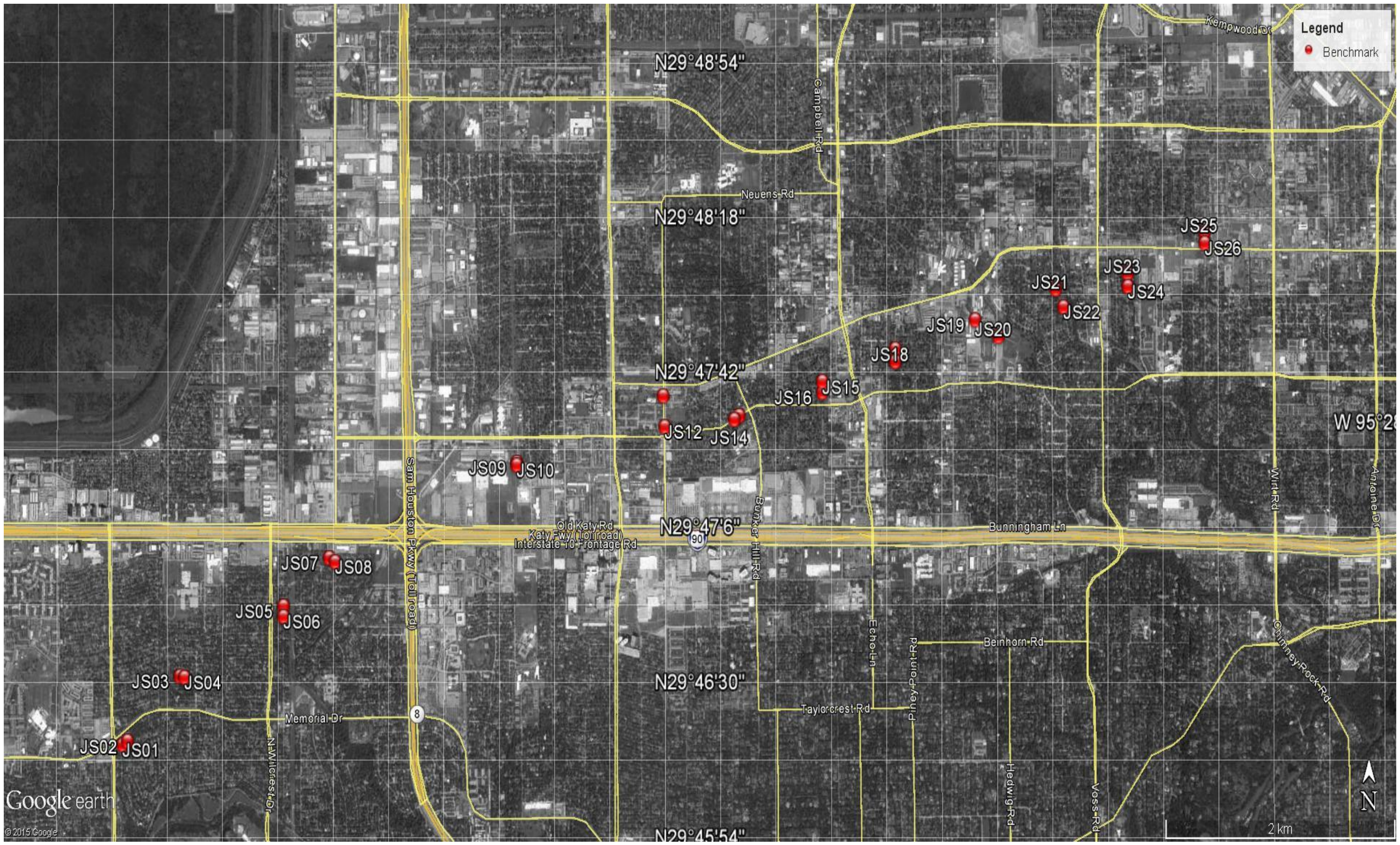

Figure 6.02: Overall Installed Benchmarks (JS01–26)

Twenty-six benchmarks (red circles) were installed along the fault trace of the Long-Point Fault; odd numbers represent benchmarks on the footwall side, while even numbers represent benchmarks on the hanging wall side.

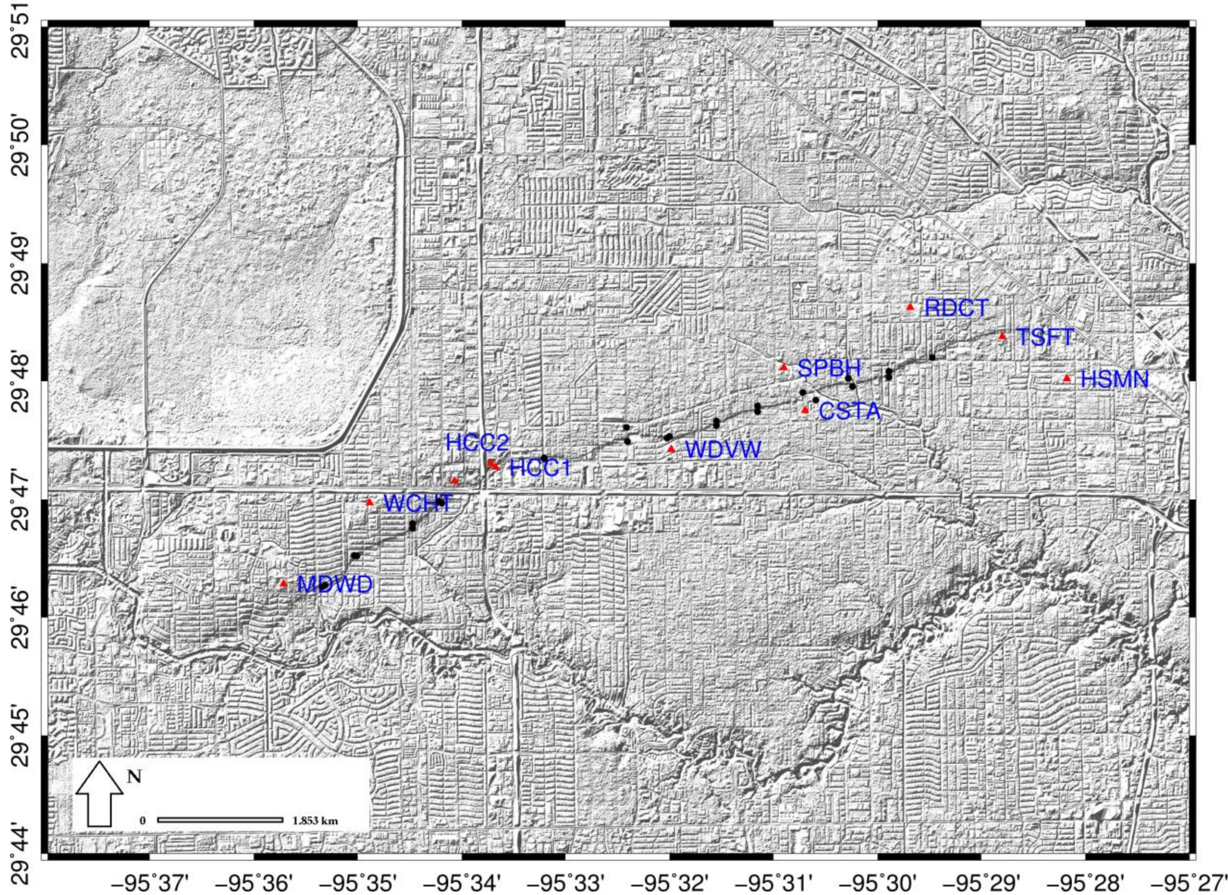

Figure 6.03: Permanent GPS Stations and Benchmarks Interfaced with LiDAR data

Eleven GPS stations (red triangles) and twenty-six benchmarks (black circles) show relative position to the fault trace of the Long-Point Fault.

6.2 Relative and Absolute Displacement

Methods such as relative positioning (double-difference) and absolute positioning (Precise Point Positioning or PPP) are used to convert raw data into relative and absolute positions, respectively. Both double-difference and PPP techniques were used in this study and the methods employed will be described here.

Relative Position Processing

Application of the double-difference technique requires a minimum of two receivers: one "rover" station with an unknown position and at least one reference station whose position is known (Gao and Chen, 2004). To compensate for common errors, these stations must observe identical satellites concurrently. Through the analysis of various series of measurements made separately by unique receiver–satellite pairs, identification of mutual errors due to hardware bias are differenced and significantly reduced. The reduction of errors substantially increases as the distance between reference station and rover station decreases (baseline length); furthermore, an increase in the number of reference stations facilitates a decrease in the amount of error (Firuzabadi and King, 2012) as well as the number and geometries of available satellites (Wang, 2010). While several publically accessible software packages and internet-based services utilizing the double-difference technique exist, this study specifically employs Topcon Tools and the Online Positioning User Service (OPUS), a commercial software package and a web-based processing service, respectively.

The Topcon Tools (v.8.2.3) software package developed by Topcon Positioning Systems, Inc., provides single-base post-processing, network analysis, and adjustment of GPS data. In post-processing static GPS data, three-component translational distances (NS: North to South; EW: East to West, and Vertical) between the reference station (UTEX) and the remaining ten observation stations along the Long-Point Fault were calculated. Of importance to this study, single-base post-processing (with L1 and L2 frequencies) between observation and reference stations less than ten kilometers in length can achieve sub-centimeter horizontal and vertical accuracies. Baseline lengths between reference station (UTEX) and observation stations constituting the study averaged five kilometers.

The Online Positioning User Service (OPUS) is an automated, web-based, GPS data post-processing service that provides its users with accurate and reliable positional coordinates (Weston et al., 2007) by processing user data with a set of control stations: (three) automatically selected from the CORS network, managed by the National Geodetic Survey (NGS). While different data-processing methods dependent on the duration of the data session submitted are available (static vs. rapid static), this study utilizes the static processing method (OPUS-S), specifically for data session durations greater than two hours. OPUS is capable of computing highly accurate geospatial coordinates from a single GPS data file provided by the user (Wang and Soler, 2013); resultant positional coordinates, averaged estimates between three single-baseline solutions, are automatically emailed to the user within minutes.

GPS data processed using Topcon Tools and/or OPUS require a conversion from raw data format (native to GPS receiver) to a Receiver INdependent EXchange (RINEX) format. This standardized format developed by the Astronomical Institute of the University of Berne allows for the uncomplicated exchange of GPS data (Gurtner, 2007). Processing results for this study are exported and tabulated via Excel for presentation using CoPlot.

Absolute Position Processing

Precise Point Positioning (PPP) is an absolute positioning technique using un-differenced, dual-frequency pseudo-range and carrier-phase observations along with precise satellite orbit and clock information to determine position from a single GPS receiver (Kouba, 2005). Aspects of the GPS constellation system (e.g. satellite orbit and clock information) estimated from the allocation of a global network of stations can be correlated to an individual station that did not contribute to said estimates. Use of the PPP technique provides a significant improvement to position accuracy in instances where baseline length restricts the accuracy of measurements via the double-difference technique or when studies of regional features are desired (Zumberge et al., 1997).

Analogous to the availability of several publically accessible software packages and internet-based services utilizing relative position processing, various software packages are available that employ absolute position processing; however, this study will only consider the software package GNSS-Inferred Positioning System and Orbit Analysis Simulation Software (GIPSY-OASIS). GIPSY-OASIS (v.6.2), or GIPSY for short, was used in its Precise Point Position mode, which generates positions with single-receiver phase-ambiguity resolution (PPP-SHPA).

GIPSY is capable of generating an ambiguity-resolved precise position from a single receiver using final satellite orbits and clocks provided by the International GNSS (Global Navigation Satellite System) Service (IGS) and wide lane and phase bias estimates provided by the Jet Propulsion Laboratory (JPL). Operations within GIPSY allow for the input and specification of various parameters in order to achieve the highest precision.

PPP processing characterizes a modified differencing technique; however, rather than examining transmitter–receiver pairs (akin to relative positioning), GIPSY combines the single-receiver data with a globally generated list of biases. The ambiguity-resolved solutions have demonstrably improved precision, most notably in the East–West (EW) direction (Wang and Soler, 2012). Employing GIPSY, Bertiger et al. (2010) tested and demonstrated repeatable daily solutions (twenty-four hour sessions) of approximately two millimeters in the northing and easting directions and six millimeters with respect to the vertical direction.

GPS Accuracy and Removal of Outliers

Intrinsic error sources of the GPS system (e.g. phase ambiguity bias, clock inaccuracies, incorrect ephemeris, and signal delay) can be corrected or estimated by utilizing current processing techniques as illustrated in this case study. An estimation of the number of wavelengths between the transmitter and receiver are required to process

GPS carrier phase data. Through the stripping of modulations, thus isolating waveforms, distances are calculated using carrier signals transmitted from GPS satellites (Remondi, 1985). Ideally, the number of cycles (wavelengths) transmitted and received increases linearly with time; moreover, there would be no variation in the rate of signal propagation. In reality, GPS is a system in motion and signals do not function in a perfectly linear manner. The process of accurately estimating this number of wavelengths is now known as bias optimization (Blewitt, 1989).

Ephemeris errors occur when predicted (or modeled) positions of satellites do not correctly align with true positions. While the difference between the predicted and actual position is defined, the effects of this discrepancy will reveal themselves differently based on the viewing angle of any particular receiver. Fortunately, short-baseline observations may negate these effects (El-Rabbany, 2006); as the distance between monitoring stations decreases, the accuracy of their ephemeris estimates improves. In order to generate accurate positions, extremely precise ephemeris data are essential.

Ephemeris data are acquired from the IGS in order to improve the International Terrestrial Reference Frame (ITRF), measure deformations of the Earth's surface, and determine atmospheric parameters such as ionospheric and tropospheric conditions. These tools are integral for establishing the precise point positions used within this study.

Ionosphere and troposphere conditions result in carrier signal delay that must be corrected. Overall tropospheric delays are due to both hydrostatic and wet parameters (Davis et al., 1985). Hydrostatic delay (dependent on surface pressure) is responsible for approximately ninety percent of total observed delay (Bar-Sever et al., 1998); however, wet delay (dependent on the dipole component of atmospheric water vapor) is far more variable (Davis et al., 1985).

With respect to the receiver, tropospheric delay both varies in zenith path and azimuthal (horizontal) directions. As the elevation approaches the zenith, the magnitude of the horizontal variations decreases (Bar-Sever et al., 1998). Bar-Sever et al. (1998) showed that repeatability of coordinates improved when gradients were modeled using a random-walk process and a relatively low elevation cutoff of seven degrees; this method was used in the current study.

The Vienna Mapping Function (VMF), designed by Boehm and Schuh (2004), was introduced to simplify the modeling of tropospheric delay explicitly. Advantages of VMF1 (the most recent VMF model) include improved constraints on the hydrostatic portion of the delay while simultaneously employing a mapping function that is dependent on latitude and day of year (Boehm and Schuh, 2004). In this study, the delay attributed to the troposphere was modeled using the VMF1 mapping model. Utilizing this model has shown improved vertical repeatability of ground station coordinates (Bertiger et al., 2010).

Additional atmospheric effects on signal transference are attributed to ionospheric delay (i.e., first and second order). First-order ionospheric delay is contingent on various factors (e.g. solar activity, local time of day and season, and satellite elevation) with distinct severity; however, second-order ionospheric delay results in errors on the centimeter to millimeter scale. As GPS solutions improve in repeatability, these seemingly small errors become relatively large. Reduction of motion attributed to seasonal variations and improved station-coordinate repeatability are the result of correcting for second-order ionospheric delay (Kedar et al., 2003).

Displacements caused by solar and lunar tides effect the solid earth, hence the positions of orbiting satellites; however, these effects can be modeled using an internet-based software system. The Ocean Tidal Loading interface, operated by Chalmers University's Onsala Space Observatory (OSO) in Sweden, allows users to select their preferred tidal model. This study utilizes the FES2004 atlas, the most current FES (Finite Element Solutions) atlas. Major diurnal and semi-diurnal tides are calculated with internal and well-established algorithms inherent to FES2004. The calculated values are then correlated with altitude data gathered by altimetry satellites (Lyard et al., 2006).

Once the GPS data have been processed, it is essential that outliers be removed. The GIPSY processing method generates sigma values (standard deviations from the mean of all values measured that particular day) for each daily position. Outlier removal is dependent on the analysis of sigma values over time, not on a daily basis. Standard deviations derived from unacceptable data are presumably larger than of their neighbors (e.g. because of daily positions that might have been corrupted by multipath propagation, inaccurate estimation of delays, or cycle slip) resulting in greater variability in high-frequency measurements. With iteration, analysis of sigma values over time will distinguish outliers for removal.

Outlier identification and removal in this study is adapted from previous work by Wang (2011). A local reference frame of nearby stations was employed and any positions beyond their directionally respective "two times average sigma" range are treated as outliers. Similarly, this study takes average daily values collected for each position component (Northing, Easting, and Vertical), and the daily positions beyond twice the average daily sigma were treated as outliers and removed.

Reference Frames

All positions must be presented relative to a well-established reference frame; however, as mentioned previously, one of the shortcomings of GPS observations is the lack of spatial coverage. Despite this, modern processing techniques allow researchers to achieve millimeter-scale precision, though these positions cannot extend beyond the observation point. The Houston–Galveston region has referenced surface GPS positions (and velocity vectors) for isolated, yet stable, deep-monument CORS stations. An alternative to this baseline-pair approach is to use the observed motion of stable sites to generate the orientation, origin, scale, and time-dependency of a local reference frame (Wang, 2013). All observations referenced to this frame will readily illustrate the internal, or local, deformation for the study area that is not affected by any regional motion.

A stable reference frame must be employed in order to relate GPS positions and displacements to earth processes (Bawden et al., 2012). Processing GPS data with GIPSY generates solutions referenced to the Earth-centered, Earth Fixed International GNSS Service Reference Frame, the most current version being IGS08. The IGS08 reference frame is suitable when considered in light of the global availability of the IGS products, processing software such as GIPSY, BERNESE, GAMIT, etc., and GPS data in general.

The increase in localized (specific) use of GPS studies has resulted in a comparable increase in the establishment of local or regional reference frames (e.g. the North American Datum of 1983 (NAD83), the European Terrestrial Reference Frame of 1989 (ETRS89), and the Geodetic Datum of Australia of 1994 (GDA94)) (Soler and Snay, 2004; Soler and Marshall, 2003). These reference frames have been created owing in part to researchers needing to demonstrate local (or intra-regional) processes rather than global-scale processes. The implementation of a regional reference frame greatly improves the utility and comprehension of GPS-derived positions (Wang, 2013b).

For this study, a local reference frame called the Stable Houston Reference Frame (SHRF) (Wang, 2013b) was employed for the investigation of GPS-derived time series, Figure 6.04. This local frame allows researchers in the Houston–Galveston area to analyze the intra-regional deformation due to subsidence, fault motion, salt tectonics, etc., in a site-specific manner (Wang, 2103b). Through the use of a 14-parameter Helmert transformation, IGS08-referenced positions can be represented in the local reference frame. This transformation is described in this section and follows the methodology and definitions of previous studies (e.g. Wang, 2013b; Soler and Snay, 2004).

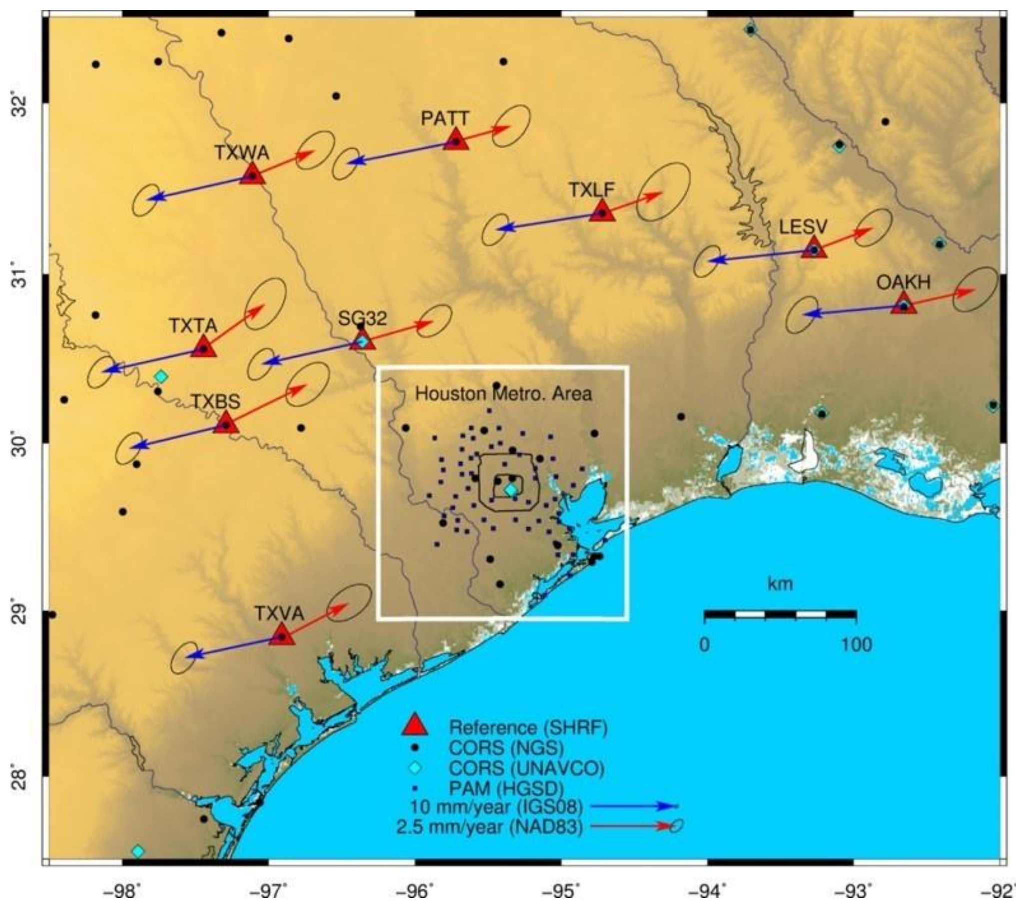

Figure 6.04: The Stable Houston Reference Frame (SHRF)

This map shows the locations of nine frame sites that constitute the stable Houston reference frame (SHRF).

In 1994, the IGS began formatting its precision products within the International Terrestrial Reference Frame (ITRF). The ITRF is the most comprehensive geocentric coordinate system employed by the GPS community (Kouba, 2002). Over time, the coordinates within the ITRF have improved and sequential realizations that have been determined (e.g. ITRF92, ITRF94, …, ITRF08). As the ITRF is updated, IGS products must be updated simultaneously so that the precise orbits and clocks remain relevant to ITRF realizations. Since 2000, the sequential iterations of the ITRF have not significantly impacted the IGS; moreover, the most recent iteration (ITRF05 to ITRF08) indicated internal ITRF translational stability (Ray et al., 2011).

In 2011, the IGS adopted its most current reference frame—IGS08—which replaces the previous reference frame (IGS05). This new realization is based on the current ITRF08 frame. Since 2000, the IGS has defined its own unique, global reference frame based on the most current ITRF realizations (Ray et al., 2011). Currently, all IGS products cite the IGS08 reference frame.

Transformation to a Local Reference Frame (SHRF)

In order to sufficiently determine localized, intra-regional surface displacement, the globally derived IGS08 reference frame must be transformed into a local reference frame. The parameters in the following equations are defined as functions of time. This time-dependency allows the transformation process to accommodate any change in position coordinates through time.

SHRF Transformation Equations:

$$X(t)_{SHRF} = T_X(t) + [1 + s(t)] \cdot X(t)_{IGS08} + R_Z(t) \cdot Y(t)_{IGS08} - R_Y(t) \cdot Z(t)_{IGS08}$$

$$Y(t)_{SHRF} = T_Y(t) - R_Z(t) \cdot X(t)_{IGS08} + [1 + s(t)] \cdot Y(t)_{IGS08} + R_X(t) \cdot Z(t)_{IGS08}$$

$$Z(t)_{SHRF} = T_Z(t) + R_Y(t) \cdot X(t)_{IGS08} - R_X(t) \cdot Y(t)_{IGS08} + [1 + s(t)] \cdot Z(t)_{IGS08}$$

In these equations, $X(t)_{IGS08}$, $Y(t)_{IGS08}$, and $Z(t)_{IGS08}$ represent the X, Y, and Z position coordinates of the ground station at time t, calculated using GIPSY (referenced to the IGS08 frame). Comparably, $X(t)_{SHRF}$, $Y(t)_{SHRF}$, and $Z(t)_{SHRF}$ represent the X, Y, and Z position coordinates of the ground station, at time t, within the Earth-centered, Earth-Fixed coordinate system of the Stable Houston Reference Frame.

The equations also demonstrate that the X, Y, and Z coordinates in the IGS08 frame are transformed into the SHRF through (1) a translation along the respective axis, represented by the terms $T_x(t)$, $T_Y(t)$, and $T_Z(t)$, (2) differential scalings of the respective axes, denoted by the s(t) terms, and (3) counterclockwise rotations around the remaining two axes, shown as terms $R_x(t)$, $R_Y(t)$, and $R_Z(t)$ (Wang, 2013b). Table 6.01 provides the values of these fourteen parameters for both the transformation of IGS08 into SHRF as well as the transformation of IGS08 into NAD83, a regional reference frame. Comparing GPS results in three different reference frames allows for an in-depth investigation of motions at varying scales. With the detailed history available in the Houston–Galveston region, the SHRF transformation was able to account for all seven parameters and their rates.

Transformation Parameter	Unit	IGS08 to SHRF t_0 = 2012	IGS08 to NAD83(2011) t_0 = 1997
$T_x(t_0)$	cm	0.00000	99.34300
$T_y(t_0)$	cm	0.00000	-190.33100
$T_z(t_0)$	cm	0.00000	-52.65500
$R_x(t_0)$**	mas***	0.00000	25.91467
$R_y(t_0)$	mas	0.00000	9.42645
$R_z(t_0)$	mas	0.00000	11.59935
$s(t_0)$	Ppb****	0.00000	1.71504
dT_x	cm/year	-1.07250	0.07900
dT_y	cm/year	-1.05876	-0.06000
dT_z	cm/year	-3.54574	-0.13400
dR_x	mas/year	1.15720	0.06667
dR_y	mas/year	-0.93885	-0.75744
dR_z	mas/year	-0.33224	-0.05133
ds	Ppb/year	1.37220	-0.10201

*Source: (Wang, 2013b), Table 2; Pearson and Snay (2013), Table 7
**Counterclockwise rotations of axes are positive.
***mas = milliarc second.
radians to mas coefficient: 206264806.24709636;
mas to radians coefficient: 4.848137E-09.
**** ppb=parts per billion

Table 6.01: Fourteen Parameters for Helmert Transformation

Parameters for similarity transformations from IGS08 to SHRF (Wang, 2013).

The values for all seven transformation parameters can be defined after Pearson et al. (2010) as:

$$T_X(t) = T_X(t_0) + T_X' \cdot (t - t_0)$$

$$T_Y(t) = T_Y(t_0) + T_Y' \cdot (t - t_0)$$

$$T_Z(t) = T_Z(t_0) + T_Z' \cdot (t - t_0)$$

$$R_X(t) = R_X(t_0) + R_X' \cdot (t - t_0)$$

$$R_Y(t) = R_Y(t_0) + R_Y' \cdot (t - t_0)$$

$$R_Z(t) = R_Z(t_0) + R_Z' \cdot (t - t_0)$$

$$s(t) = s(t_0) + s' \cdot (t - t_0)$$

The time dependency of these equations is explained through a linear relationship with a fixed initial value, defined at a specific epoch denoted as t_0. The value t_0 is a constant; therefore, $T_X(t_0)$, $T_Y(t_0)$, $T_Z(t_0)$, $R_X(t_0)$, $R_Y(t_0)$, $R_Z(t_0)$, and $s(t_0)$ will also be constants. The values for the second set of seven parameters (T_X', T_Y', T_Z', R_X', R_Y', R_Z', and s') can be defined after Pearson et al. (2010) as time derivatives (or velocities) of the original seven parameters; thus, providing the rate of change for translation, rotation, and scaling with respect to time (Soler and Marshall, 2003).

GPS Positional Time Series

The scope of this study intends to reveal current ground motions using daily solutions from continuously monitoring GPS stations by applying relative and absolute position processing. Processed daily solutions were normalized prior to being graphed with CoPlot. Specific to all data presented in this study, the implementation of normalization to the average was preferred; furthermore, this brought displacement value distributions into alignment.

In Figure 6.05, all GPS stations were referenced to UTEX for Topcon Tools processing. Of all GPS stations installed along the Long-Point Fault, UTEX has the longest continuous dataset, nearly two and a half years; also, the relative position of UTEX with respect to other GPS stations provides baseline lengths less than ten kilometers. Figure 6.05 reveals that baseline distance to UTEX affects repeatability (precision); moreover, the stations closest to UTEX had higher precision, while stations further away from UTEX displayed somewhat lower precision. All stations exhibited a reverse trend to UTEX. This reverse trend shows relative movement of the corresponding station to the absolute position of UTEX (top of Figure 6.05). Figure 6.06 and Figure 6.07 also display footwall side GPS stations and hanging wall side GPS stations relative to the absolute position of UTEX, respectively. Overall, no considerable relative movements were observed in all three directions for all GPS stations. Additionally, Figures 6.08–6.11 present various GPS stations on the hanging wall side referenced to various GPS stations on the footwall side of the Long-Point Fault. All figures show strong seasonal signals with no considerable relative movement in all three directions.

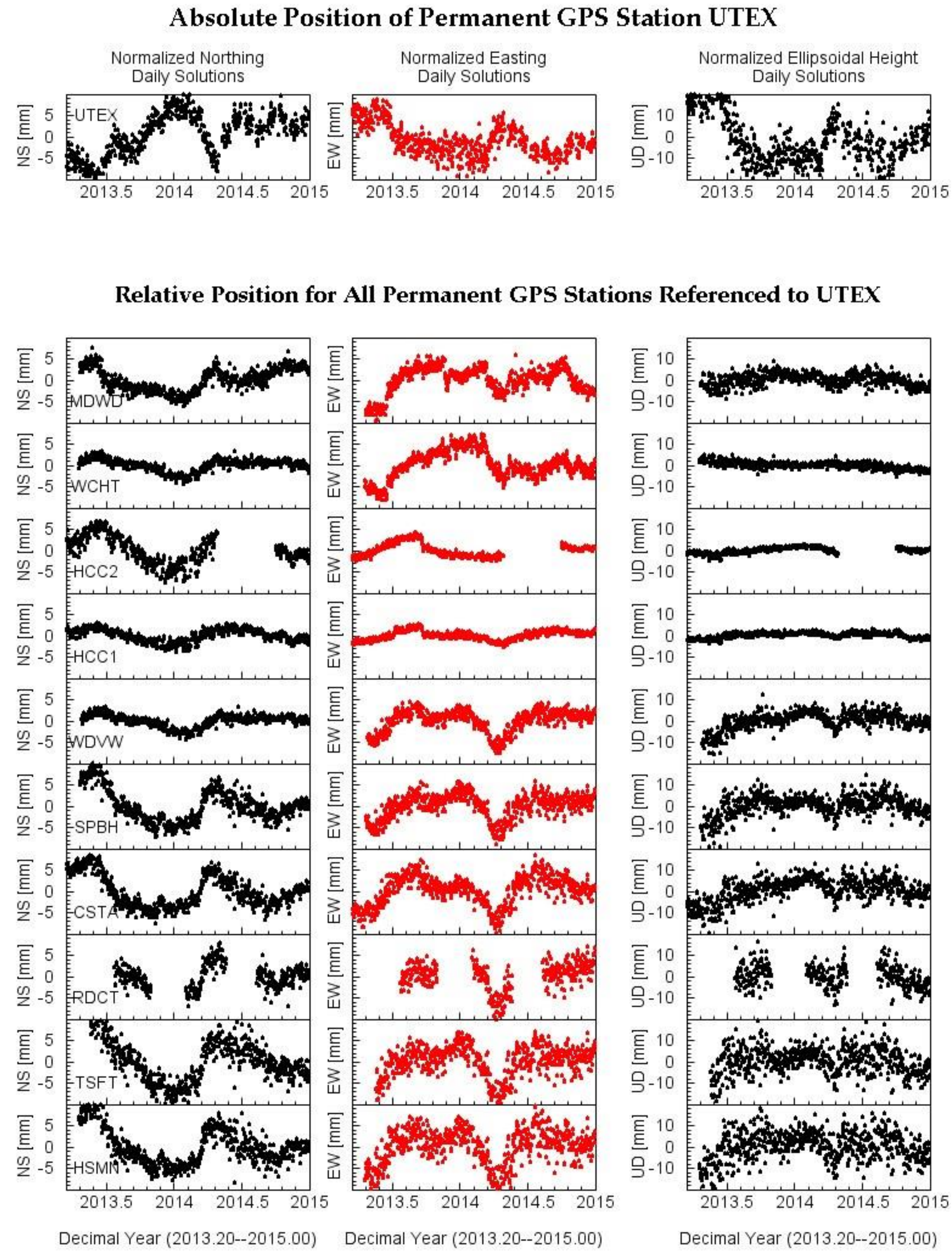

Figure 6.05: Time Series for All GPS Stations Referenced to UTEX

Time series comparison of all GPS stations referenced to UTEX using the double-difference technique via Topcon Tools software. (North = positive NS, South = negative NS, East = positive EW, West = negative EW, rebound = positive UD, and subsidence = negative UD.)

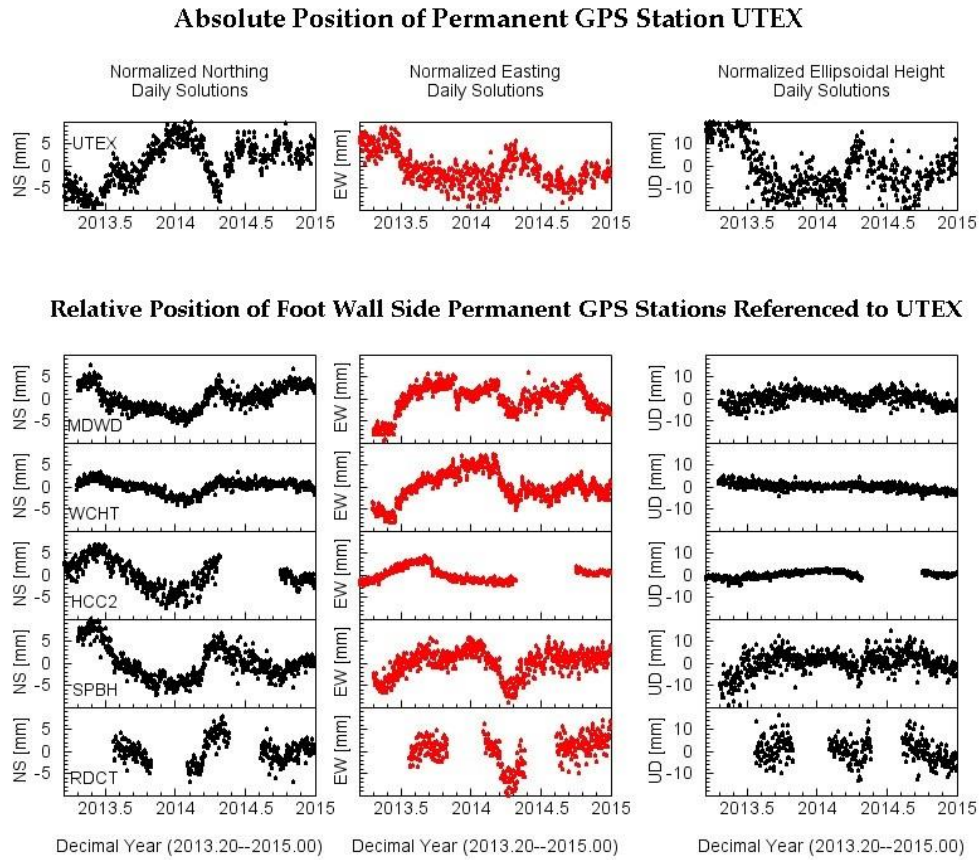

Figure 6.06: Time Series of Foot Wall Side GPS Stations Referenced to UTEX

Time series comparison of GPS stations relative to the foot wall side of the Long-Point Fault referenced to UTEX using the double-difference technique via Topcon Tools software. (North = positive NS, South = negative NS, East = positive EW, West = negative EW, rebound = positive UD, and subsidence = negative UD.)

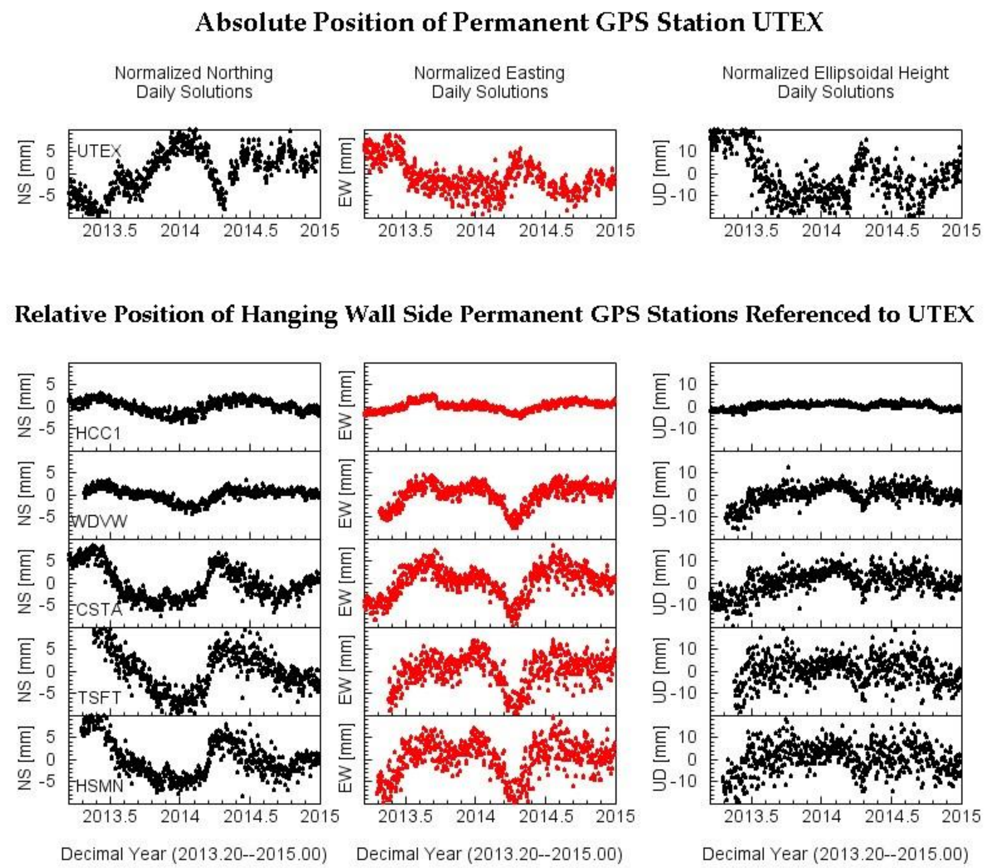

Figure 6.07: Time series of Hanging Wall Side GPS Stations Referenced to UTEX

Time series comparison of GPS stations relative to the hanging wall side of the Long-Point Fault referenced to UTEX using the double-difference technique via Topcon Tools software. (North = positive NS, South = negative NS, East = positive EW, West = negative EW, rebound = positive UD, and subsidence = negative UD.)

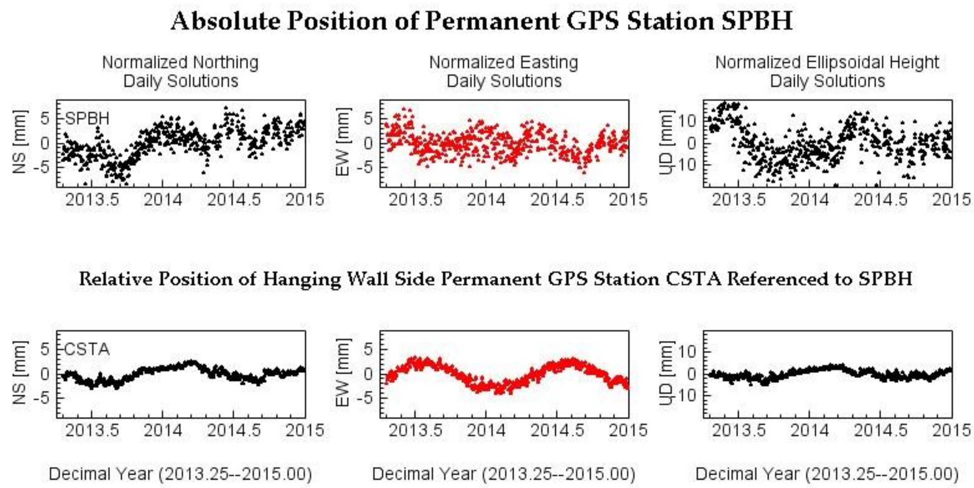

Figure 6.08: Time series of CSTA Referenced to SPBH

Time series comparison of GPS station CSTA (Hanging Wall Side) referenced to GPS Station SPBH (Foot Wall Side) using the double-difference technique via Topcon Tools software. (North = positive NS, South = negative NS, East = positive EW, West = negative EW, rebound = positive UD, and subsidence = negative UD.)

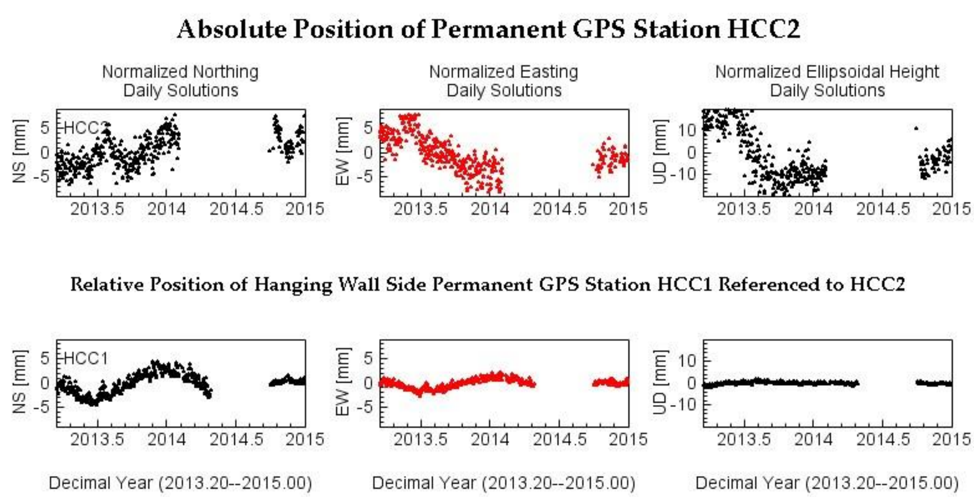

Figure 6.09: Time series of HCC1 Referenced to HCC2

Time series comparison of GPS station HCC1 (Hanging Wall Side) referenced to GPS Station HCC2 (Foot Wall Side) using the double-difference technique via Topcon Tools software. (North = positive NS, South = negative NS, East = positive EW, West = negative EW, rebound = positive UD, and subsidence = negative UD.)

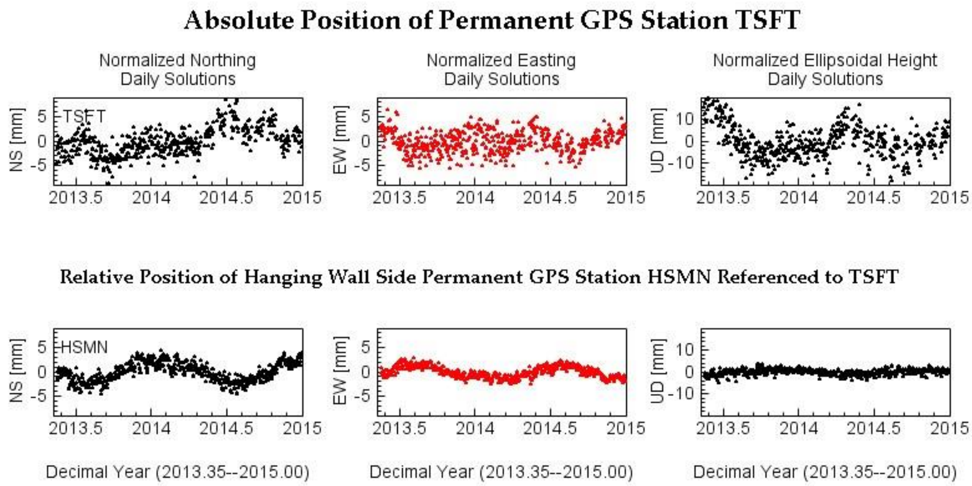

Figure 6.10: Time series of HSMN Referenced to TSFT

Time series comparison of GPS station HSMN (Hanging Wall Side) referenced to GPS Station TSFT (Hanging Wall Side) using the double difference technique via Topcon Tools software. (North = positive NS, South = negative NS, East = positive EW, West = negative EW, rebound = positive UD, and subsidence = negative UD.)

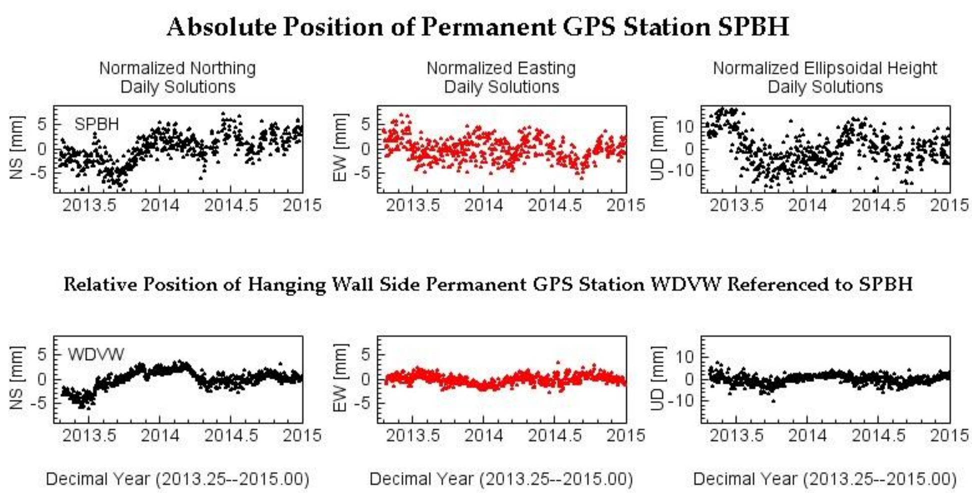

Figure 6.11: Time Series of WDVW Referenced to SPBH

Time series comparison of GPS station WDVW (Hanging Wall Side) referenced to GPS Station SPBH (Foot Wall Side) using the double-difference technique via Topcon Tools software. (North = positive NS, South = negative NS, East = positive EW, West = negative EW, rebound = positive UD, and subsidence = negative UD.)

Table 6.02 and 6.03 display directional velocities (millimeter per year) for all GPS stations referenced to UTEX as well as a horizontal velocity vectors (millimeter per year). Horizontal directional velocities for all GPS stations are stable, showing velocities of up to 1 mm/yr. Vertical directional velocities for most GPS stations are stable also, showing up to 1 mm/yr uplift; however, stations WCHT and RDCT show up to 2 mm/yr subsidence, while station CSTA shows 2 mm/yr uplift. All GPS stations have horizontal velocity vectors displaying up to 1 mm/yr velocity. Figures 6.12 and 6.13 display horizontal vector velocities and vertical vector velocities for all GPS stations referenced to UTEX, respectively. Again, no considerable relative movements were observed in all three directions for all GPS stations.

Station	Easting [mm/yr]	Easting Corr. [mm]	Northing [mm/yr]	Northing Corr. [mm]	Vertical [mm/yr]	Vertical Corr. [mm]
MDWD	0.67816	0.29216	0.82237	0.25	-0.1627	0.28559
WCHT	0.47484	0.30965	-0.102	0.13487	-1.2608	0.11407
HCC2	-0.034	0.18507	-1.6751	0.35143	0.71516	0.14433
HCC1	0.21234	0.056	-0.047	0.08193	0.35722	0.0682
WDVW	0.65761	0.24526	-0.4031	0.23796	1.96742	0.37764
SPBH	0.77354	0.27205	-1.3416	0.3498	1.64235	0.47897
CSTA	1.04137	0.2538	-1.3509	0.27234	2.57778	0.40067
RDCT	1.33524	0.80356	0.31127	0.64832	-2.8268	1.20984
TSFT	0.58967	0.39686	-1.2283	0.52113	-0.1021	0.72331
HSMN	0.82226	0.39841	-1.4748	0.40129	1.50525	0.73705

Table 6.02: Directional Velocities for All Stations Referenced to UTEX

Directional velocities for all stations as a result of the double-differencing technique.

Station	Horizontal Velocity Vector [mm/yr]	θ (degrees)
MDWD	1.065922155	39.51040537
WCHT	0.485662178	-77.88178035
HCC2	1.675432915	1.161905281
HCC1	0.217485217	-77.50766747
WDVW	0.771343269	-58.49047172
SPBH	1.548660847	-29.96634608
CSTA	1.705699254	-37.62758221
RDCT	1.371039716	76.87747158
TSFT	1.362463721	-25.64504187
HSMN	1.688520003	-29.14153154

Table 6.03: Horizontal Velocity Vectors and Direction for All Stations Referenced to UTEX

Horizontal velocity vectors and direction for all stations as a result of the double-differencing technique.

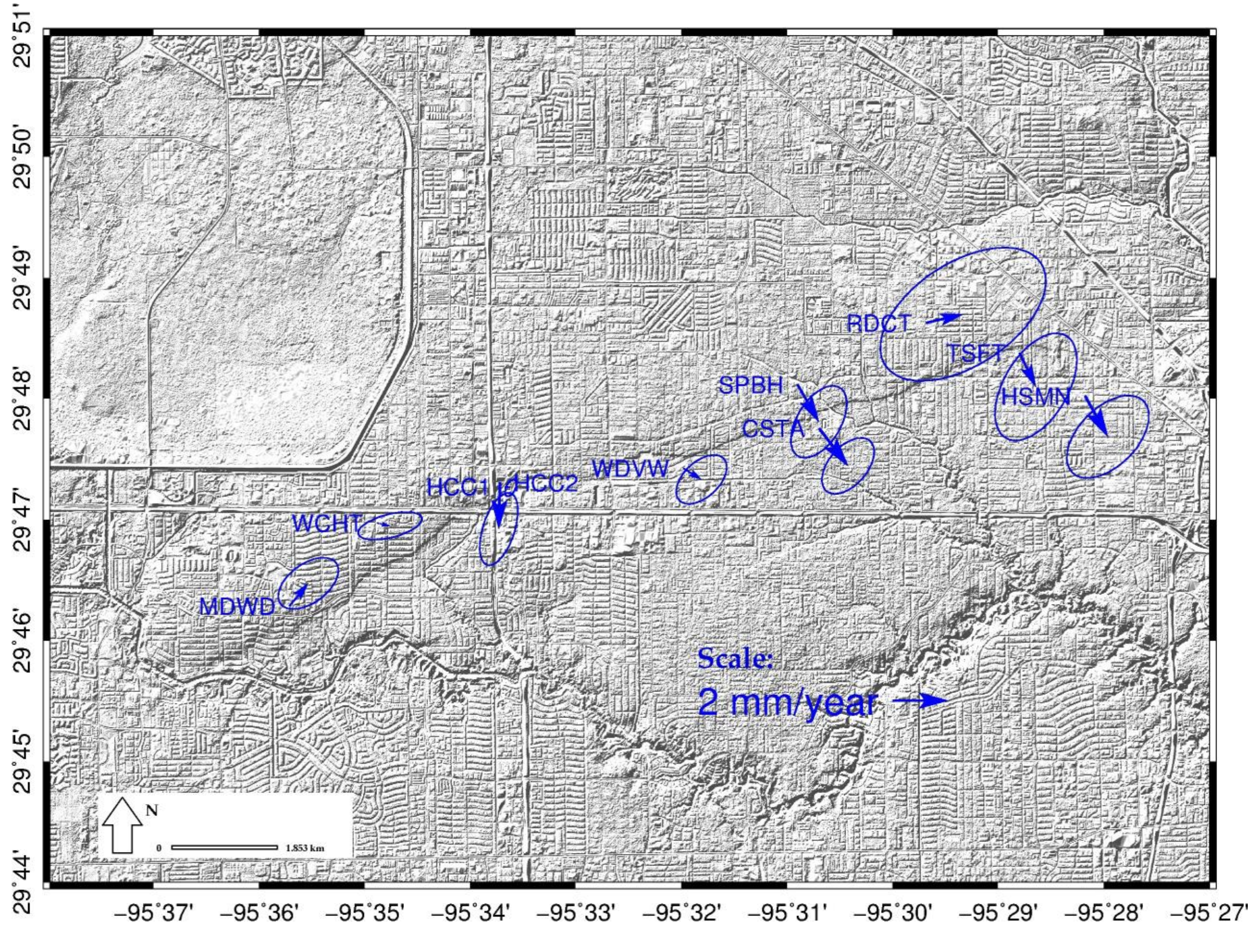

Figure 6.12: Horizontal Velocity Vectors for All Stations Referenced to UTEX

Horizontal velocity vectors for all stations as a result of the double-differencing technique.

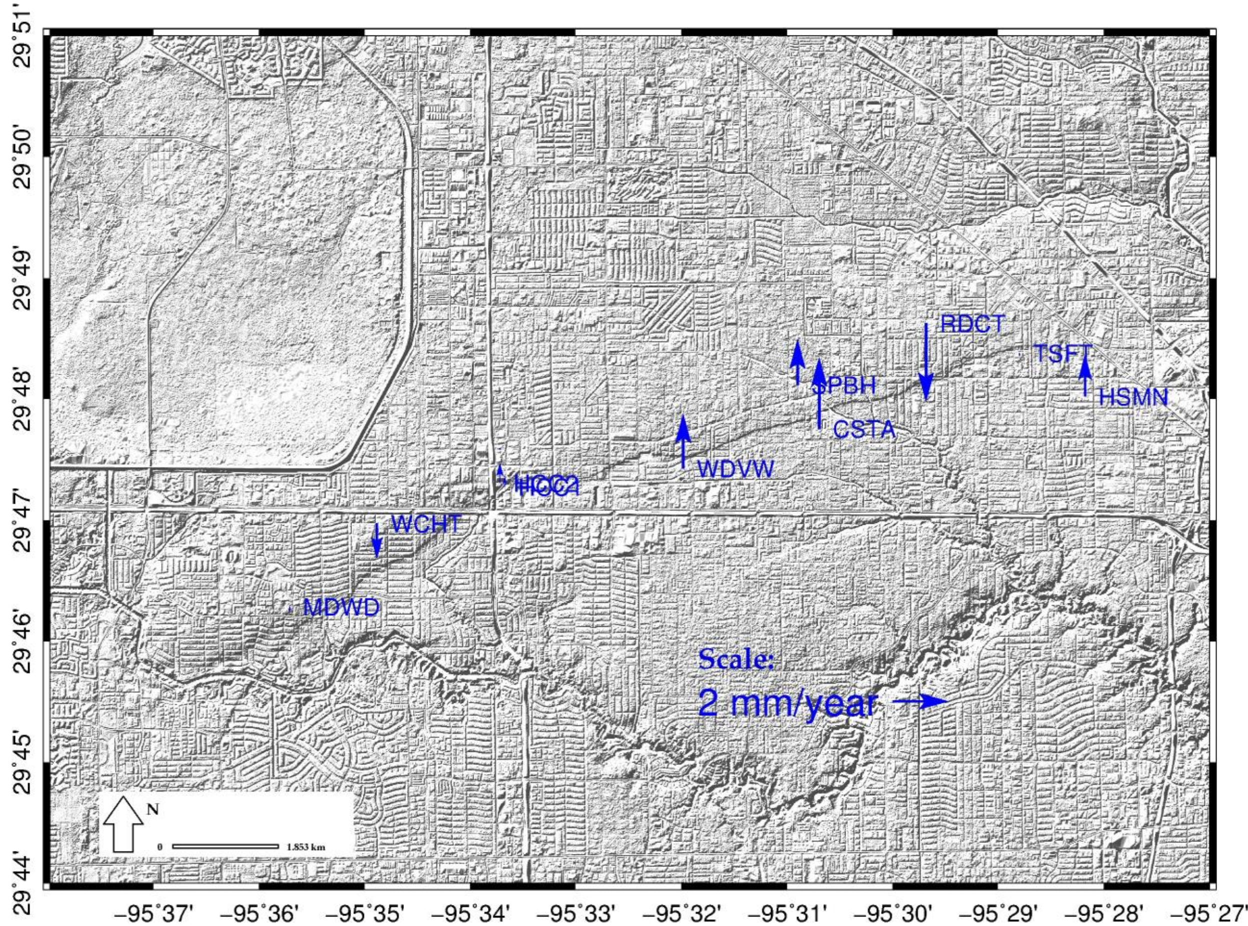

Figure 6.13: Vertical Velocity Vectors for All Stations Referenced to UTEX

Vertical velocity vectors for all stations as a result of the double-differencing technique.

In Figure 6.14, all GPS stations were processed utilizing GIPSY software. All GPS stations display high repeatability in all three directions. Although two stations, HCC2 and RDCT, are missing a considerable amount of data, all stations show seasonal variations in all three directions; however, seasonal variation in the vertical direction is strong. In the NS direction, absolute positions for all stations trend slightly to the North, but show stability with respect to the EW direction; moreover, all stations show subsidence.

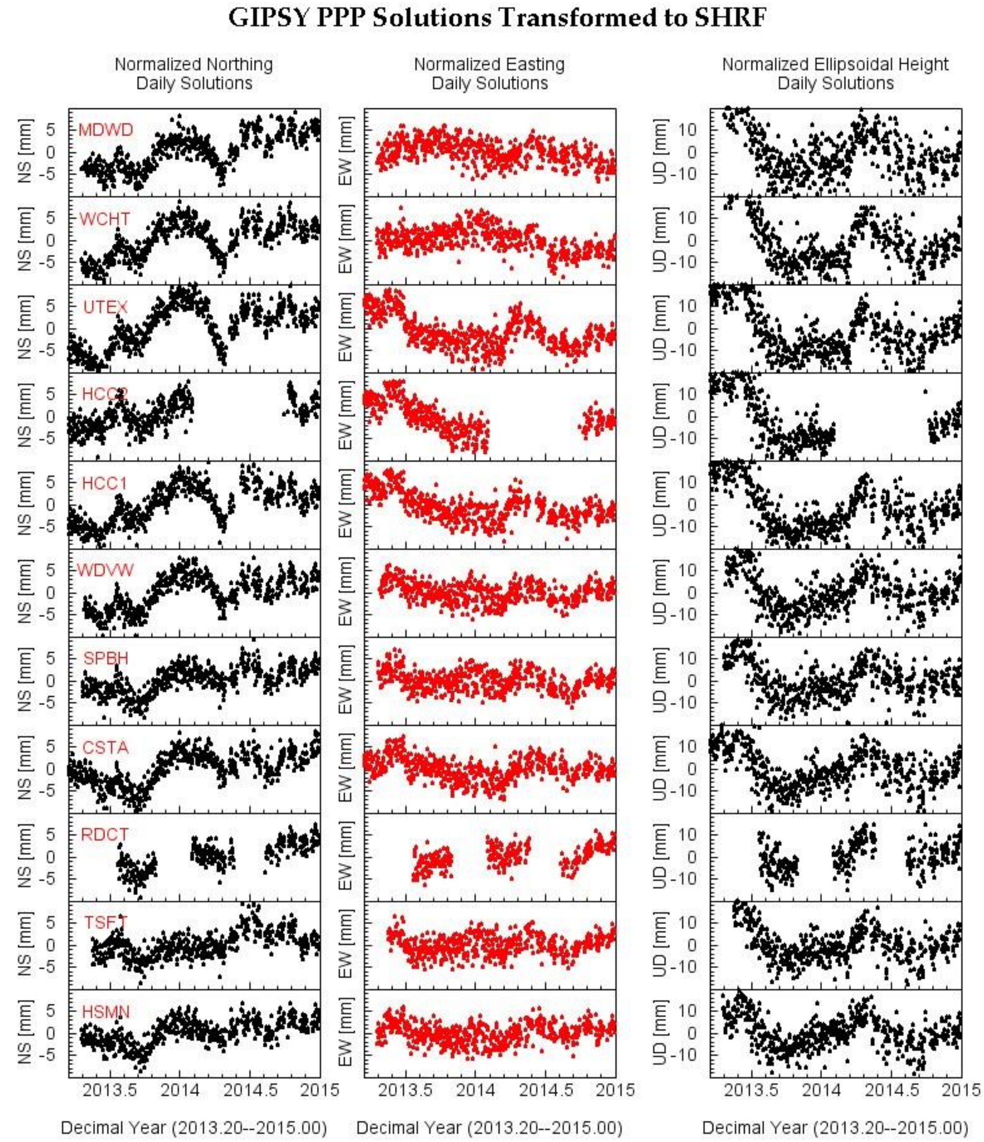

Figure 6.14: Time Series for All GPS Stations Referenced to SHRF

Time series comparison of all stations using the precise point positioning technique in the GIPSY software. (North = positive NS, South = negative NS, East = positive EW, West = negative EW, rebound = positive UD, and subsidence = negative UD.)

Table 6.04 and 6.05 display directional velocities (millimeters per year) for all stations with respect to SHRF as well as a horizontal velocity vector (millimeters per year) with direction. All stations have easting directional velocities displaying up to 1 mm/yr; however, northing directional velocities range from 1–4 mm/yr. Horizontal directional and vertical velocities relative to HCC2 and RDCT have not been taken into consideration. Compared to stations within their respective areas, HCC2 and RDCT horizontal directional velocities are significantly higher. This is most likely attributable to the significant amount of data missing from their respective datasets, thus skewing velocities in all directions. Vertical directional velocities for all stations (excluding HCC2 and RDCT) range from 1–7 mm/yr subsidence. Horizontal velocity vectors display 1–4 mm/yr velocity. Figures 6.15 and 6.16 display horizontal vector velocities and vertical vector velocities for all GPS stations referenced to SHRF, respectively. Again, tabulated velocities confirm slight trending to the North in the NS direction, stability in the EW direction, and subsidence for all stations.

Station	Easting [mm/yr]	Easting Corr. [mm]	Northing [mm/yr]	Northing Corr. [mm]	Vertical [mm/yr]	Vertical Corr. [mm]
MDWD	-1.5316	0.28102	4.12529	0.33966	-5.3089	1.30896
WCHT	-1.4645	0.29103	3.44309	0.38562	-7.0938	1.34575
UTEX	-1.2522	0.13236	1.27825	0.1795	-2.1818	0.43142
HCC2	-3.0821	0.53822	3.04618	0.44413	-10.25	1.88381
HCC1	-1.8004	0.19485	1.93015	0.26864	-5.1629	0.73344
WDVW	-0.6501	0.27023	3.32062	0.39527	-1.5318	1.08285
SPBH	-0.6495	0.27163	2.61778	0.29854	-2.1592	0.979
CSTA	-0.7278	0.24016	2.41381	0.29907	-3.3088	0.82499
RDCT	3.06188	0.6169	6.27089	0.6255	5.19158	1.85437
TSFT	0.30385	0.3123	2.39179	0.34572	-2.2649	1.04005
HSMN	0.10348	0.2745	2.26598	0.28276	-1.9302	0.87164

Table 6.04: Directional Velocities for All Stations Referenced to SHRF

Directional velocities for all stations as a result of the precise point positioning technique.

Stations	Horizontal Velocity Vector [mm/yr]	θ (degrees)
MDWD	4.40043813	-20.36857768
WCHT	3.741623514	-23.04285578
UTEX	1.789356573	-44.4091437
HCC2	4.33343033	-45.33594889
HCC1	2.639494794	-43.00814824
WDVW	3.383658087	-11.07701198
SPBH	2.697140983	-13.93360984
CSTA	2.521151151	-16.77945507
RDCT	6.978478239	26.02480613
TSFT	2.411011366	7.239925215
HSMN	2.268345655	2.614798017

Table 6.05: Horizontal Velocity Vectors and Direction for All Stations Referenced to SHRF

Horizontal velocity vectors for all stations as a result of the precise point positioning technique.

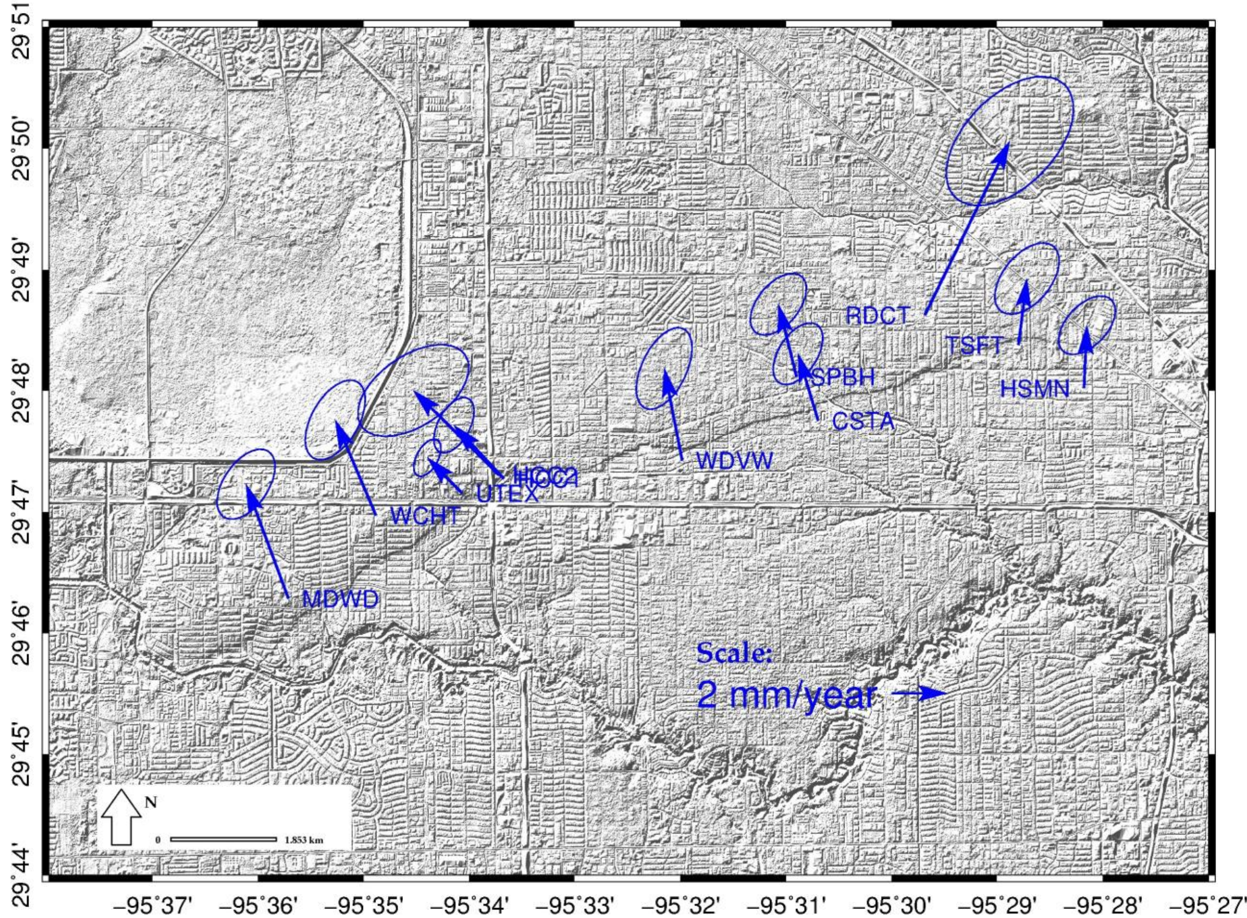

Figure 6.15: Horizontal Velocity Vectors for All Stations Referenced to SHRF

Horizontal velocity vectors for all stations as a result of the precise point positioning technique.

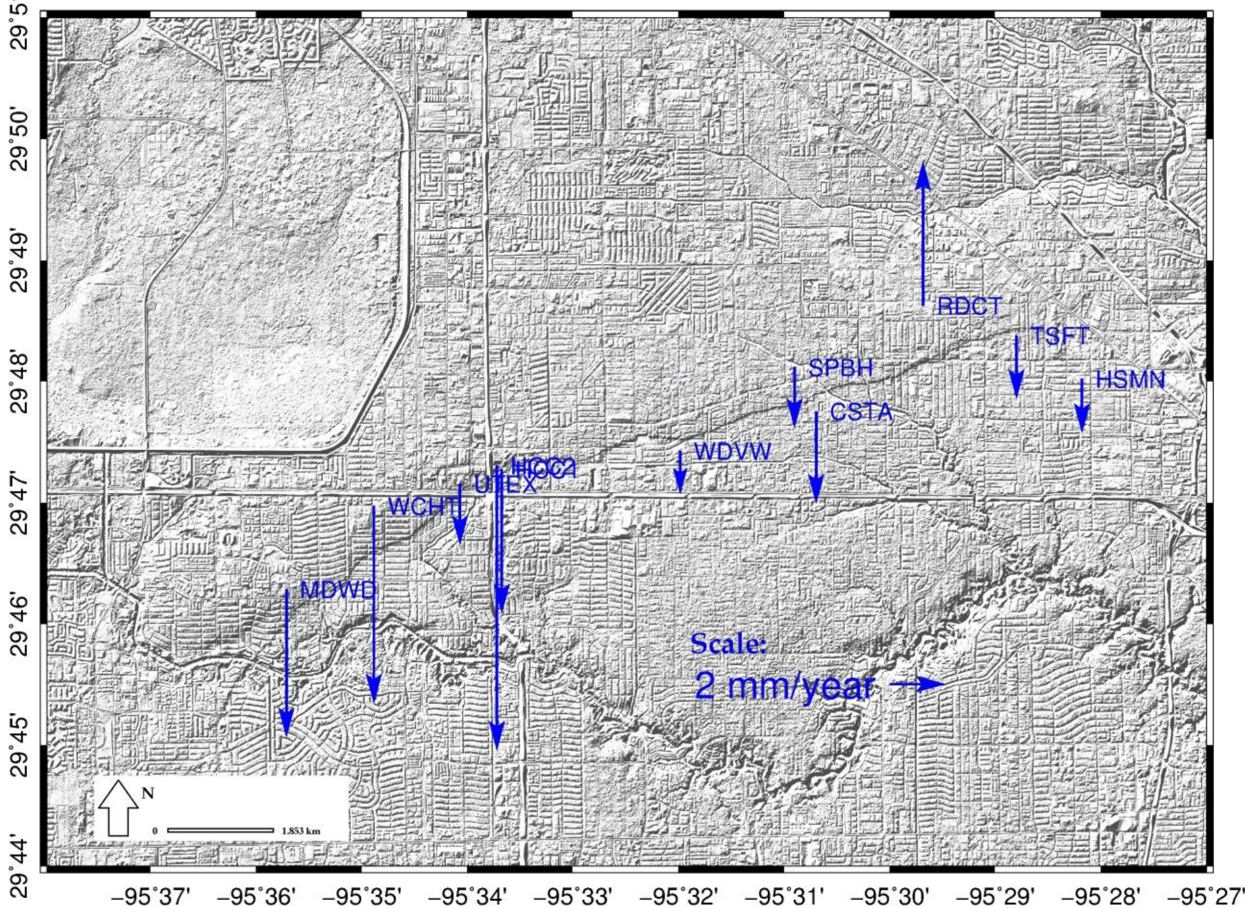

Figure 6.16: Vertical Velocity Vectors for All Stations Referenced to SHRF

Vertical velocity vectors for all stations as a result of the precise point positioning technique.

In Figure 6.17, all GPS stations were processed utilizing NGS OPUS Static processing. All GPS stations display lower repeatability, compared to GIPSY processing, in all three directions. Similarly, although two stations, HCC2 and RDCT, are missing a considerable amount of data, all stations show strong seasonal signals in all three directions. In the NS direction, relative positions for all stations trend slightly to the North, but exhibit stability with respect to the EW direction; moreover, all stations show subsidence.

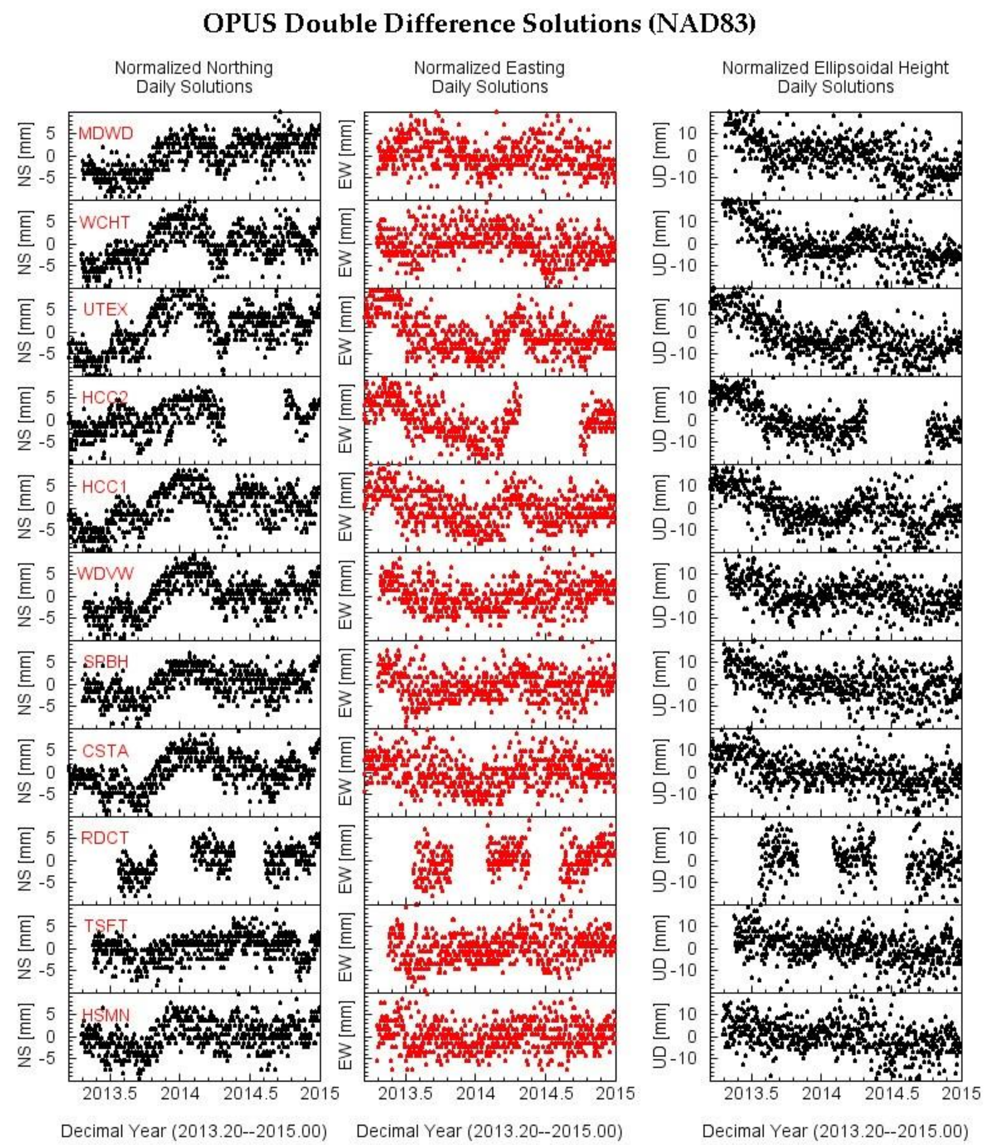

Figure 6.17: Time Series for All GPS Stations Referenced to NAD83

Time series comparison of all stations using the double-difference technique utilizing NGS OPUS. (North = positive NS, South = negative NS, East = positive EW, West = negative EW, rebound = positive UD, and subsidence = negative UD.)

Table 6.06 and 6.07 display directional velocities (millimeters per year) for all stations referenced to NAD83 as well as a horizontal velocity vector (millimeters per year) with direction. All stations have easting directional velocities exhibiting stability; however, northing directional velocities range 1–3 mm/yr. Analogous to GIPSY processing, horizontal directional and vertical velocities relative to HCC2 and RDCT have not been taken into consideration. Vertical directional velocities for all stations (excluding HCC2 and RDCT) range from 3–7 mm/yr subsidence. Horizontal velocity vectors exhibit 1–3 mm/yr velocity. Again, tabulated velocities confirm slight trending to the North in the NS direction, stability in the EW direction, and subsidence for all stations.

Stations	Easting [mm/yr]	Northing [mm/yr]	Vertical [mm/yr]
MDWD	-0.8766592501	3.0271280429	-6.8666630519
WCHT	-0.9290506785	1.9876753628	-7.1311045185
UTEX	-0.8108815338	1.1611560011	-3.1687544243
HCC2	-1.3419346057	1.6442433422	-6.0384175472
HCC1	-0.7892727910	1.0960766093	-4.5042355953
WDVW	-0.1365241151	2.0376052456	-3.4342065880
SPBH	-0.0329704903	1.4321898509	-3.9785535215
CSTA	-0.2044985873	1.2535863156	-3.7199622780
RDCT	1.4690000420	2.1276067286	-2.4223024578
TSFT	0.8345064126	0.8425890508	-3.1827463172
HSMN	0.1333394898	1.2484793674	-3.1567050571

Table 6.06: Directional Velocities for All Stations Referenced to NAD83

Directional velocities for all stations as a result of the double-difference technique.

Stations	Horizontal Velocity Vector [mm/yr]	θ (degrees)
MDWD	3.1515132284	-16.1510681962
WCHT	2.1940803337	-25.0516520034
UTEX	1.4162669666	-34.9281326128
HCC2	2.1223394296	-39.2192985693
HCC1	1.3506796334	-35.7572482703
WDVW	2.0421738347	-3.8332162501
SPBH	1.4325693080	-1.3187751120
CSTA	1.2701568103	-9.2650972461
RDCT	2.5854731704	34.6230290694
TSFT	1.1858993470	44.7238693442
HSMN	1.2555796073	6.0961674562

Table 6.07: Horizontal Velocity Vectors and Direction for All Stations Referenced to NAD83

Horizontal velocity vectors for all stations as a result of the double-difference technique.

Figures 6.18 and 6.19 present time series for twenty-six benchmarks installed on the foot wall and hanging wall sides of the Long-Point Fault. Excluding two benchmarks, JS03 and JS25, all benchmarks have two survey measurements, conducted December, 2014 and January, 2015. Normalized solutions (based on fifteen- to twenty-minute surveys) are displayed on a centimeter scale. Two months of campaign survey measurements are not long enough to identify any coherent fault motions; however, observations between the first and last survey measurements reveal certain differences on the order of subcentimeters.

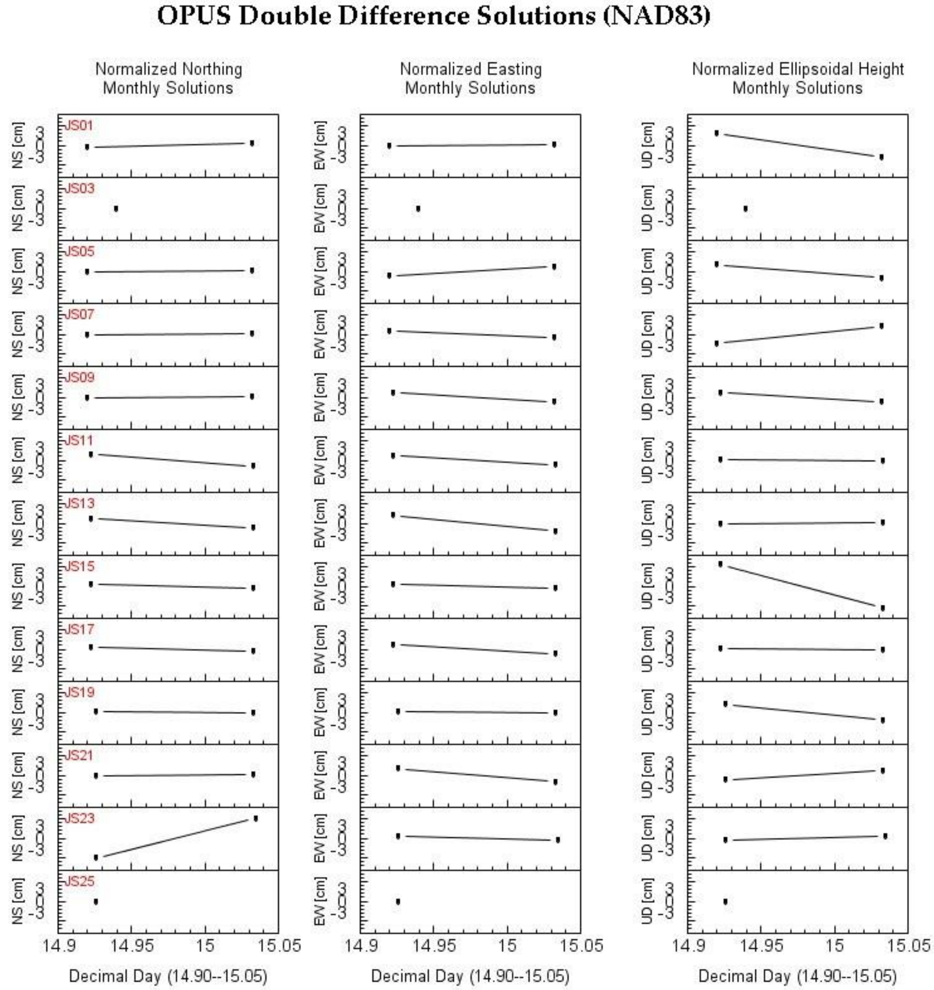

Figure 6.18: Time Series of Foot Wall Side Benchmarks Relative to the Long-Point Fault

Time series comparison of odd numbered benchmarks (thirteen) on the footwall side of Long-Point Fault using the double-difference technique utilizing NGS OPUS. (North = positive NS, South = negative NS, East = positive EW, West = negative EW, rebound = positive UD, and subsidence = negative UD.)

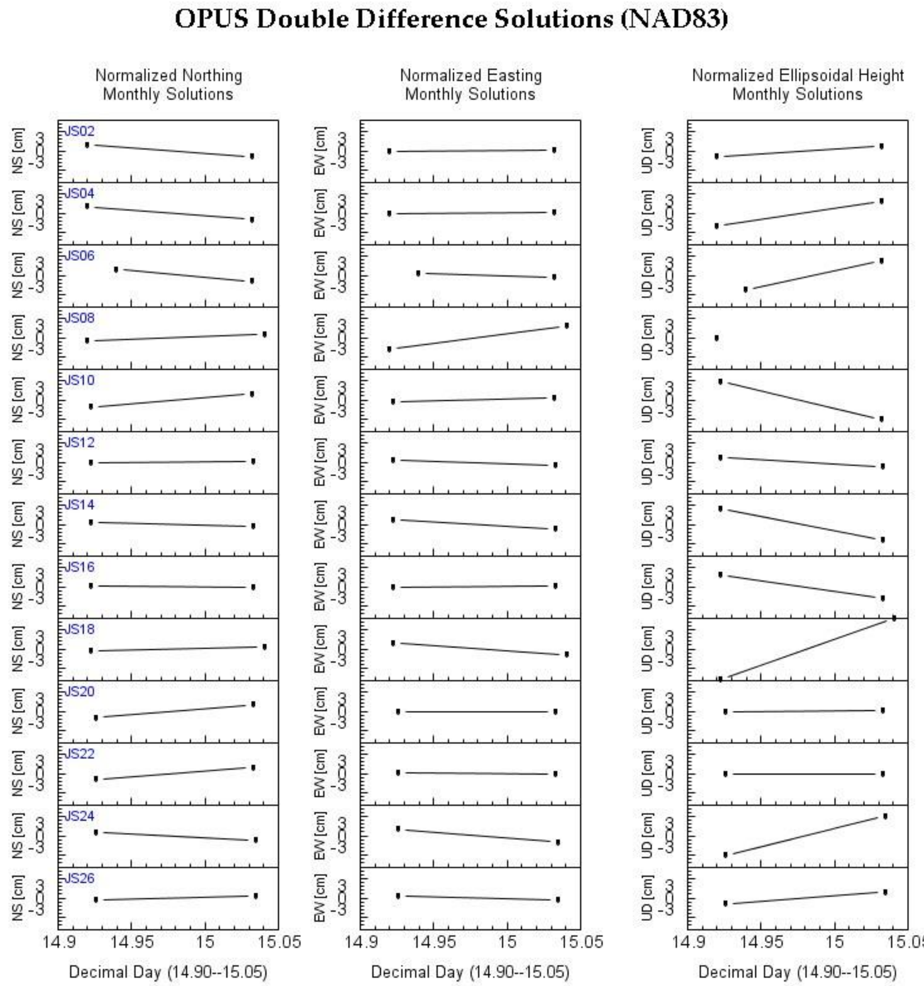

Figure 6.19: Time Series of Hanging Wall Side Benchmarks Relative to the Long-Point Fault

Time series comparison of even numbered benchmarks (thirteen) on the hanging wall side of Long-Point Fault using the double-difference technique utilizing NGS OPUS. (North = positive NS, South = negative NS, East = positive EW, West = negative EW, rebound = positive UD, and subsidence = negative UD.)

6.3 Fault Activity Comparison

Utilizing long-term GPS observations relative to the Hayward and San Andreas Faults (California), a fault activity (kinetics) comparison to the Long-Point Fault will support the significance of horizontal velocity and vertical directional velocities derived from the processed GPS daily solutions (2012–2014) of this study. Processed GPS daily solutions (NA14 and IGS08) through the Nevada Geodetic Laboratory are available to the public for download (www.geodesy.unv.edu). Because of the vicinity of station pairs SRB1 & P224 and P193 & MCCM to the Hayward and San Andreas Faults (respectively), these stations were chosen as close comparisons (e.g. distances between stations and distance to fault) in relation to the Long-Point Fault, as shown in Figure 6.20.

Hayward & San Andreas Fault

Figures 6.21 and 6.22 display GPS time series from stations relative to the Hayward and the San Andreas Fault, respectively. The figures display normalized daily solutions representative of the NS, EW, and UD directions. While daily solutions for the four GPS stations span a period of approximately four to eight years, all four stations show similarity in trends. In the NS direction, relative positions for all stations trend to the North, but show stability with respect to the EW direction; moreover, all stations show uplift.

Tables 6.08 and 6.09 display directional velocities (centimeters per year) for GPS stations SRB1 and P224 processed by the Nevada Geodetic Laboratory (NA12) as well as horizontal velocity vectors (centimeters per year). Northing directional velocities range from 1–2 cm/yr; in contrast, both GPS stations have easting directional velocities exhibiting stability. Vertical directional velocities for both GPS stations range from 1–2 cm/yr uplift, and horizontal velocity vectors display 1–3 cm/yr velocity. Tabulated velocities confirm trending to the North in the NS direction, stability in the EW direction, and uplift for both SRB1 and P224 GPS stations.

Tables 6.10 and 6.11 display directional velocities (centimeters per year) for GPS stations P193 and MCCM processed by the Nevada Geodetic Laboratory (NA12) as well as horizontal velocity vectors (centimeters per year) with direction. Northing directional velocities range from 3–9 cm/yr; however, both GPS stations have easting directional velocities ranging up to 1 cm/yr. Vertical directional velocities for both GPS stations range from 3–6 cm/yr uplift, and horizontal velocity vectors display 4–9 cm/yr velocity. Tabulated velocities confirm trending to the North in the NS direction, stability in the EW direction, and uplift for both P193 and MCCM GPS stations.

Comparison

Horizontal vector velocities for the Hayward and San Andreas Faults are greater than the Long-Point Fault. At 1–3 cm/yr (Hayward) and 4–9 cm/yr (San Andreas), as shown in Figures 6.23 and 6.25, respectively, the horizontal vector velocities surpass the Long-Point Fault horizontal vector velocity range of 1–3 mm/yr. Similarly, vertical directional velocities for the Hayward and San Andreas Faults are larger than the Long-Point Fault. At 1–2 cm/yr (Hayward Fault) and 3–6 cm/yr (San Andreas Fault), the vertical directional velocities exceed the Long-Point Fault vertical directional velocity range of 1–7 mm/yr. Comparatively, the horizontal vector and vertical directional velocities of the Long-Point Fault are much slower than those of the Hayward and San Andreas Faults.

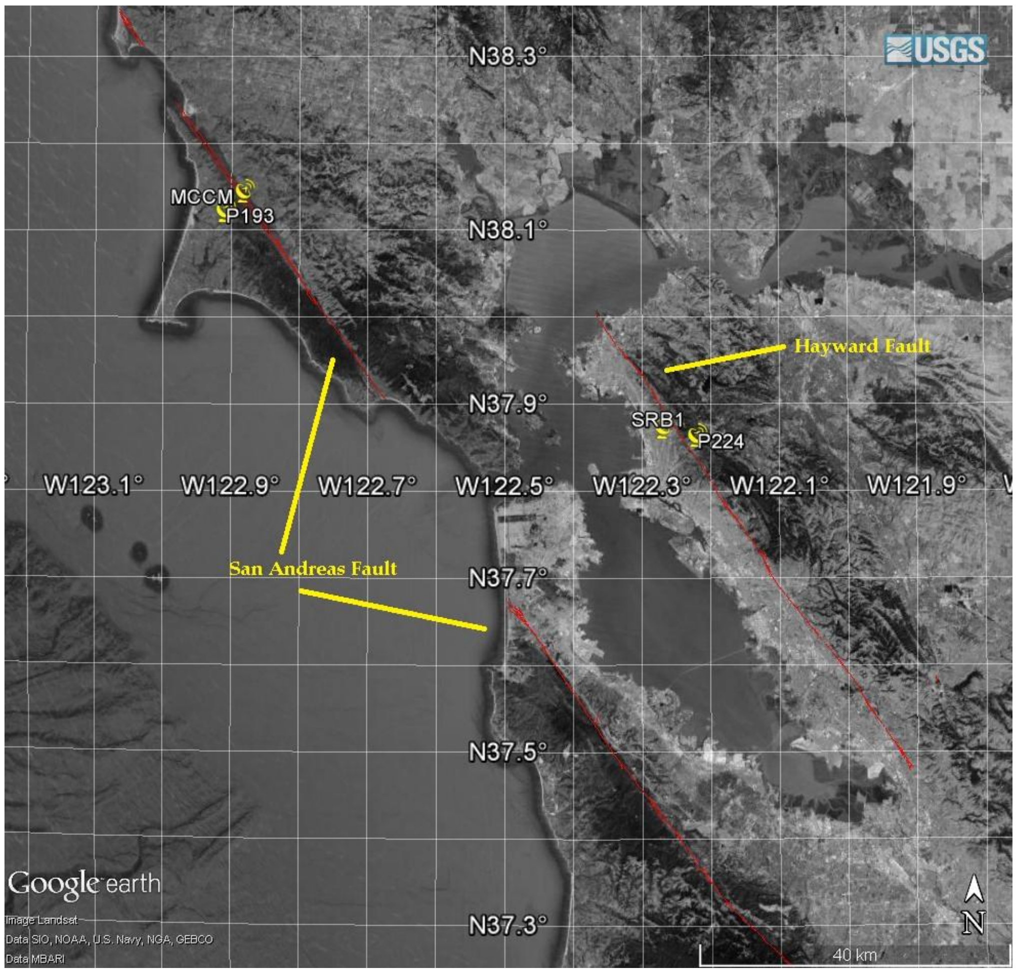

Figure 6.20: Hayward and San Andreas Fault (California, U.S.A.)
Google Earth mapping of both San Andreas and Hayward Fault interfaced with permanent GPS stations MCCM, P193, SRB1, and P224.

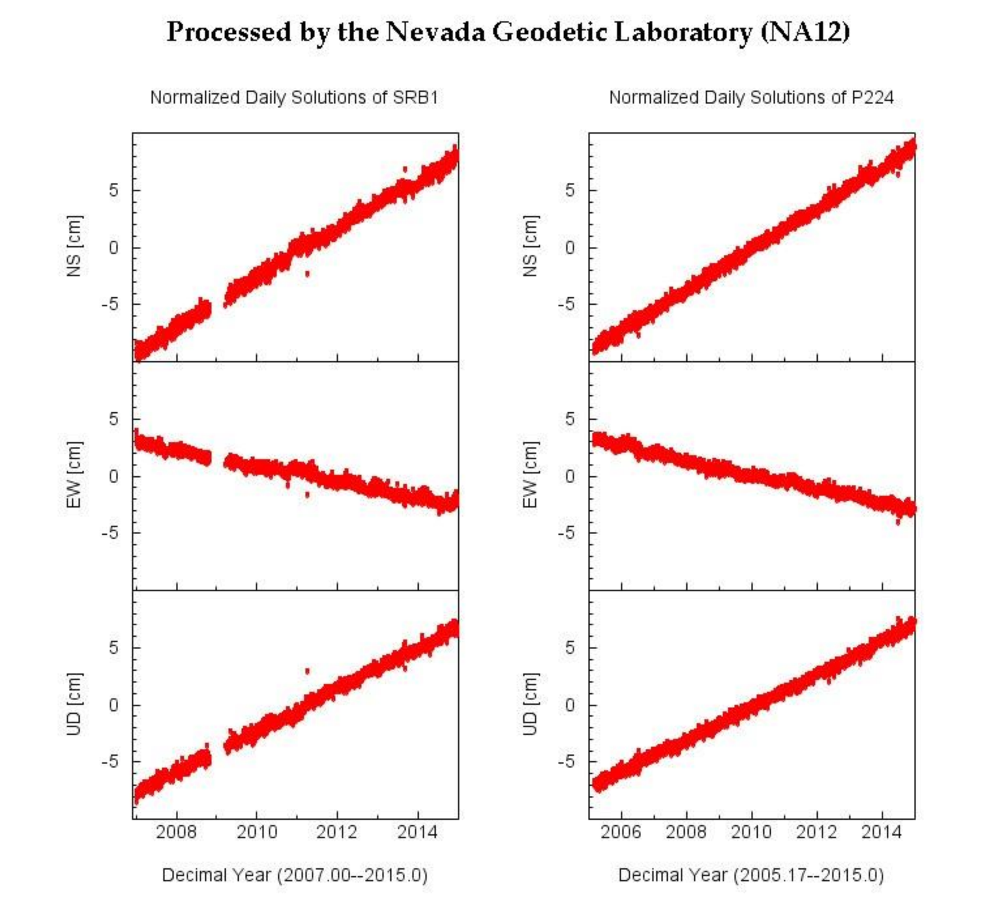

Figure 6.21: Time Series for Stations SRB1 and P224 (Hayward Fault)

Time Series comparison for stations SRB1 and P224 in the vicinity of the Hayward Fault. (North = positive NS, South = negative NS, East = positive EW, West = negative EW, rebound = positive UD, and subsidence = negative UD.)

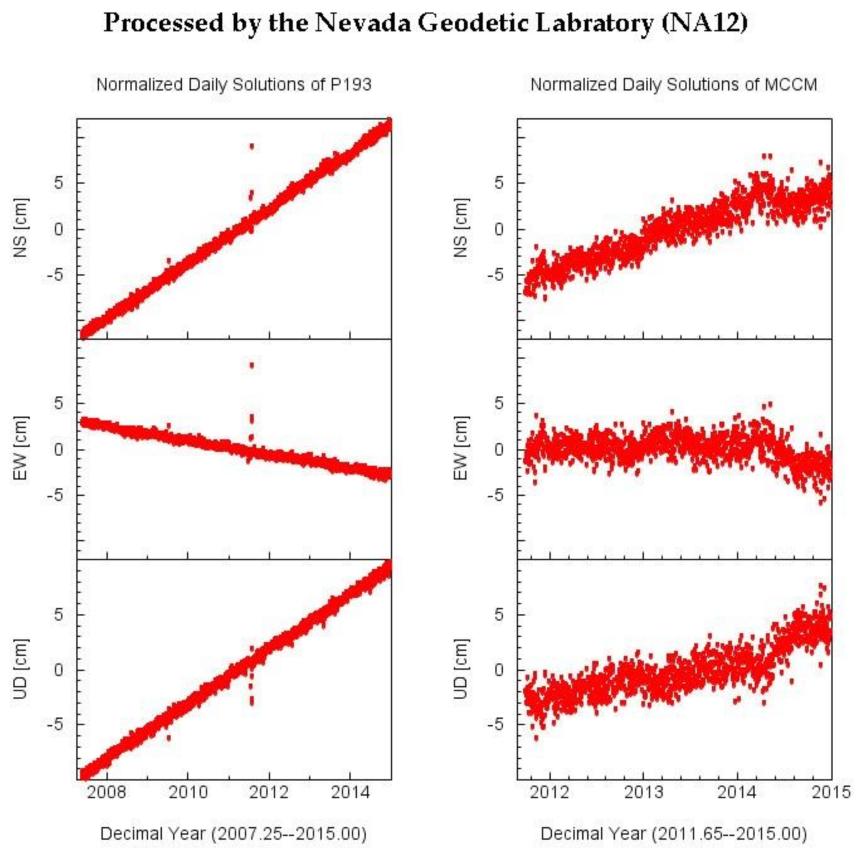

Figure 6.22: Time Series for Stations P193 and MCCM (San Andreas Fault)

Time Series for stations P193 and MCCM in the vicinity of the San Andreas Fault. (North = positive NS, South = negative NS, East = positive EW, West = negative EW, rebound = positive UD, and subsidence = negative UD.)

Station	Northing [cm/yr]	Easting [cm/yr]	Vertical [cm/yr]
SRB1	2.8719864532	-0.9268772086	2.4316804012
P224	1.8015571938	-0.6290544418	1.4460758536

Table 6.08: Directional Velocities for Stations SRB1 and P224

Directional velocities for stations processed with respect to NAD83.

Station	Horizontal Velocity Vector [cm/yr]	θ (degrees)
SRB1	3.017848165	-17.8864656
P224	1.908223732	-19.2478033

Table 6.09: Horizontal Velocity Vectors and Direction for Stations SRB1 and P224

Horizontal velocity vectors processed with respect to NAD83.

Station	Northing [cm/yr]	Easting [cm/yr]	Vertical [cm/yr]
P193	3.9208617172	-0.9860139383	3.2508614140
MCCM	9.2394439798	-1.4145668566	6.0343784221

Table 6.10: Directional Velocities for Stations P193 and MCCM

Directional velocities for stations processed with respect to NAD83.

Station	Horizontal Velocity Vector [cm/yr]	θ (degrees)
P193	4.042942009	-14.1159653
MCCM	9.347102463	-8.70444297

Table 6.11: Horizontal Velocity Vectors and Direction for Stations P193 and MCCM

Horizontal velocity vectors processed with respect to NAD83.

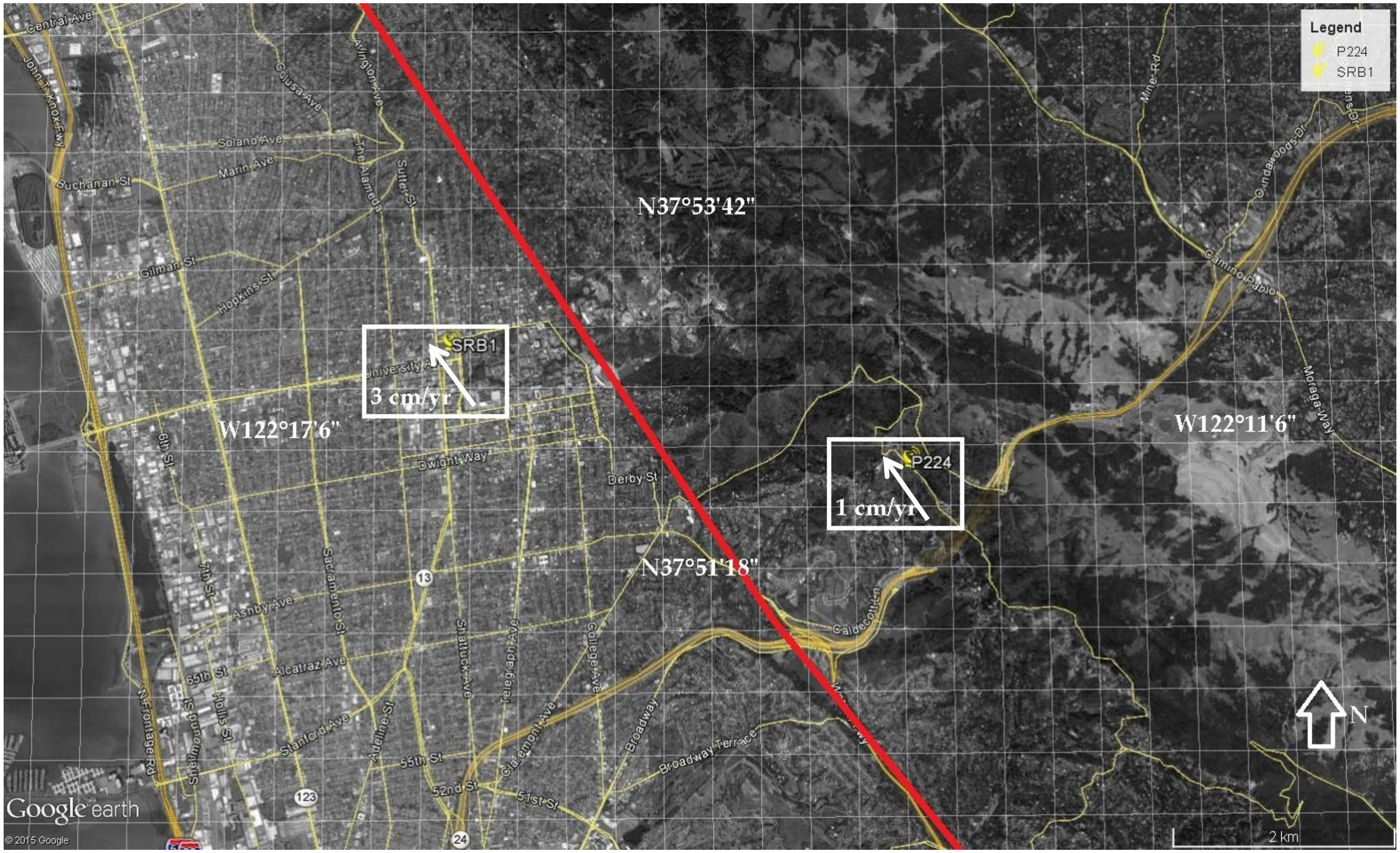

Figure 6.23: Hayward Fault Horizontal Vector Velocities
Stations SRB1 and P224 along the Hayward Fault displaying 3 cm/yr and 1 cm/yr velocity, respectively.

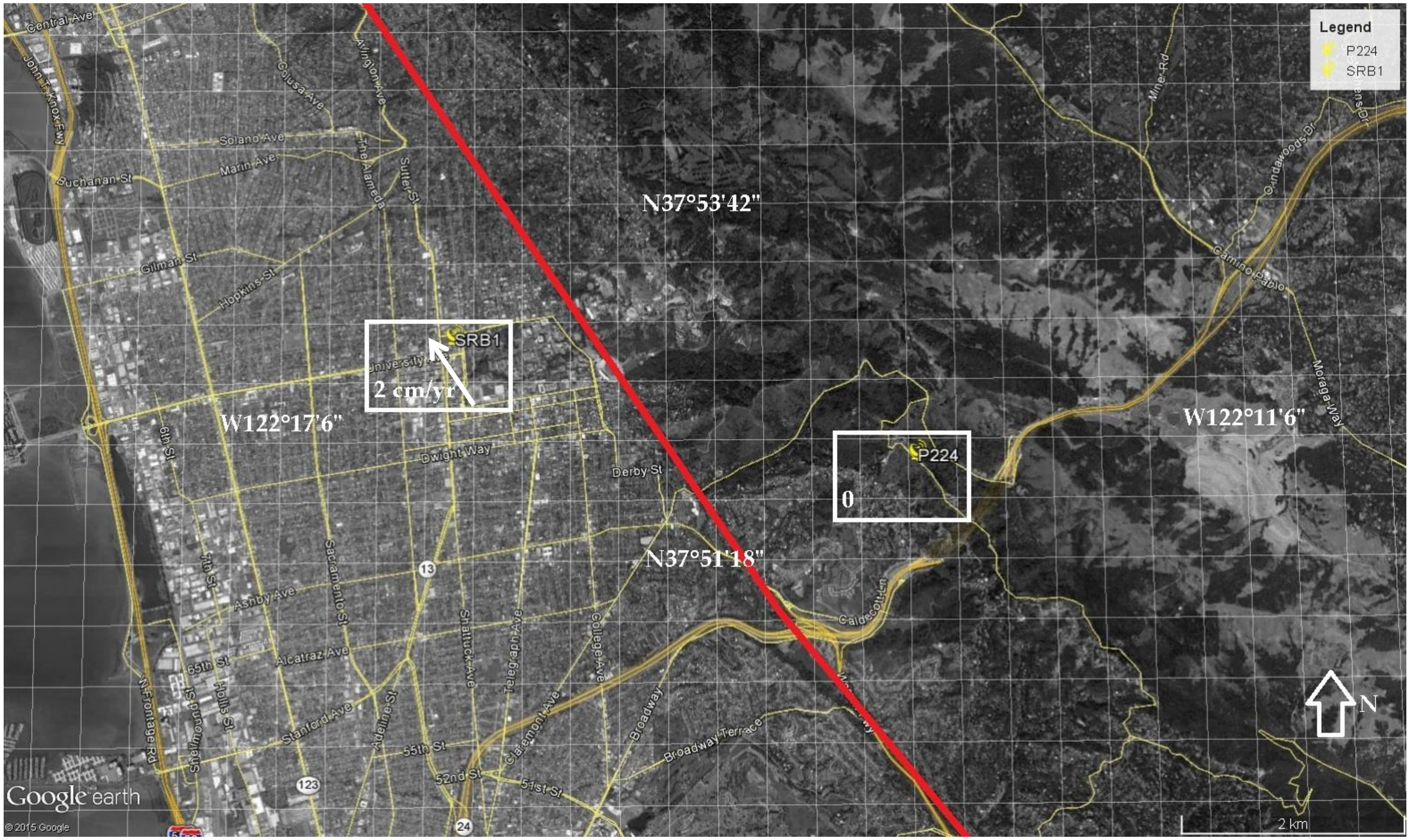

Figure 6.24: Resultant Horizontal Vector Velocity of GPS Station SRB1 with Respect to Stationary GPS Station P224
By making GPS station P224 the reference station, GPS station SRB1 displays 2 cm/yr velocity (right-lateral).

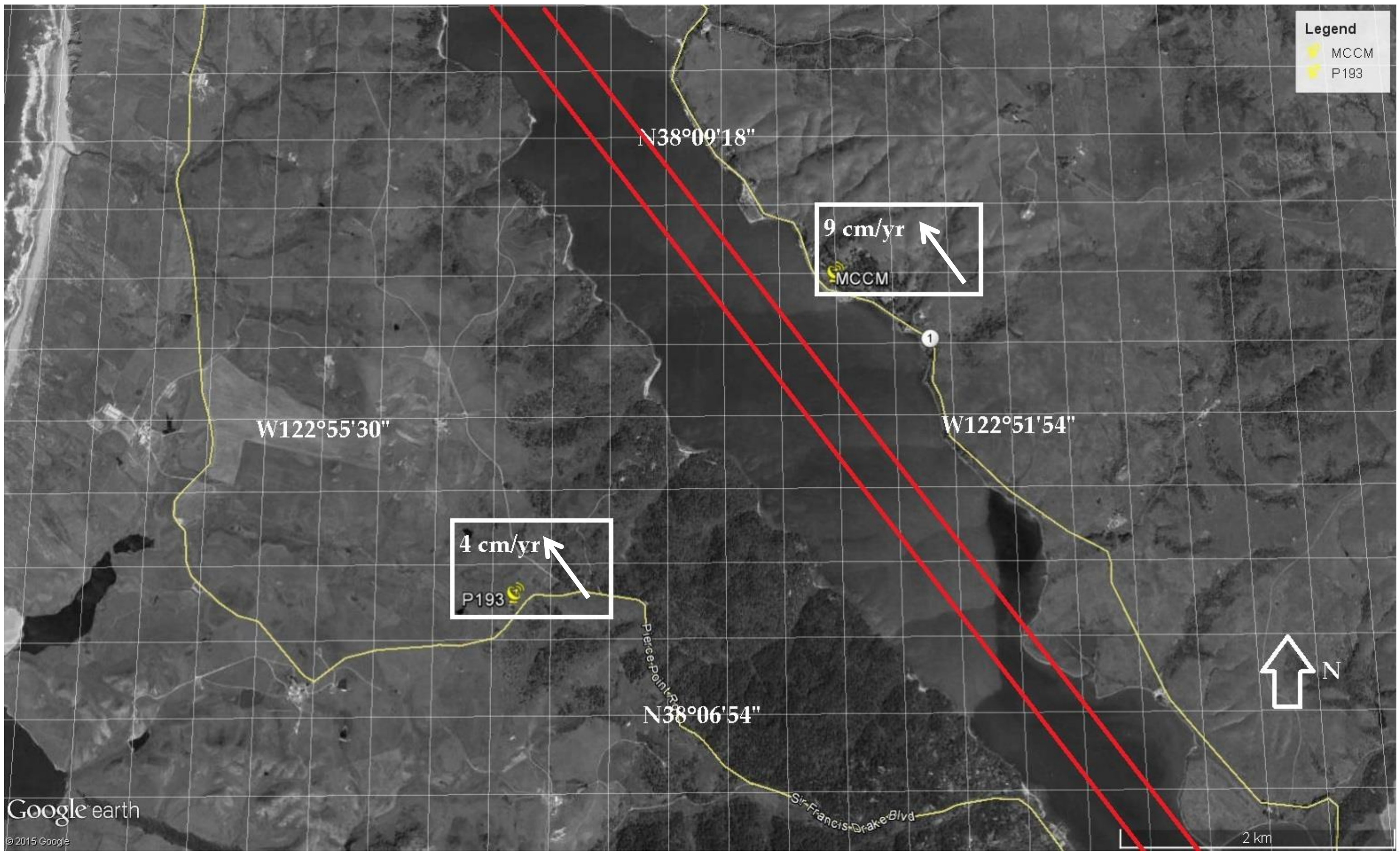

Figure 6.25: San Andreas Fault Horizontal Vector Velocities

Stations P193 and MCCM along the San Andreas Fault displaying 4 cm/yr and 9 cm/yr velocity, respectively.

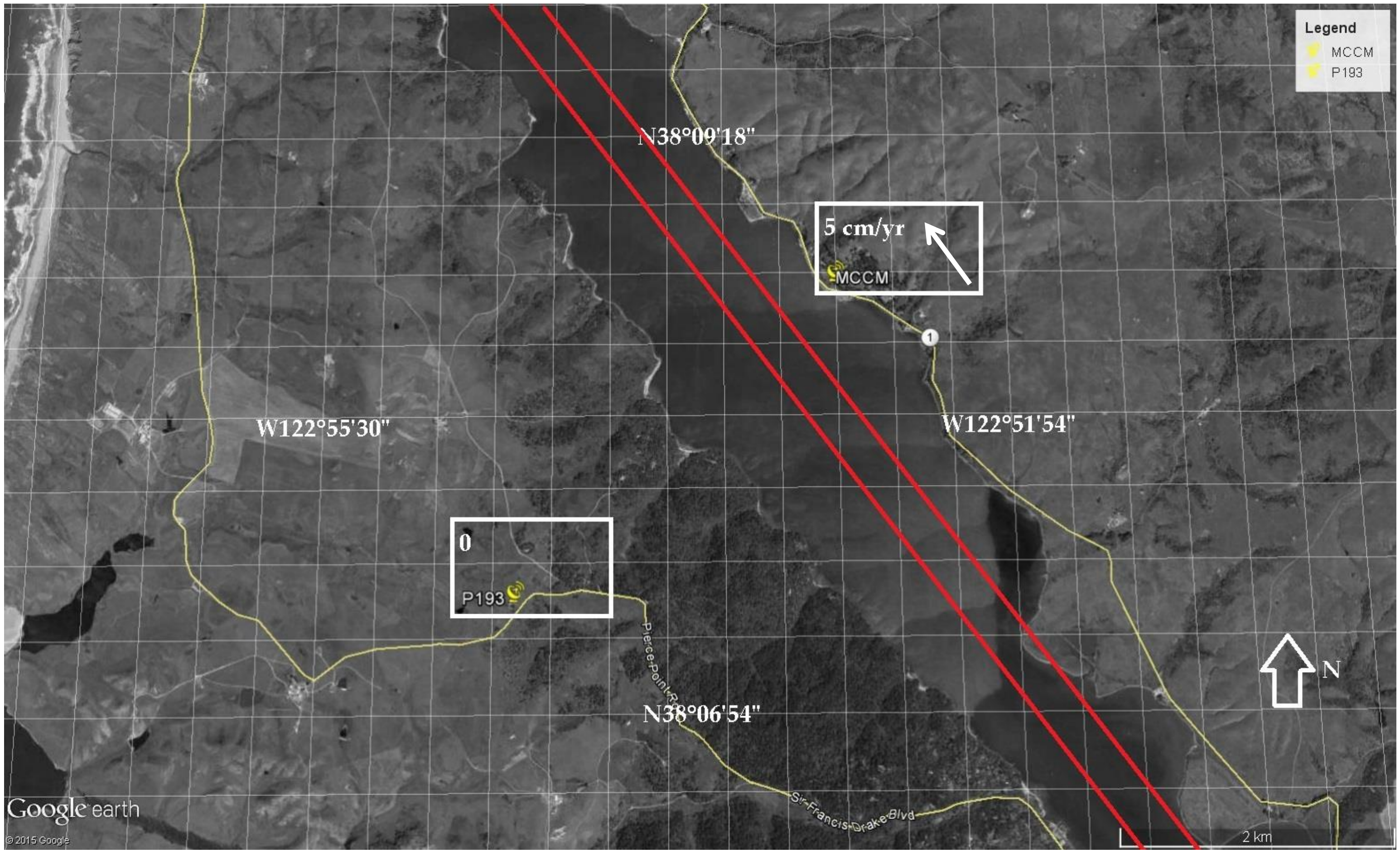

Figure 6.26: Resultant Horizontal Vector Velocity of GPS Station MCCM with Respect to Stationary GPS Station P193
By making GPS station P193 the reference station, GPS station MCCM displays 5 cm/yr velocity (left-lateral).

6.4 Current Activity of the Long-Point Fault

Double-difference and PPP processing of daily solutions from eleven continuously monitoring GPS stations (2012–2014) installed along the footwall and hanging wall side of the Long-Point Fault revealed no considerable, steady horizontal movements; however, vertical directional velocities range from 1–7 mm/yr subsidence. This subsidence rate agrees with reported subsidence rates of 5–8 mm/yr (2005–2012) within the Addicks area (Kearns et al., 2015). Figure 6.27 displays average subsidence rates within the Houston area (2005–2012).

Groundwater

Groundwater data was obtained from water wells (Figure 6.28 and 6.30) in the western Houston area, and within the vicinity of the Long-Point Fault area, through the USGS Active Groundwater Watch website. Water wells measured the yearly and daily depth to groundwater level for the Chicot and Evangeline aquifer system. At the end of 2014, the groundwater levels in the Chicot and Evangeline aquifers in the Long-Point Fault area were 50–53 meters and 69–106 meters below the ground surface, respectively. The Chicot and Evangeline aquifer system displays stability within the past five years, as shown in Figure 6.29; however, prior to 2010, variance between station measurements is considerable. Daily depth to groundwater level for the Chicot and Evangeline aquifer system shows correlation between aquifer recharge, and withdrawal, and vertical seasonal variation exhibited by all installed GPS stations along the Long-Point Fault. Figures 6.31 and 6.32 display depth to groundwater level for the Chicot and Evangeline aquifers compared to the footwall side and hanging wall side vertical movement for all GPS stations along the Long-Point Fault. The Chicot and Evangeline ground water levels have been increasing in this area since 2000, but are still below the regional preconsolidation of ~30 meters below the ground surface, contributing to the subsidence observed. No considerable coherent fault motions were observed along the fault surface trace.

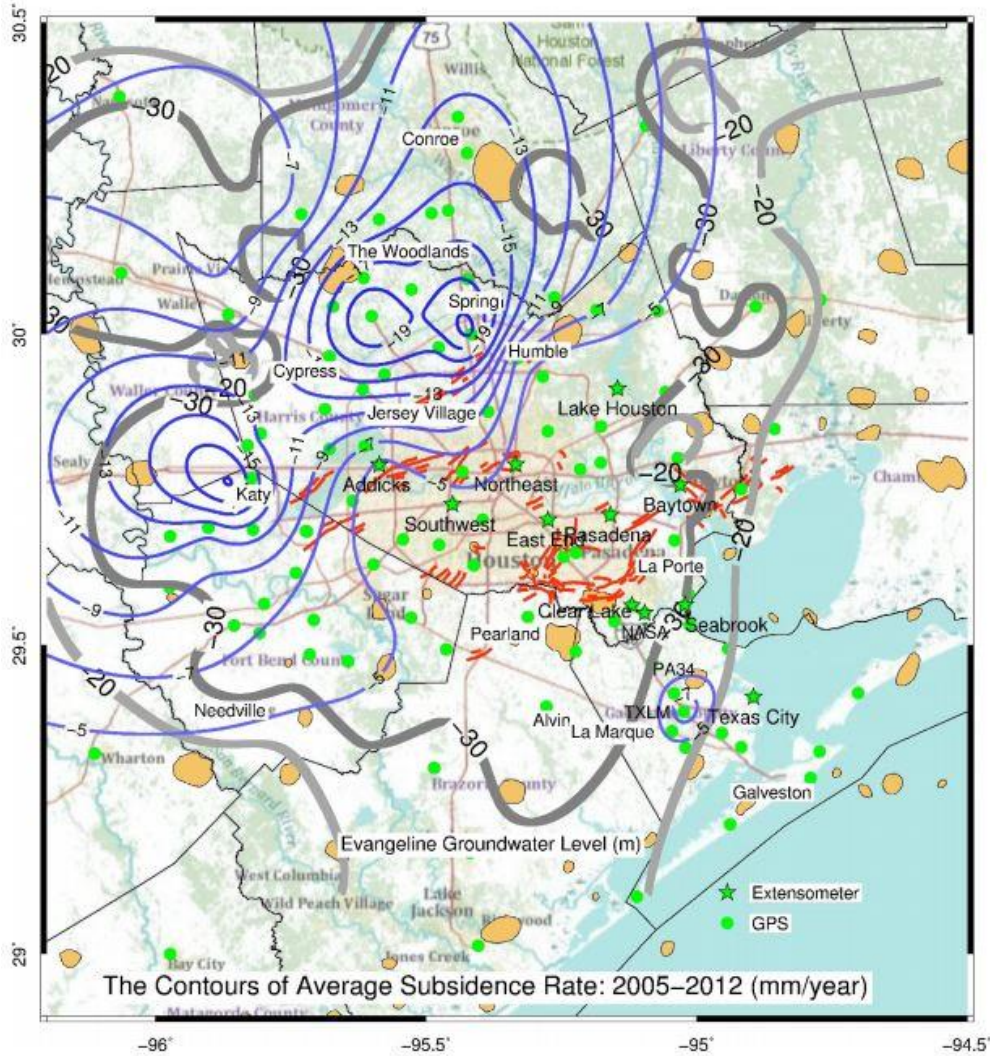

Figure 6.27: Average Subsidence Rates Within the Houston Area

Subsidence rates established from 2005–2012 within the Greater Houston Area (Kearns et al., 2015).

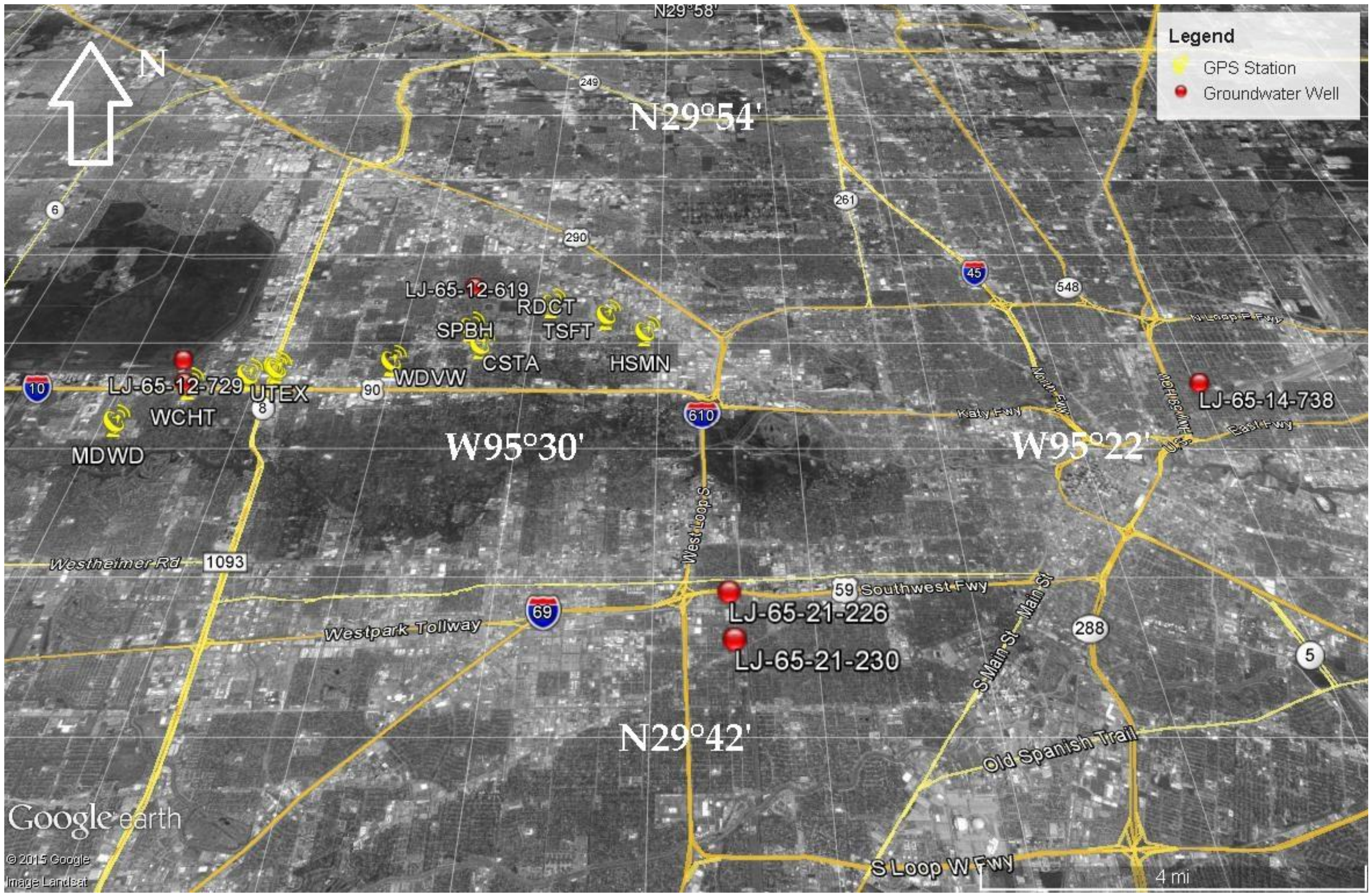

Figure 6.28: Water Wells Within Western Houston Area

Groundwater well positions relative to the eleven GPS Stations within the Western Houston area.

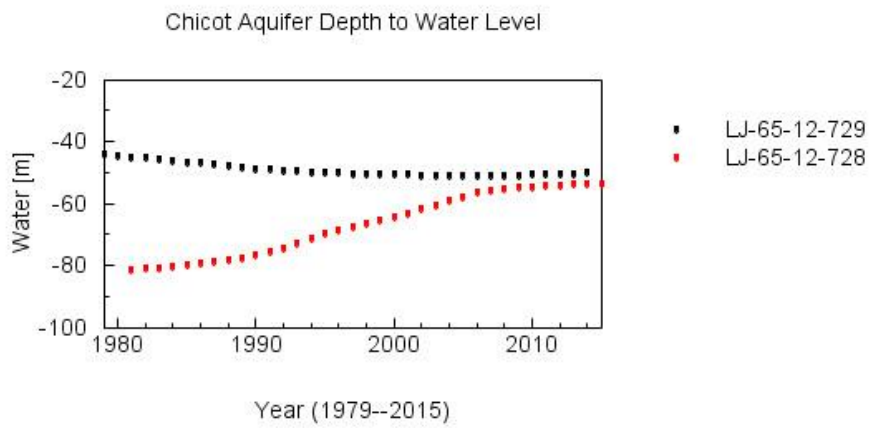

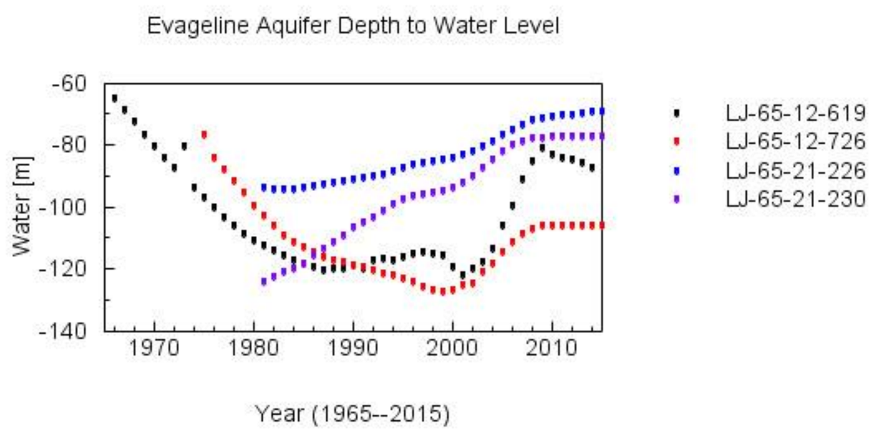

Figure 6.29: Yearly Depth to Water Level for Chicot and Evangeline Aquifer

Time series comparison of aquifers Chicot and Evangeline within the area of the Long-Point Fault. Two water wells (LJ-65-12-729 and LJ-65-12-728) represent the Chicot aquifer, while four water wells (LJ-65-12-619, LJ-65-12-726, LJ-65-21-226, and LJ-65-21-230) represent the Evangeline aquifer.

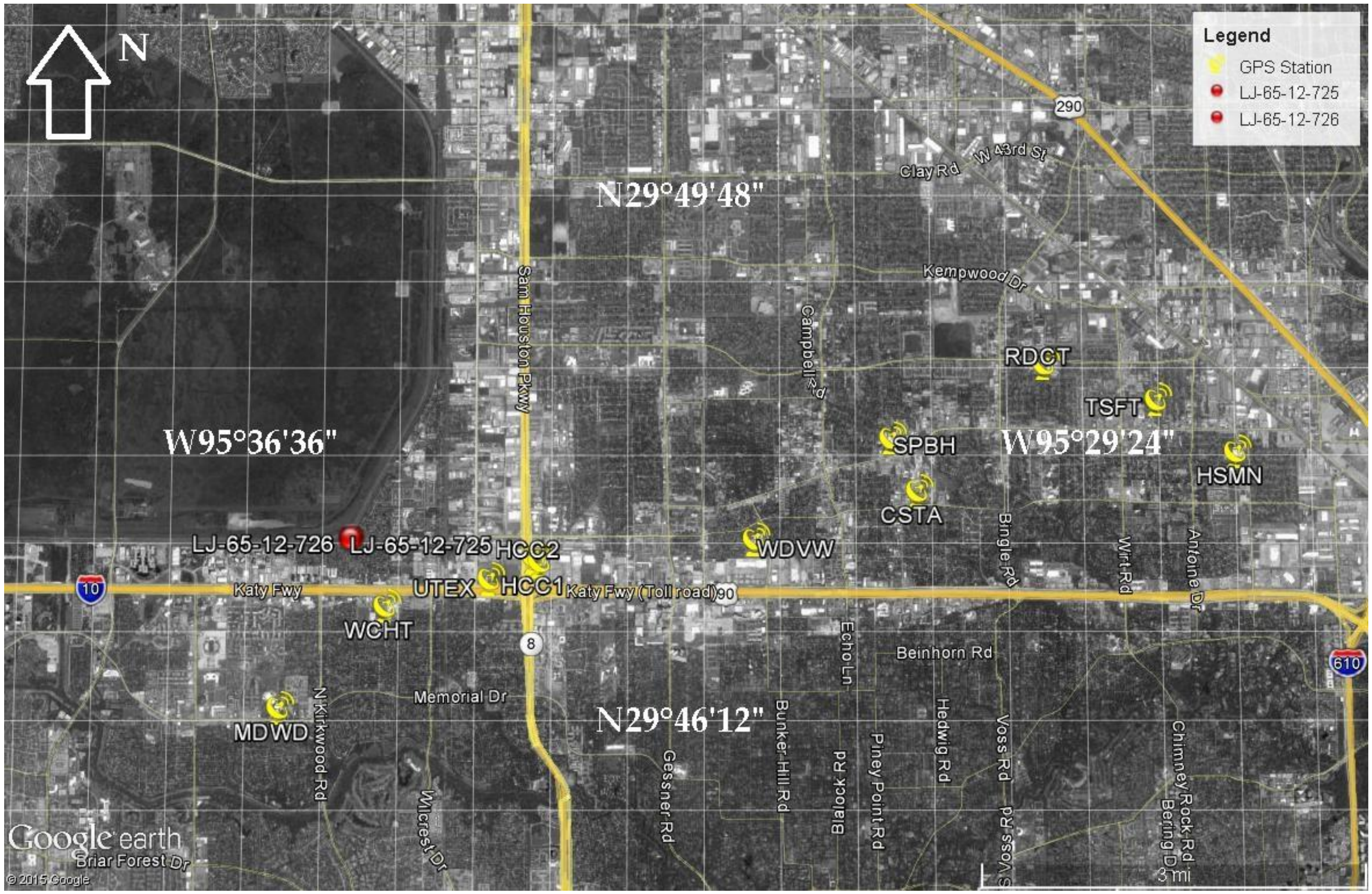

Figure 6.30: Water Wells Within Vicinity of Study Area

Water well positions relative to the eleven GPS Stations within the Long-Point Fault area.

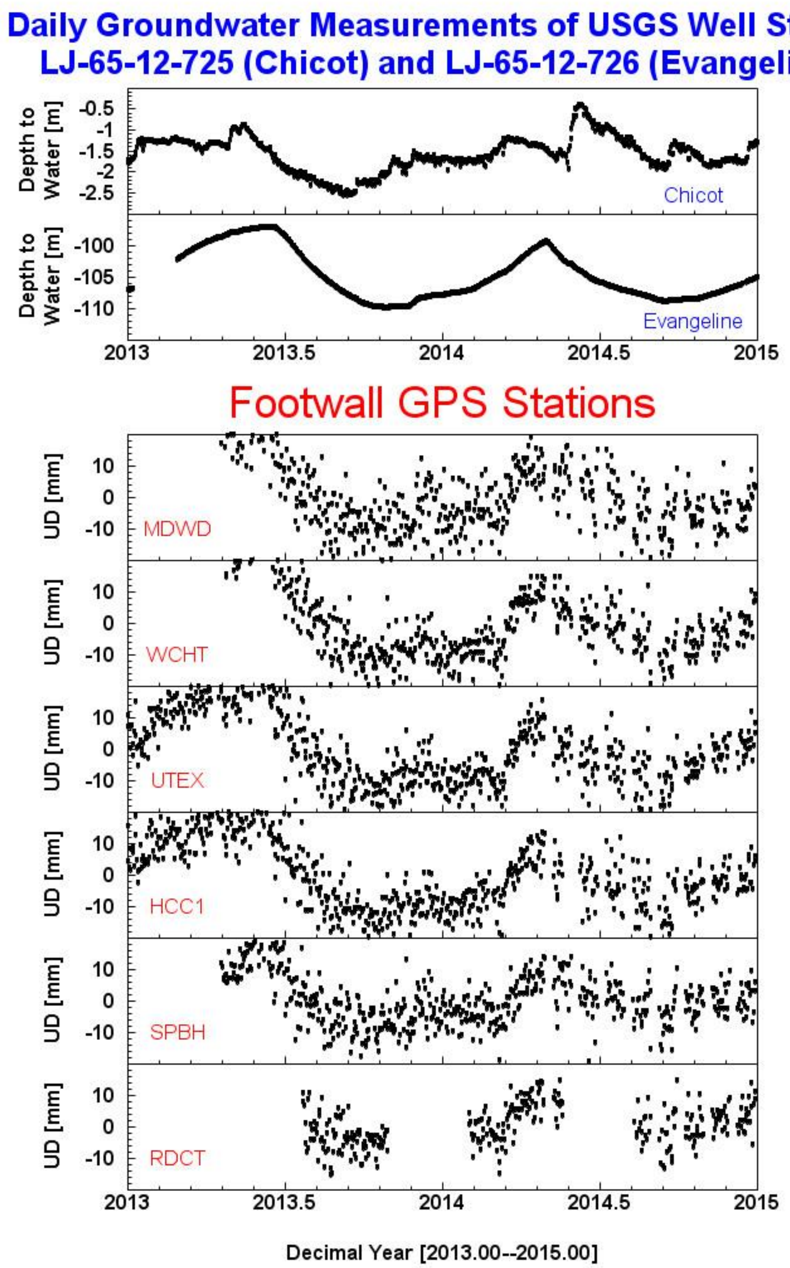

Figure 6.31: Daily Depth to Water Level for the Chicot and Evangeline Aquifer Compared to Footwall Side GPS Station Vertical Movement

Time series comparison of aquifers Chicot and Evangeline within the area of the Long-Point Fault compared to footwall side GPS station vertical movement. Two water wells (LJ-65-12-725 and LJ-65-12-726) represent the Chicot aquifer and Evangeline aquifer, respectively. (Rebound = positive UD and subsidence = negative UD.)

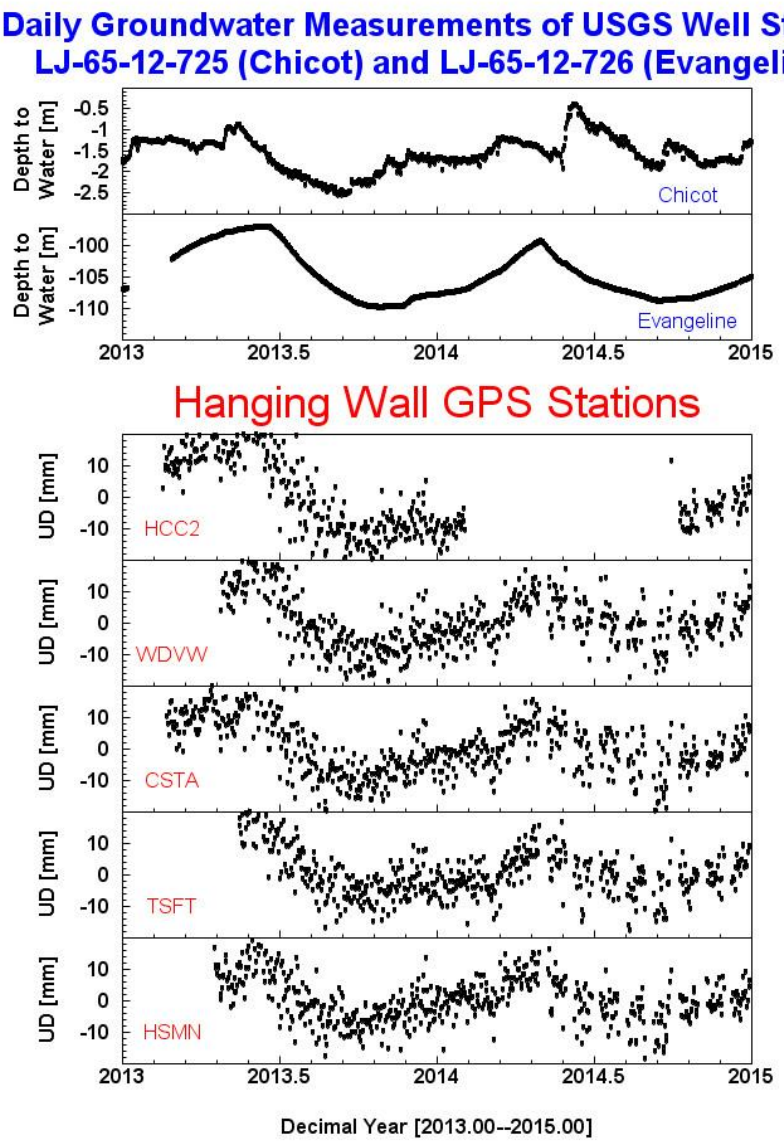

Figure 6.32: Daily Depth to Water Level for the Chicot and Evangeline Aquifer Compared to Hanging Wall Side GPS Station Vertical Movement

Time series comparison of aquifers Chicot and Evangeline within the area of the Long-Point Fault compared to hanging wall side GPS station vertical movement. Two water wells (LJ-65-12-725 and LJ-65-12-726) represent the Chicot aquifer and Evangeline aquifer, respectively. (Rebound = positive UD and subsidence = negative UD.)

7 Discussion and Conclusions

This study was aimed at investigating current ground motions associated with the Long-Point Fault. Employing a high-resolution LiDAR map depicting precise locations of principal fault systems within the greater Houston metropolitan area, georeferencing collaborated with a high-accuracy kinematic GPS technique established the precise fault trace of the Long-Point Fault. Field investigations verified that the fault scarp mapped by the 2001 airborne LiDAR mapping of the Houston region is in fact the surface trace of the Long-Point Fault. Eleven permanent GPS stations along the Long-Point fault were installed for continuous GPS monitoring in 2012. Twenty-six benchmarks were installed along the Long-Point fault trace and were used to capture monthly surveys. Two months of campaign survey measurements are not long enough to identify any coherent fault motions. Observations between the first and second survey measurements reveal certain differences on the order of subcentimeters, whereas all directional movements with respect to the Long-Point Fault are on the order of millimeters. Specific to this study, benchmark observations of fifteen to twenty minutes cannot achieve the accuracy provided by twenty-four hour, continuous monitoring that permanent GPS stations provide. Daily GPS observations from 2012–2014 were processed using both relative (double differencing) and absolute (precise point positioning) positioning methods. Two years of GPS observations indicate that the Long-Point Fault area is experiencing subsidence. All GPS stations along the Long-Point Fault observed subsidence rates ranging from 1–7 mm/year as well as strong vertical seasonal variation, 4 cm peak to peak. Minor horizontal movements ranging from 1–4 mm/yr, referred to the stable Houston reference frame (SHRF), were observed at several GPS stations; however, no considerable coherent fault motions were observed along the fault surface trace. Groundwater data from water wells near the Long-Point Fault area were obtained and examined for possible correlation with subsidence. By examining yearly and daily depth to groundwater level data, the Chicot and Evangeline aquifer system was observed to display stability within the past five years. At the end of 2014, the groundwater levels in the Chicot and Evangeline aquifers in the Long-Point Fault area were 50–53 m and 69–106 m below the ground surface, respectively. Daily depth to groundwater level for the Chicot and Evangeline aquifer system show correlation between aquifer recharge, and withdrawal, and vertical seasonal variation exhibited by all installed GPS stations along the Long-Point Fault. The Chicot and Evangeline ground water levels have been increasing in this area since 2000, but are still below the regional preconsolidation of ~30 m below the ground surface, contributing to the subsidence observed. While correlation between seasonal vertical variation and groundwater level change exists, a longer period of continuous GPS observations will be able to provide more information about the activity of the fault.

The continual investigation of surface ground motion along the Long-Point Fault for greater than five years is proposed. LiDAR scans of damaged zones and additional field mapping (or investigations) are planned to determine the width of the Long-Point

Fault damage zone (if any) and whether there are branches in the Long-Point Fault attributing to ground motion.

8 Appendix

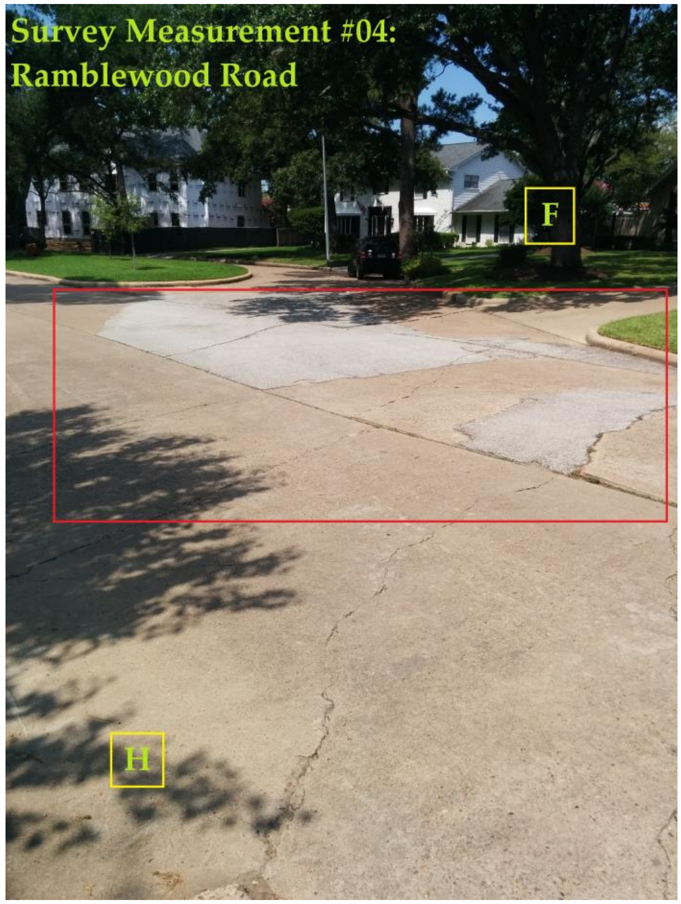

Figure A.01: GPS Survey Measurement #04 (Ramblewood Rd)

GPS survey measurement #04 (Latitude: 29°46′15.76 N, Longitude: 95°35′19.88″ W) on Ramblewood Road displays road damage (red rectangle). Footwall side (F) and hanging wall side (H) of the Long-Point Fault are labeled for reference.

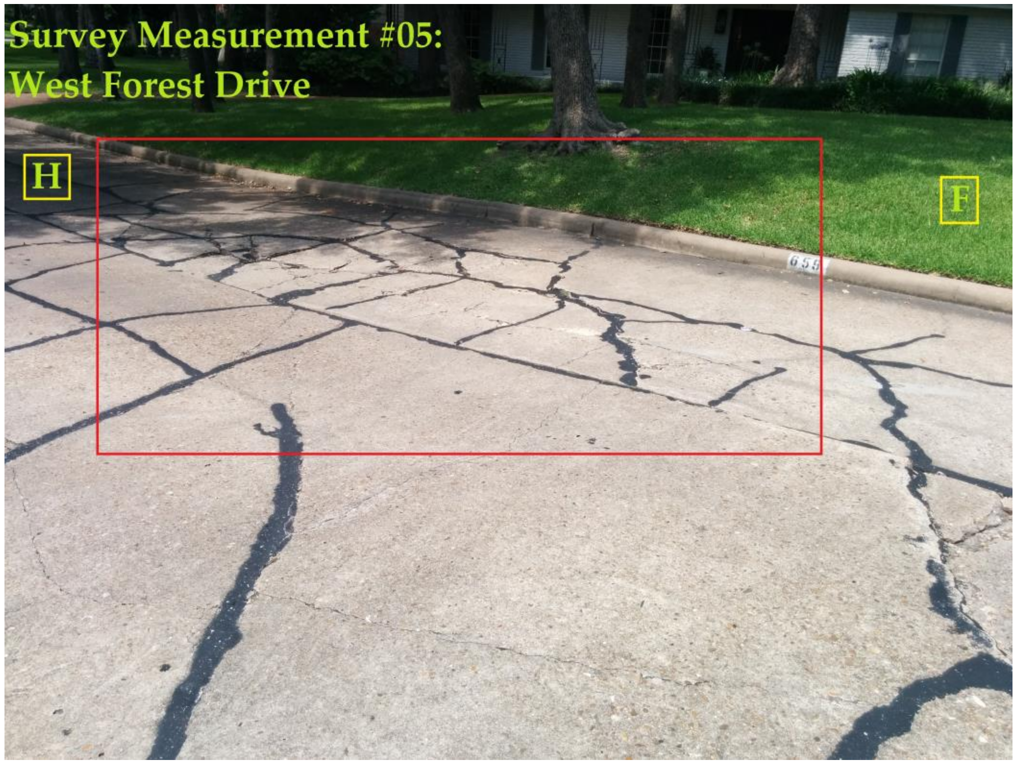

Figure A.02: GPS Survey Measurement #05 (West Forest Dr)

GPS survey measurement #05 (Latitude: 29°46’20.78 N, Longitude: 95°35’8.94” W) on West Forest Drive displays road damage (red rectangle). Footwall side (F) and hanging wall side (H) of the Long-Point Fault are labeled for reference.

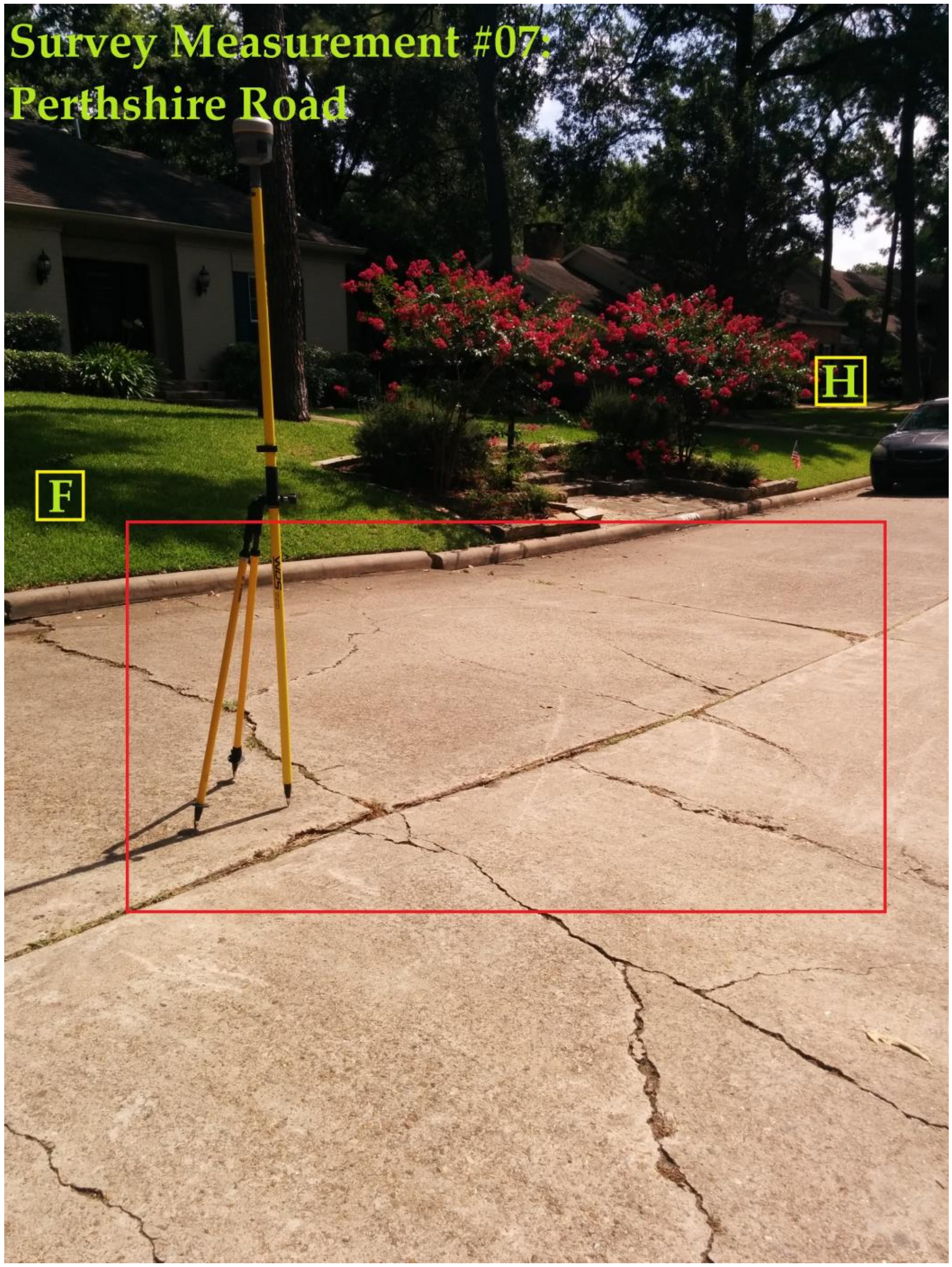

Figure A.03: GPS Survey Measurement #07 (Perthshire Rd)

GPS survey measurement #07 (Latitude: 29°46′31.31 N, Longitude: 95°35′0.71″ W) on Perthshire Road displays road damage (red rectangle). Footwall side (F) and hanging wall side (H) of the Long-Point Fault are labeled for reference.

Figure A.04: GPS Survey Measurement #09 (Glenchester Dr)

GPS survey measurement #09 (Latitude: 29°46’37.86 N, Longitude: 95°34’46.71” W) on Glenchester Drive displays road damage (red rectangle). Footwall side (F) and hanging wall side (H) of the Long-Point Fault are labeled for reference.

Figure A.05: GPS Survey Measurement #14 (Lasso Ln)

GPS survey measurement #14 (Latitude: 29°46′58.91 N, Longitude: 95°34′12.20″ W) on Lasso Lane displays road damage (red rectangle). Footwall side (F) and hanging wall side (H) of the Long-Point Fault are labeled for reference.

Figure A.06: GPS Survey Measurement #26 (Bullock Ln)

GPS survey measurement #26 (Latitude: 29°47’32.32 N, Longitude: 95°32’11.23” W) on Bullock Lane displays road damage (red rectangle). Footwall side (F) and hanging wall side (H) of the Long-Point Fault are labeled for reference.

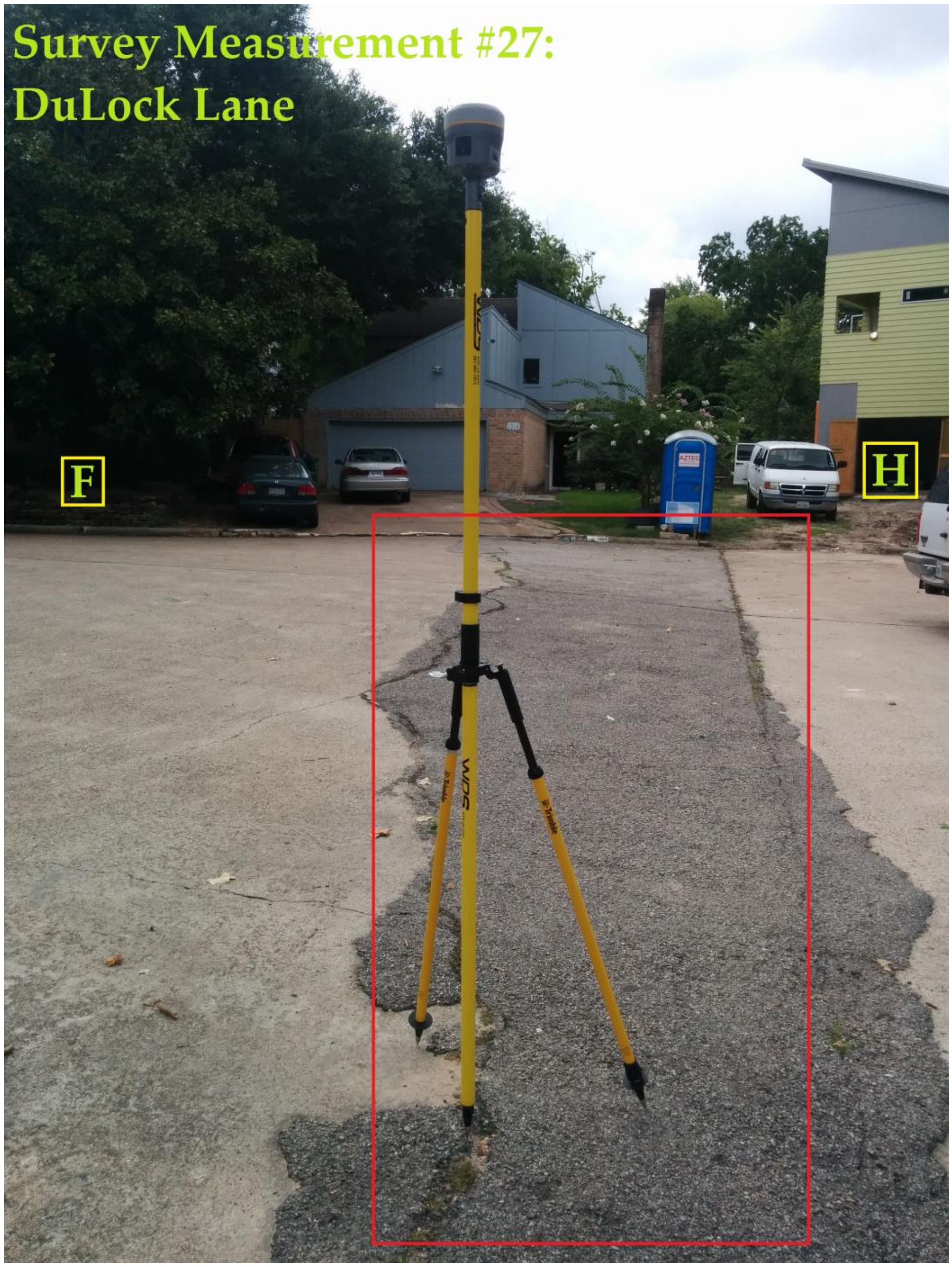

Figure A.07: GPS Survey Measurement #27 (Du Lock Ln)

GPS survey measurement #27 (Latitude: 29°47′31.84 N, Longitude: 95°32′7.85″ W) on Du Lock Lane displays road damage (red rectangle). Footwall side (F) and hanging wall side (H) of the Long-Point Fault are labeled for reference.

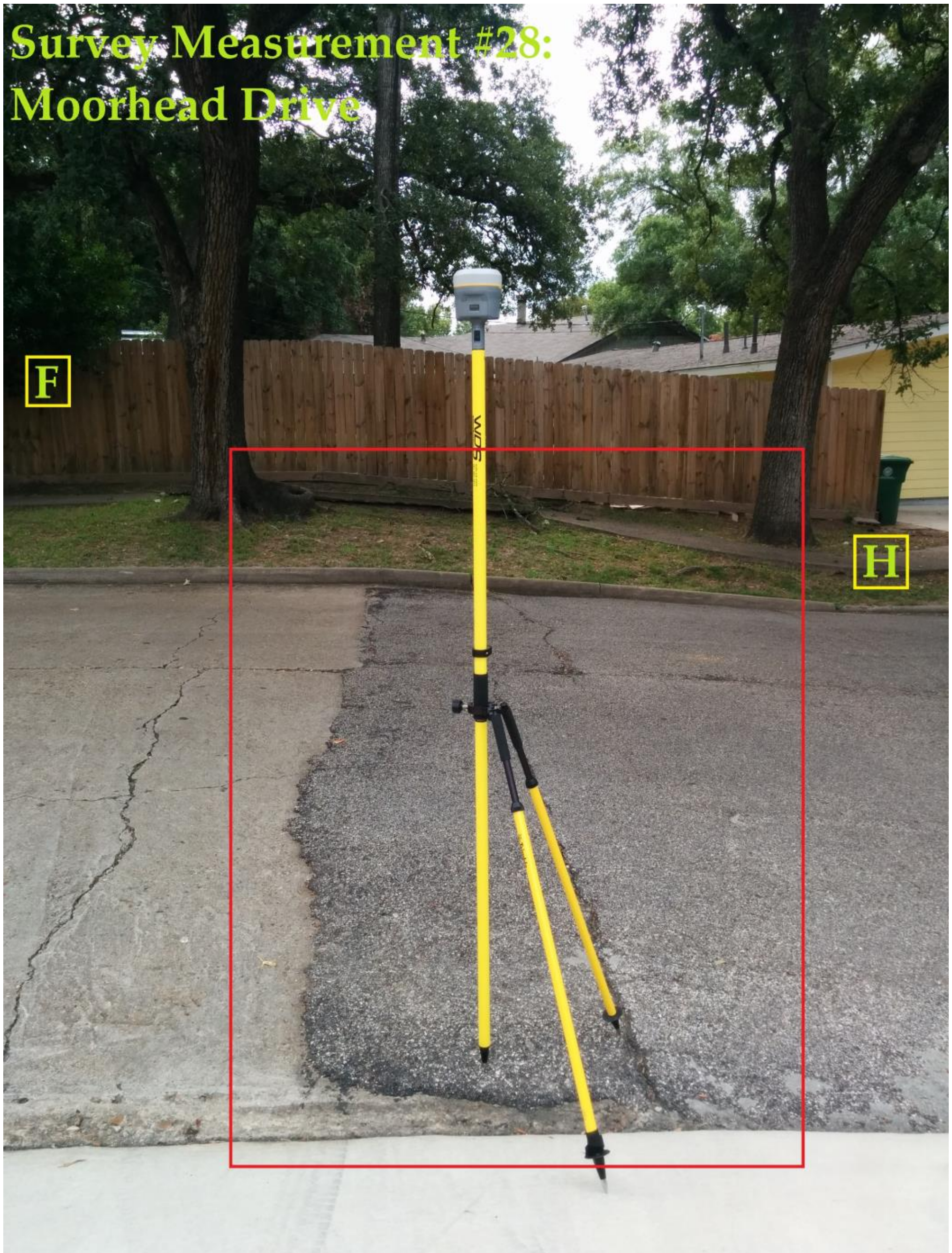

Figure A.08: GPS Survey Measurement #28 (Moorehead Dr)

GPS survey measurement #28 (Latitude: 29°47’31.64 N, Longitude: 95°32’4.29” W) on Moorehead Drive displays road damage (red rectangle). Footwall side (F) and hanging wall side (H) of the Long-Point Fault are labeled for reference.

Figure A.09: GPS Survey Measurement #32 (Panola Way)

GPS survey measurement #32 (Latitude: 29°47′37.81 N, Longitude: 95°31′35.52″ W) on Panola Way displays road damage (red rectangle). Footwall side (F) and hanging wall side (H) of the Long-Point Fault are labeled for reference.

Figure A.10: GPS Survey Measurement #33 (Oak Tree Rd)

GPS survey measurement #33 (Latitude: 29°47′39.05 N, Longitude: 95°31′32.60″ W) on Oak Tree Road displays ground damage (red rectangle). Footwall side (F) and hanging wall side (H) of the Long-Point Fault are labeled for reference.

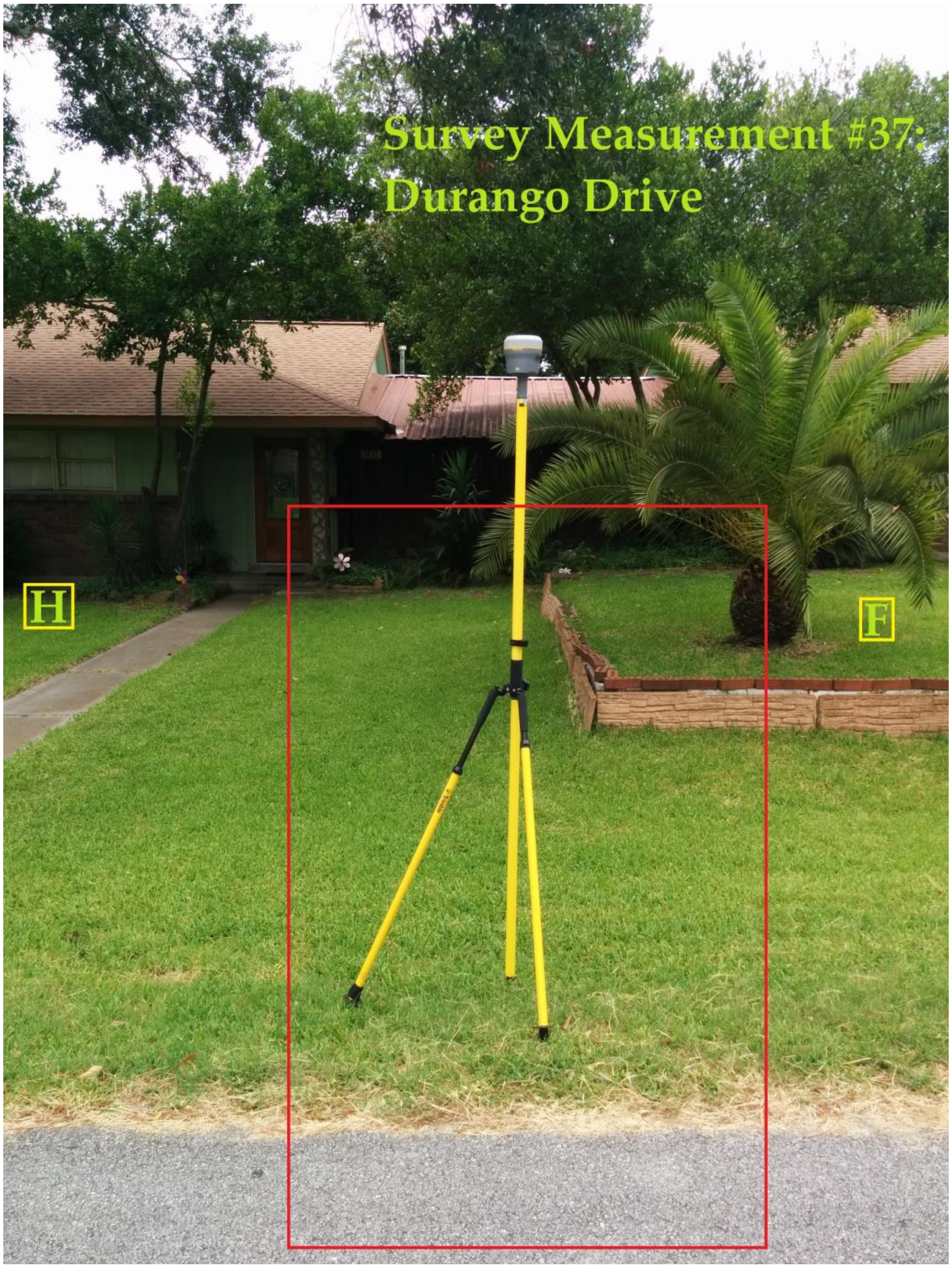

Figure A.11: GPS Survey Measurement #37 (Durango Dr)

GPS survey measurement #37 (Latitude: 29°47′45.61 N, Longitude: 95°31′9.16″ W) on Durango Drive displays ground damage (red rectangle). Footwall side (F) and hanging wall side (H) of the Long-Point Fault are labeled for reference.

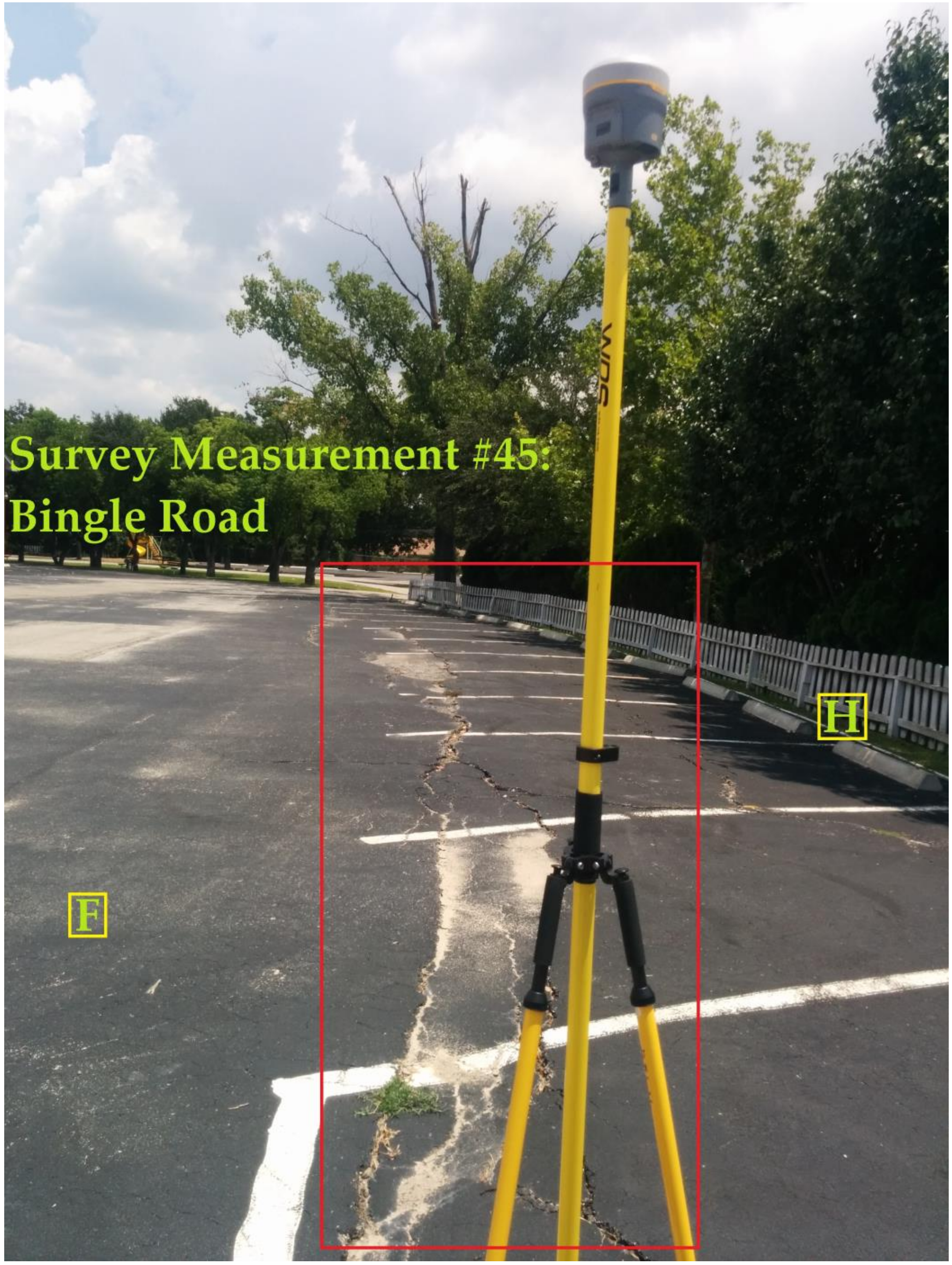

Figure A.12: GPS Survey Measurement #45 (Bingle Rd)

GPS survey measurement #45 (Latitude: 29°48′1.05 N, Longitude: 95°30′2.69″ W) on Bingle Road displays parking lot damage (red rectangle). Footwall side (F) and hanging wall side (H) of the Long-Point Fault are labeled for reference.

Figure A.13: Bracket for Mounting to Building
8x12x36 inch welded bracket, with eight pre-drilled holes for mounting.

Figure A.14: Ideal Bracket Mounting Position

Mounting of bracket to corner of building with clearance to the roofline.

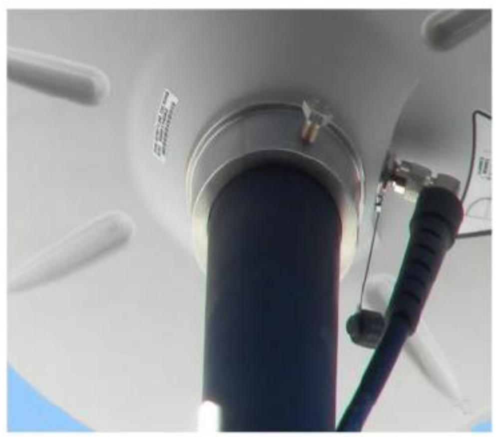

Figure A.15: Adapter between Antenna and Bracket

Stainless steel adapter allowing antenna to remain stationary in 3D space. If repair is needed, the adapter allows for a simple exchange of the antenna.

Figure A.16: Leveling and Marking of Pilot Hole

Colleagues on the roof assist by holding the bracket in place, while the installer positioned on the ladder simultaneously levels the bracket and marks a pilot hole for drilling.

Figure A.17: Drilling Pilot Hole

Colleagues brace the bracket in place while the installer prepares to drill a pilot hole.

Figure A.18: Mounted Bracket

Mounted bracket secured with eight masonry anchors.

Figure A.19: Mounted Junction Box over Penetration Hole

Exterior junction box (uncovered) mounted over penetration hole in close proximity to bracket.

Figure A.20: Mounted Junction Box with Coaxial Cable Enclosed in Conduit

Exterior junction box (covered) with coaxial cable enclosed in conduit, secured by hose fittings to prevent water damage to cable and building.

Figure A.21: Mounted Junction Box with Receiver and Electrical Cords
Electrical cable junction box housing receiver with attached coaxial cable, Ethernet cable, and power adapter.

Figure A.22: Permanent GPS Stations Part 1

Clockwise from top left: MDWD, WCHT, UTEX, and HCC2.

Figure A.23: Permanent GPS Stations Part 2
Clockwise from top left: HCC1, WDVW, SPBH, and CSTA.

Figure A.24: Permanent GPS Stations Part 3
Clockwise from top left: RDCT, TSFT, and HSMN.

Figure A.25: Installed Benchmark (JS04)

Benchmark JS04 (Latitude: 29°46′31.20 N, Longitude: 95°35′0.44″ W) pictured is positioned on the hanging wall side of the Long-Point Fault. The benchmark is shown being surveyed.

Figure A.26: Installed Benchmark (JS11)

Benchmark JS11 (Latitude: 29°47'36.58 N, Longitude: 95°32'24.74" W) pictured is positioned on the footwall side of the Long-Point Fault. The benchmark is shown being surveyed.

Figure A.27: Installed Benchmark (JS14)

Benchmark JS14 (Latitude: 29°47’31.09 N, Longitude: 95°32’1.56” W) pictured is positioned on the hanging wall side of the Long-Point Fault. The benchmark is shown being surveyed.

Figure A.28: Installed Benchmark (JS16)

Benchmark JS16 (Latitude: 29°47′37.43 N, Longitude: 95°31′32.89″ W) pictured is positioned on the hanging wall side of the Long-Point Fault. The benchmark is shown being surveyed.

Figure A.29: Installed Benchmark (JS17)

Benchmark JS17 (Latitude: 29°47′47.49 N, Longitude: 95°31′9.13″ W) pictured is positioned on the footwall side of the Long-Point Fault. The benchmark is identified in the study area by the fluorescent green circle.

Figure A.30: Installed Benchmark (JS26)

Benchmark JS26 (Latitude: 29°48′12.09 N, Longitude: 95°29′28.23″ W) pictured is positioned on the hanging wall side of the Long-Point Fault. The benchmark is shown being surveyed.

9 Works Cited

Abidin, H. Z., Andreas, H., Djaja, R., Darmawan, D., and Gamal, M. (2008), Land subsidence Characteristics of Jakarta between 1997 and 2005, as estimated using GPS surveys, GPS Solutions, 12, 23–32.

Ashworth, J. B., and Hopkins, J. (1995), Aquifers of Texas. Austin, TX, Texas Water Development Board Report 345.

Baker Jr, E. (1978), Stratigraphic and Hydrogeologic Framework of Part of the Coastal Plain of Texas, USGS Open-File Report, 77–712.

Bar-Sever, Y. E., Kroger, P. M., and Borjesson, J. A. (1998), Estimating horizontal gradients of tropospheric path delay with a single GPS receiver, Journal of Geophysical Research, 103(B3), 5019–5035.

Bawden, G. W., Johnson, M. R., Kasmarek, M. C., Brandt, J., & Middleton, C. S. (2012), Investigation of Land Subsidence in the Houston–Galveston Region of Texas by Using the Global Positioning System and Interferometric Synthetic Aperture Radar, 1993–2000, Denver, CO, U.S. Geological Survey Scientific Investigations Report 2012–5211.

Berman, Arthur E. (2005), The Debate over subsidence in coastal Louisiana and Texas, Houston Geological Society Bulletin 48(1), 47-54.

Bertiger, W., Desai, S. D., Haines, B., Harvey, N., Moore, A. W., Owen, S., & Weiss, J. P. (2010), Single receiver phase ambiguity resolution with GPS data, Journal of Geodesy, 84(5), 327–337.

Bird, Dale E., Kevin Burke, Stuart A. Hall, and John F. Casey (2005), Gulf of Mexico tectonic history: Hotspot tracks, crustal boundaries, and early salt distribution, AAPG Bulletin 89(3), 311–328.

Blewitt, G. (1989), Carrier phase ambiguity resolution for the global positioning system applied to geodetic baselines up to 2000 km, Journal of Geophysical Research, 94(B8), 10,187–10,203.

Boehm, J., and Schuh, H. (2004), Vienna mapping functions in VLBI analyses, Geophysical Research Letters, 31(L01603), doi:10.1029/2003GL018984.

Bruce, Clemont H. (1973), Pressured shale and related sediment deformation: Mechanism for development of regional contemporaneous faults, AAPG Bulletin, 57, 878–886.

Buckley, S. M., Rosen, P., Hensley, S., and Taplay, B. D. (2003), Land subsidence in Houston, Texas, measured by radar interferometry and constrained by extensometers, Geophysics Research, 108(B11), 2542–2553.

Chowdhury, A. H., and Turco, M. J. (2006), Geology of the Gulf Coast aquifer, Texas, Texas Water Development Board Report 365. Retrieved 03, 2015. https://www.twdb.texas.gov/publications/reports/numbered_reports/doc/R365/ch02-Geology.pdf

Coleman, J. M., Roberts, H. H., and Bryant, W. R., (1991), Late Quaternary sedimentation, in Salvador, A., ed., The Gulf of Mexico Basin: The Geology of North America, Boulder, CO, Geological Society of America, volume J, 325–352.

Davis, J. L., Herring, T. A., Shapiro, I., Rogers, A., and Elgered, G. (1985), Geodesy by radio interferometry: Effects of atmospheric modeling errors on estimates of baseline length, Radio Science, 20(6), 1593–1607.

Department of Homeland Security. (2013), GPS Status Advisory. U.S. Coast Guard. Alexandria, VA: Navigation Center (NAVCEN).

Dokka, Roy K. (2004), The Anatomy of a silent disaster: Ongoing subsidence and inundation of the Northern Margin of the Gulf of Mexico Basin, Houston Geological Society Bulletin, 47(3), 19–21.

El-Rabbany, A. (2006), Introduction to GPS: The Global Positioning System 2nd Edition. Norwood: Artech House.

Engelkemeir, R., Khan, S. D., & Burke, K. (2010), Surface deformation in Houston, Texas using GPS, Tectonophysics, 490(1–2), 47–54.

Everett, John R., and William M. Reid. (1979), Active faults in Houston, Texas, area as observed on LANDSAT imagery, AAPG Bulletin, 63, 13–27.

Firuzabadi´, D., & King, R. W. (2012), GPS precision as a function of session duration and reference frame using multi-point software, GPS Solutions, 16, 191–196.

Galloway, W. E., Bebout, D. G., Fisher, W. L, Dunlap, J. B., Cabrera-Castro, R., Lugo-Riveraa, J. E., and Scott, T. M., (1991), Cenozoic, in Salvador, A., ed., The Gulf of Mexico Basin: The Geology of North America, Boulder, CO, Geological Society of America, volume J, 245–324.

Galloway, D. L. & Burbey, T. J., (2011), Review: Regional land subsidence accompanying groundwater extraction, Hydrogeology Journal, 19, 1459–1486.

Gao, Y., and Chen, K. (2004), Performance analysis of precise point positioning using real-time orbit and clock products, Journal of Global Positioning System, 3(1–2), 95–100.

Gurtner, Werner. (2007), RINEX: The Receiver Independent Exchange Format Version 2.10, NASA JPL. ftp://igscb.jpl.nasa.gov/pub/data/format/rinex210.txt

Hodgson, M. E., Jensen, J., Raber, G., Tullis, J., Davis, B. A., Thompson, G. and Schuckman, K., (2005), An evaluation of LiDAR-derived elevation and terrain slope in leaf-off condition, Photogrammetric Engineering and Remote Sensing, 71(7), 817–823.

IGS Central Bureau (2013), International GNSS Service formally the International GPS Service. Retrieved 01, 2015.

Jackson, M. P. A., and Steven J. Seni (1984), Domes of East Texas, AAPG Bulletin, 68, 163–179.

Jackson, M. P. A., and C. J. Talbot, 1986, External shapes, strain rates, and dynamics of salt structures: Geological Society of America Bulletin, v. 97, p. 305–323.

Kaplan, E. (1996), Introduction, Understanding GPS Principles and Applications, Artech House Inc., Norwood, MA, 1–15.

Kasmarek, M. C., & Strom, E. W. (2002), Hydrogeology and Simulation of Ground-Water Flow and Land-Surface Subsidence in the Chicot and Evangeline Aquifers, Houston Area, Texas, Austin, TX, U.S. Geological Survey Water-Resources Investigations Report 02–4022.

Kasmarek, M., Johnson, M., & and Ramage, J. (2010), Water-level Altitudes 2010 and Water Level Changes in the Chicot, Evangeline, and Jasper Aquifers and Compaction 1973–2009 in the Chicot and Evangeline Aquifers, Houston–Galveston Region, Texas, Denver, CO, U.S. Geological Survey Scientific Investigations Map 3138.

Kearns, T.J. (2015), Current Land Subsidence and Groundwater level changes in the Houston Metropolitan Area, Texas (2005–2012), Journal of Surveying Engineering, in press 2015.

Kedar, S., Hajj, G. A., Wilson, B. D., and Heflin, M. B. (2003), The effect of the second order GPS ionospheric correction on receiver positions, Geophysical Research Letters, 30(16), 1829.

Knox, P. R., Young, S. C., Galloway, W. E., Jr., E. T., and Budge, T. (2006), A Stratigraphic approach to Chicot and Evangeline aquifer boundaries, central Texas Gulf Coast, Gulf Coast Association of Geological Societies Transactions, 56, 371–393.

Kouba, J. (2002), The GPS Toolbox - ITRF Transformations, GPS Solutions, 5(3), 88–90.

Leake, S.A., and Prudic, D.E. (1991), Documentation of a Computer Program to Simulate Aquifer System Compaction using the Modular Finite-Difference Ground-Water Flow Model. Denver, CO: U.S. Geological Survey, Techniques of Water-Resources Investigations, Book 6, Chapter A2.

Leick, A. (1996), Processing Pseudoranges and Carrier Phases, GPS Satellite Surveying, John Wiley & Sons, Hoboken, NJ, 228–300.

Lohse, E.A. (1955), Dynamic geology of the modern coastal region, northwest Gulf of Mexico, in finding ancient shorelines: Soc. Econ. Paleontologists and Mineralogists Spec. Pub. No. 3, 99–105.

Los Angeles Air Force Base (2012), Fact Sheet. Global Positioning Systems Directorate. Retrieved 02, 2015. http://www.losangeles.af.mil/library/factsheets/factsheet.asp?id=5311

Lyard, F., Lefevre, F., Letellier, T., & Francis, O. (2006), Modelling the global ocean tides: modern insights from FES2004, Ocean Dynamics, 56, 394–415.

Mc Farlan, E., and Menes, L. S. (1991), Lower Cretaceous, in Salvador, A., ed., The Gulf of Mexico Basin: The Geology of North America, Boulder, CO, Geological Society of America, volume J, 181–204.

Meigs, A. (2013), Active tectonics and the LiDAR revolution, Lithosphere, 5, 226–229.

Meyer, Willis G. (1939), Stratigraphy and historical geology of Gulf coastal plain in vicinity of Harris County, Texas, AAPG Bulletin, 23, 145–211.

NCO (2013), Official U.S. Government information about the Global Positioning System (GPS) and related topics. (National Coordination Office - Space Based Positioning, Editor) Retrieved 02, 2015. http://www.gps.gov

Neighbors, R. J., and Mitchell, G. J. (2010), A plan to use continuously operating GPS stations to monitor subsidence in the Harris–Galveston coastal subsidence district. Retrieved 03, 2015. http://www.ngs.noaa.gov/PUBS_LIB/A_PlanToUseContinuouslyOperatingGPS_%20StationsToMonitorSubsidenceInTheHarris-GalvestonCoastalSubsidenceDistrict.pdf

Nelson, T. H. (1991), Salt tectonics and listric-normal faulting, in Salvador, A., ed., The Gulf of Mexico Basin: The Geology of North America, Boulder, CO, Geological Society of America, volume J, 73–90.

NGS-CORS, N. G. (2013), Guidelines for New and Existing Continuously Operating Reference Stations (CORS), Springfield, MD: National Ocean Survey, NOAA.

Pearson, C., McCaffrey, R., Elliott, J. L., & Snay, R. (2010), HTDP 3.0: Software for coping with the coordinate changes associated with crustal motion, Journal of Surveying Engineering, 136(2), 80–90.

Pratt, W. E., & Johnson, D. W. (1926), Local subsidence of the Goose Creek oil field, Journal of Geology, 34(7, Part 1), 577–590.

Ray, J., Rebischung, P., and Schmid, R. (2011), Dependence of IGS products on the ITRF Datum, International Association of Geodesy Symposia, 138, 63–67.

Reid, William M. (1973), Active Faults in Houston, Texas, PhD Dissertation, University of Texas at Austin, 143 pp.

Remondi, B. W. (1985), Global positioning system carrier phase: Description and use, Bulletin of Geodesy, 59(4), 361–377.

Richmond, G.M., Weide, D.L., and Moore, D.W., eds., Pope, D.E., Gilliland, W.A., and Wermund, E.G., State compilations, 1990, Quaternary Geologic Map of the White Lake 4° x 6° Quadrangle, United States: U.S. Geological Survey Miscellaneous Investigations Series Map I–1420 (NH–15), scale 1:1,000,000 [Bush, C.A., Digital edition, 2012].

Salvador, A. (1991), Triassic-Jurassic, in Salvador, A., ed., The Gulf of Mexico Basin: The Geology of North America, Boulder, CO, Geological Society of America, volume J, 131–180.

Salvador, A. (1991b), Origin and development of the Gulf of Mexico basin, in Salvador, A., ed., Boulder, CO, Geological Society of America, volume J, 389–444.

Schmid, K.; Hadley, B.C., and Wijekoon, N. (2011), Vertical accuracy and use of topographic LIDAR data in coastal marshes, Journal of Coastal Research, 27(6A), 116–132.

Shah, S. D., & Lanning-Rush, J. (2005), Principal Faults in the Houston Metropolitan Area -Scientific Investigations Map 2874, Denver, CO: U.S. Geological Survey.

Soler, T., and Marshall, J. (2003), A note on frame transformations with applications to geodetic datums, GPS Solutions, 7(1), 23–32.

Soler, T., and Snay, R. A. (2004), Transforming positions and velocities between the International Terrestrial Reference Frame of 2000 and North American Datum of 1983, Journal of Surveying Engineering, 130(2), 49–55.

Stork, S., and Sneed, M. (2002), Houston–Galveston Bay Area, Texas, From Space - A New Tool for Mapping Land Subsidence. Houston, TX: U.S. Geological Survey Fact Sheet, 110–120.

TSARP, Tropical Storm Allison Recovery Project (2002), Off The Charts. FEMA; HGFCD.U.S. Geological Survey. (2012), Earthquake glossary. Retrieved 03, 2015. http://earthquake.usgs.gov/learn/glossary/?termID=54

U.S. Geological Survey (2012), Geologic Maps of the US States. Retrieved 03 19, 2013. http://mrdata.usgs.gov/geology/state/

Van Siclen, D. C. (1961), Surface geology in and near Houston, in Geology of Houston and vicinity, Texas: Houston, Geological Society, 18–20.

Wang, G., & Soler, T. (2012), OPUS for horizontal subcentimeter-accuracy landslide monitoring: Case study in the Puerto Rico and Virgin Island region, Journal of Surveying Engineering 138(3), 143–153.

Wang, G., & Soler, T. (2013), Using OPUS for measuring vertical displacements in Houston, TX, Journal of Surveying Engineering, 138(3), 143–153.

Wang, G. (2011), GPS Landslide monitoring: Single base vs. network solutions, a case study based on the Puerto Rico and Virgin Islands permanent GPS Network, Journal of Geodetic Sciences, 1(3), 191–203.

Wang, G. (2013), Millimeter-Accuracy GPS Landslide monitoring using precise point positioning with single receiver phase ambiguity resolution: A case study in Puerto Rico, Journal of Geodetic Science, 3(1), 22–31.

Wang, G., J. Yu, J. Ortega, G. Saenz, T. Burrough, and R. Neill (2013), A stable reference frame for ground deformation study in the Houston Metropolitan Area, Texas, Journal of Geodetic Science, 3(3), 188–202.

Ward, P. (1996), GPS Satellite Signal Characteristics, Understanding GPS Principles and Applications, Artech House Inc., Norwood, MA, 83–117.

Waters, J. A., P. W. McFarland, and J. W. Lea, (1955), Geologic framework of Gulf coastal plain of Texas, Journal of Sedimentary Research, 39(5), 1821–1850.

Wehr, A. and Lohr, U. (1999), Airborne laser scanning – an introduction and overview. ISPRS Journal of Photogrammetry and Remote Sensing 54, 68–82.

Weston, N.D., Soler, T., and Mader, G.L. (2007), Web-based solutions for GPS data - NOAA OPUS, GIM Int., 21(4), 23–25.

Zilkoski, D. B., Hall, L. W., Mitchell, G. J., Kammula, V., Singh, A., Chrismer, W. M., and Neighbors, R. J. (2001), The Harris–Galveston Coastal Subsidence District/ National Geodetic Survey Automated GPS Subsidence Monitoring Project. Galveston: U.S. Geological Survey Subsidence Interest Group Conference.

Zumberge, J. F., Heftin, M. B., Jefferson, D., Watkins, M. M., & Webb, F. H. (1997), Precise point positioning for the efficient and robust analysis of GPS data from large networks, Journal of Geophysical Research, 102(B3), 5005–5517.